View metadata, citation and similar papers at core.ac.uk

brought to you by CORE

provided by ASU Digital Repository

Modeling Layered Accretion and the Magnetorotational Instability in Protoplanetary Disks

by

Michael V. Lesniak III

A Dissertation Presented in Partial Fulfillment
of the Requirements for the Degree
Doctor of Philosophy

Approved November 2011 by the
Graduate Supervisory Committee:

Steven Desch, Chair
Evan Scannapieco
Francis Timmes
Sumner Starrfield
Andrei Belitsky

ARIZONA STATE UNIVERSITY

May 2012

ABSTRACT

Understanding the temperature structure of protoplanetary disks (PPDs) is paramount to modeling disk evolution and future planet formation. PPDs around T Tauri stars have two primary heating sources, protostellar irradiation, which depends on the flaring of the disk, and accretional heating as viscous coupling between annuli dissipate energy. I have written a "1.5-D" radiative transfer code to calculate disk temperatures assuming hydrostatic and radiative equilibrium. The model solves for the temperature at all locations simultaneously using Rybicki's method, converges rapidly at high optical depth, and retains full frequency dependence.

The likely cause of accretional heating in PPDs is the magnetorotational instability (MRI), which acts where gas ionization is sufficiently high for gas to couple to the magnetic field. This will occur in surface layers of the disk, leaving the interior portions of the disk inactive ("dead zone"). I calculate temperatures in PPDs undergoing such "layered accretion." Since the accretional heating is concentrated far from the midplane, temperatures in the disk's interior are lower than in PPDs modeled with vertically uniform accretion. The method is used to study for the first time disks evolving via the magnetorotational instability, which operates primarily in surface layers. I find that temperatures in layered accretion disks do not significantly differ from those of "passive disks," where no accretional heating exists. Emergent spectra are insensitive to active layer thickness, making it difficult to observationally identify disks undergoing layered vs. uniform accretion.

I also calculate the ionization chemistry in PPDs, using an ionization network including multiple charge states of dust grains. Combined with a criterion for the onset of the MRI, I calculate where the MRI can be initiated

and the extent of dead zones in PPDs. After accounting for feedback between temperature and active layer thickness, I find the surface density of the actively accreting layers falls rapidly with distance from the protostar, leading to a net outward flow of mass from $\sim$0.1 to 3 AU. The clearing out of the innermost zones is possibly consistent with the observed behavior of recently discovered "transition disks."

DEDICATION

To my parents, who taught me that no goal is unattainable and to follow my dreams.

ACKNOWLEDGEMENTS

Many individuals have had a hand in me running the gauntlet through graduate classes, research, and writing papers and my dissertation. I would first like to thank the chair of my committee and my adviser, Dr. Steven Desch, for his wise counsel, patience, and guiding hand through my years at Arizona State University. I also want to extend my appreciation to the other members of my committee for making themselves available to me when needed: Dr. Evan Scannapieco, Dr. Frank Timmes, Dr. Sumner Starrfield, and Dr. Andrei Belitsky.

The computer codes used to generate the models presented in this dissertation are written entirely in FORTRAN 90. It wasn't until taking Dr. Eric Kostelich's scientific computing course that I was aware of this updated version of FORTRAN, and that not all versions subject the scientist using it to cruel and unusual punishment as FORTRAN 77 and its predecessors sometimes do.

I could not have kept my sanity without the support of my family and friends. My parents, Joanne and Michael, and my sister, Kristen, have always been supportive of me during this trip through graduate school. In the first years at ASU I was aided by my fellow classmates who braved the storm of graduate physics/astronomy classes and teaching astronomy labs together: Dr. Katherine Kaleida, Hwiyun Kim, Angel Fuentes, Adam Mott, and James Caruthers. I'd like to finally thank the rest of my friends and comrades here at ASU, who shared in the good times and the bad during my years here. In no particular order, they are William Gray, Dr. Melissa Morris, Simon Porter, Natalie Hinkel, Todd Veach, Dr. Russell Ryan, Dr. Kazuyuki Tamura, Dr. Nic Ouellette, Dr. R. Erik DeSimone, Jake Russell, and Jon Rohrbach.

TABLE OF CONTENTS

LIST OF TABLES

LIST OF FIGURES

Figure Page

Chapter 1

INTRODUCTION

1.1 Protoplanetary Disks

The question of how our solar system formed has been considered by philosophers and scientists at least as early as Descartes (1644). In addition to supporting Copernicus' then-controversial heliocentric model of the solar system, Descartes proposed that the motions in the universe could be explained by the non-existence of vacuums and structures that he called "swirling vortexes." While fundamentally incorrect, it provided a starting point for future theories on solar system formation. Changes and refinements were made over the decades after Descartes' work; however, it was in the 18th century when the first advances toward our modern theory of star/planet formation were made.

Swedenborg (1734) laid out a formation theory where a shell of particles around the Sun collapses into a belt and expands outward. The belt then fragments into pieces; the larger ones collapse to form planets and the smaller pieces fall back into the Sun. This idea was improved upon by Kant (1755), who postulated that a large cloud of gas and dust was the progenitor of the star/planet system. According to Kant, this cloud of gas and dust collapses into a disk out of which forms the central star and orbiting planets. Finally, Laplace (1796) added the idea of the circumstellar disk forming from a cooling and collapsing cloud. During this collapsing process rings of the disk break away and coalesce to form the planets. This model of the solar system's origins was recognized for its consistency with observations of the planets' motions. All planets orbit the Sun in a similar counter-clockwise fashion. This uniform orbital direction is due to the planets all forming from

a common disk which also rotated in a counter-clockwise direction.

Interestingly, while this theory (the "nebular hypothesis") was the prevailing theory for the centuries after its first proposal, observational evidence for such a scenario was lacking until recent decades (a more complete discussion can be found in the review of Boss 1989). Infrared observations of YSOs in the 12-25 μm wavelength range exhibited excess emission that was inconsistent with an isolated protostar. This excess was explained by a relatively warm ($> 200\,\mathrm{K}$) disk of material around the protostar (Adams & Shu 1986). A survey of 59 protostellar systems (Strom et al. 1988) in the Taurus-Auriga region revealed that 80% had a small (1.2 times) luminosity excess over what would be expected from a protostar, the proposed cause was a circumstellar disk. Additionally, 20% of the systems had a much larger luminosity excess and exhibited spectral energy distributions that were flat or rising toward larger wavelengths, strongly supporting the existence of a protoplanetary disk. Some of the systems also were observed to have UV excess emission, reasoned to be the result of accretion of material from the disk onto the central protostar. Noting the lack of self-absorbed spectral features from most protostars in a survey of around 35 systems, Cohen & Witteborn (1985) concluded that the geometry of the material is not a spherical shell and is likely a flattened disk. Another piece of evidence of the existence of disks was the bipolar outflows seen from protostars, first seen in the CO observations of the molecular cloud L1551 (Snell et al. 1980). Since then molecular outflows have been increasingly associated with protostars (Bachiller 1996), extending to distances of up to 5 parsecs. These features are often associated with rotating disks (Pudritz 1986).

The Infrared Astronomical Satellite (*IRAS*) allowed statistical studies

of disk occurrences to be made. Strom et al. (1989) surveyed the Taurus-Auriga star forming region and found that 60% of systems exhibited the infrared excess associated with circumstellar disks. Based on the ages of the systems, observed disk lifetimes were estimated between 3.0×10^6 and $\sim 10^7$ yr. Hα emission, whose strength is a measure of disk-to-star accretion, was observed to decrease with age, suggesting an evolutionary process between heavily accreting disks and disks exhibiting little to no accretion.

The modern, accepted picture of stellar formation is as follows. A molecular cloud in the galaxy composed largely of molecular hydrogen, helium, trace gases, and dust grains begins to collapse. The gas composition is complicated; molecules such as OH, H_2O, CO, CO_2, CN, HCO^+, and H_2CO have been detected with the *Spitzer Space Telescope*. For a complete discussion, see review by Williams & Cieza (2011). The dust species present include silicates, graphite grains, and polycyclic aromatic hydrocarbons (PAHs) (Draine 2003). These particles can be spectrally identified via their relatively wide bands in the IR (e.g. silicates at 10 and 18 μm (Henning 2010), PAHs at 3.3, 6.2, 7.7, 8.6, 11.2, 12.7, and 16.4 μm (Tielens 2008)).

Large clouds will fragment as they collapse, producing anywhere from dozens to hundreds of collapsing cloud cores, each of which could potentially form a star. These cloud cores continue to collapse in a non-homologous fashion (Larson 1969; Penston 1969a,b); the center of the cloud-core collapses more rapidly than the rest of the fragmented cloud due to the freefall timescale's dependence on mass density ($\tau = (G\rho)^{-1/2}$). This means that stellar densities are approached by the central protostar while the rest of the cloud is still in a configuration close to its initial conditions. A detailed analysis of the cloud material falling onto the disk has been performed by Cassen & Moosman (1981). They conclude that material will fall along

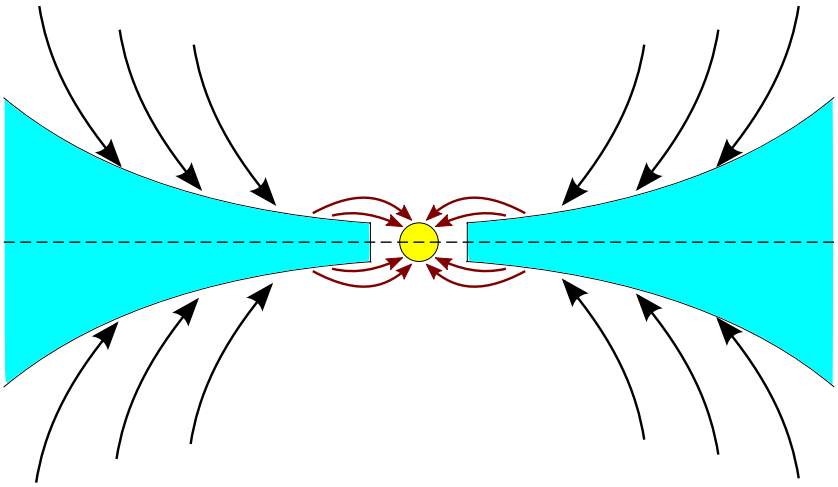

Figure 1.1: Model of a protostar with a flared protoplanetary disk accreting mass onto it. For the first few 10^4 years the disk is gaining material from the remains of the collapsing cloud fragment (black arrows) following trajectories described in Cassen & Moosman (1981). After the formation of the central protostar from the initial collapse of the cloud core, most of the star's mass gain is accreted from the disk via magnetospheric accretion(dark red arrows).

parabolic trajectories toward the disk. The trajectories become shallower as r increases. According to their model, the resulting disk will have a surface density which is highest at the inner edge and drops with r as a combination of a power law for inner regions with an exponential fallout at the outer edge. The size of the disk is dependent upon the viscosity of the infalling material. In order to conserve angular momentum, the remainder of the cloud collapses to form a circumstellar, protoplanetary disk (Adams et al. 1987). This is depicted in Figure 1.1, where a disk around a protostar is forming from cloud material.

After the initial collapse of the cloud-core's center to form the protostar, material moves from the dissipating cloud onto the disk, and then from the disk onto the protostar. Material on the inner edge of the disk is funneled along magnetic field lines onto the protostar. As this is happening, material is flowing through the disk to conserve angular momentum.

Material in the inner annuli is moving inward and mass in the outer region of the disk is moving outward. The boundary between the two regions is known as the "turn-around radius." This boundary moves outward as the disk ages (Bell et al. 1997). The position of the turnover radius, R_a, can be estimated using $R_a^2 = 0.75\nu t M_{\rm D}/\dot{M}$, where ν is the viscosity of the disk material, t is the age of the disk, $M_{\rm D}$ is the disk's mass, and $\dot{M}$ is the accretion rate of the disk material onto the protostar (Bell et al. 1997). Based on calculations performed by Bell et al. (1997), R_a varies between 1 and 100 AU depending on the viscosity and age of the disk.

Observationally, we cannot measure the rate of mass flow within the disk. However, the ultraviolet excess (Calvet & Gullbring 1998; Gullbring et al. 2000) and emission lines such as Hα (Muzerolle et al. 1998, 2001) can be used to measure the rate of accretion from the disk onto the star. If one were to assume a uniform accretion rate through the inner portions of the disk, then that rate of mass falling onto the protostar can be used as a proxy of mass flow through the disk. Simulations of the formation and early evolution of the disk suggest that bursts of mass accretion occur as the disk is forming (Machida et al. 2011; Vorobyov & Basu 2005, 2006). Accretion onto the disk from the cloud permits the fragmentation of the disk into chunks of material that fall onto the protostar. After accretion onto the disk has ceased, the models of Machida et al. (2011) demonstrate that initially there is a wide variation of accretion rates onto the protostar, ranging from $\sim 10^{-6}$ to $\sim 10^{-4}\,{\rm M}_\odot\,{\rm yr}^{-1}$. These models indicate that the rate of mass accretion is not constant and varies over periods of $\sim$100 yr. These stars can be difficult to observe directly due to the gas/dust envelope that the protostar/disk is shrouded in.

After material ceases accreting from the cloud directly onto the PPD,

the only flow of material in the system is gas and dust flowing from the disk onto the protostar. Material in the inner annuli of the disk interacts with the protostar's magnetic field which funnels material onto the star. Protostars in this phase are known as classical T Tauri stars (CTTS). Models of evolving disks around CTTS with varying masses have been compiled by Alexander & Armitage (2006). They show that the mass accretion rate from the PPD onto the protostar depends on both the mass of the protostar and the age of the disk. As the protostar's mass increases, the initial accretion rate of the system grows as well. They also demonstrate that the mass accretion rate decrease over the life of the disk. Alexander & Armitage (2006) show that for disks with ages $>10^5$ yr around protostars with $M_\star < 4\mathrm{M}_\odot$, accretion rates, $M_{\rm acc}$, are $\lesssim 10^{-7}\,\mathrm{M}_\odot\,\mathrm{yr}^{-1}$. They also propose that $\dot{M}_{\rm acc} \propto M_\star^2$. Hartmann et al. (1998) surveyed the Taurus and Chamaeleon I molecular cloud complexes, observing accreting protostars. The protostars observed all had masses $<1\,\mathrm{M}_\odot$ and $\dot{M} \lesssim 10^{-6}\,\mathrm{M}_\odot\,\mathrm{yr}^{-1}$. The youngest protostars surveyed had ages of $\approx 10^5\,\mathrm{yr}$. An analysis performed by Vorobyov & Basu (2008) demonstrated similar relations. Using previously compiled observational data of protostars with ages between 0.5 and 3 Myr in the Taurus, Chamaeleon I, and ρ Ophiuchus systems (Muzerolle et al. 2005; Natta et al. 2006) they demonstrated that the mass accretion rate onto the protostar increases monotonically both with protostellar mass and disk mass (time-averaged). Vorobyov & Basu (2008) found that $\langle \dot{M_{\rm acc}} \rangle \propto \langle M_\star \rangle^{1.7}$ and $\langle \dot{M_{\rm acc}} \rangle \propto \langle M_{\rm disk} \rangle^{1.1}$. Gullbring et al. (1998) determined via ultraviolet excess observations that for a set of 29 T Tauri stars of age $\sim$1 Myr, the range of accretion rates is $\dot{M}_{\rm acc} \sim 10^{-9} - 10^{-7}\,\mathrm{M}_\odot\,\mathrm{yr}^{-1}$.

After a period of time the disk will cease accreting material onto the protostar. The exchange of angular momentum in the disk has caused the

disk to become sufficiently spread out that the outer regions of the disk are unable to resupply the inner portions with material (Williams & Cieza 2011). The inner annuli will then become drained of mass over viscous timescales, creating a hole in the disk. The inner edge of the disk is now exposed to UV photons emitted from the protostar. These photons will evaporate the disk from the inside out, causing the central hole to grow with time. This idea has come to be known as the "UV-switch" model, where UV photoevaporation becomes important after the rate of protostellar accretion slows due to disk spreading (Alexander et al. 2006a,b; Clarke et al. 2001). The lack of accretion during this phase eliminates the spectrum's emission lines resulting from the disk to star accretion such as Hα. However, since the disk is still present for $r > r_{\rm inner}$, IR excess in the spectrum will remain. Disks like this are known as "transition disks."

The exact definition of a transition disk varies. Cieza et al. (2007) introduced a two-parameter scheme to observationally define them based on their spectral energy distributions (SEDs): a turnoff wavelength where the system's SED deviates significantly from that of a pure protostar, $\lambda_{\rm turn-off}$, and a slope of IR excess between $\lambda_{\rm turn-off}$ and 24 μm, $\alpha_{\rm excess}$. The most restrictive definition is a disk which has little to no near-infrared excess, significant far-IR excess, with a steep slope in the mid-IR range of the SED ($\lambda_{\rm turn-off} > 4.5 - 8.0\,\mu$m, $\alpha_{\rm excess} > 0$) (Muzerolle et al. 2010; Sicilia-Aguilar et al. 2010). Other definitions allow for a small amount of near-IR excess (Brown et al. 2007; Merín et al. 2010). A vocabulary describing the evolution within the group of transition disks has been developed based on the infrared SED slope and the amount of near-IR excess (see review by Williams & Cieza (2011).

Since the launch of IRAS, transition disks have been identified based

on their SEDs (Strom et al. 1989; Wolk & Walter 1996). Based on surveys of various star-forming regions (Scorpius, Ophiuchus, Taurus-Auriga, and Orion) it is currently thought that between 10% and 20% of disks in observed star-forming regions are in a transition stage (Currie et al. 2009; Dahm & Carpenter 2009; Fang et al. 2009; Hernández et al. 2007; Kim et al. 2009; Lada et al. 2006). Disks with IR excess but exhibiting $\alpha_{\text{excess}} < 0$ have been termed "weak-excess" disks and are seen to outnumber transition disks with a sharp inner hole by a factor of 2 or 3 (Cieza et al. 2010; Muzerolle et al. 2010) and are more common in older clusters (Muzerolle et al. 2010). For example, Najita et al. (2007) surveyed 60 pre-main sequence stars in Taurus. Twelve were found to have transition disks based on the above described SED qualities. Of those 12 transition disks, only 3 were deemed "classical transition disks," meaning the SED exhibits strong far-IR excess with positive α_{excess}; 7 were defined as weak-excess disks and the last 2 were described as pre-transition disks. It is currently unknown whether the low percentage of transition disks means that the transition phase is relatively short compared to the total lifetimes of PPDs or if it is simply uncommon for disks to evolve through that phase. However, given that no known process can eliminate a disk at all radii simultaneously, it stands to reason that all disks will dissipate from the inside out by whatever process causes the hole to grow, meaning that it is more likely that the transition phase is rapid in nature (Williams & Cieza 2011).

1.2 PPD Temperature Structure

Once formed, PPDs and the material in them will evolve. Many of the processes that determine the evolution of disks and the growth of solids within them rely on the temperature, including the condensation of elements (Lodders 2003), the disk chemistry (Najita et al. 2007), the formation of

meteoritic components (e.g. calcium-rich, aluminum-rich inclusions (CAIs), see Woolum & Cassen 1999), and the turbulent viscosity that drives the evolution of the disk. This viscosity is often modeled as an "alpha" viscosity $\nu = \alpha c_s^2/\Omega$, where α is a fixed dimensionless constant, Ω is the Keplerian orbital frequency, $c_s = (kT/\bar{m})^{1/2}$ is the sound speed, and $\bar{m}$ is the mean molecular weight of the gas (Shakura & Sunyaev 1973). In our treatment, the viscosity depends specifically on midplane temperature, $T_{\rm mid}$. Therefore, while modeling the formation of solids and the evolution of the disk requires known temperatures at all radii, r, and heights above midplane, z, midplane temperatures are especially important.

Temperatures in PPDs change over time. Some of these changes are slow, occurring over timescales of many Myr, much slower than the timescales for radiative diffusion (Rafikov 2007). PPDs subject to these evolutionary changes thus may be considered to be in steady state. In addition, PPDs are also characterized by sporadic decades-long heating events in the form of FU Orionis or EX Orionis outbursts (Bell et al. 2000; Herbig 2007). Transient heating events in which temperatures increase many hundreds of Kelvin, for years or even hours, are also well known to occur in PPDs, as exemplified by the existence of chondrules and annealed crystalline silicate grains (Connolly et al. 2006). These events have important consequences but must be modeled independently and must, in any case, be compared to the steady-state temperatures of PPDs, which is our focus here.

Disks in steady state (radiative equilibrium) balance cooling via emission of radiation against heating by various sources. For a parcel of disk material heating sources include external radiation from objects such as the protostar, radiation from other parts of the disk due to reprocessed radiation from external sources, viscous heating caused by turbulence within the disk,

and radioactive decay. D'Alessio et al. (1998) demonstrated that heating by radioactive decay is negligible compared to other sources and will be neglected in our treatment. Models of so-called "passive disks" (where viscous heating has been neglected) have been generated (Dullemond et al. 2002) where the only source of heating considered is external radiation and its reprocessed byproduct. However, for annuli with $r \lesssim 2$ AU turbulent heating can be significant to the disk's energy balance and must be included. Disks that are heated both by external radiation as well as viscous heating are known as active disks. Since our disks will have inner radii of < 2 AU, we will be modeling active disks.

Disk shape is an important parameter of PPD models. It regulates the amount of protostellar radiation that is intercepted by the upper layers of the disk. In general PPDs are considered to be geometrically thin, meaning that the local scale height is small compared to the radius, $H \ll r$. It is expected that disks will be in vertical hydrostatic equilibrium, $dP/dz = -\rho\,\Omega^2 z$. D'Alessio et al. (1998) demonstrated that other forces that act upon parcels of disk material, such as radiation pressure, are negligible compared to gravity. For a disk isothermal within a vertical column, the scale height trends as $H \propto T^{1/2}$. Disks do not have parallel top and bottom surfaces, nor is the H/r ratio uniform. Instead, PPDs are generally flared, with the disk's pressure scale height $H = c_{\rm s}/\Omega$ varying with distance from the star, r, as $r^{1+\eta}$, where $\eta > 0$ depends on and feeds into the midplane temperature, $T_{\rm mid}$ (Kenyon & Hartmann 1987). If the absorbing surface of the disk lies a height Z above the midplane, with Z/H a fixed constant (≈ 4), then the starlight absorbed per unit area of the disk varies as $dZ/dr - Z/r = \eta Z/r$ (see §2.1). Because $H \propto T^{1/2}$, warmer disks have larger Z, and therefore absorb more energy per area; likewise, disks that absorb

more starlight have higher temperatures. Analytic solutions are possible in some instances (e.g., a passive disk with Z/H fixed: Chiang & Goldreich 1997), but generally this feedback between the disk structure and the disk temperature has required sophisticated codes to be developed that simultaneously impose hydrostatic equilibrium in the vertical direction and solve iteratively for the disk temperature and disk flaring η, even in passive disks (e.g. Chiang et al. 2001; Dullemond et al. 2002).

Additional feedbacks are seen in active PPDs. In a disk where viscous dissipation dominates, the energy dissipated per disk area, per time, is $Q = (9/4)\Sigma\,\nu\,\Omega^2$, where Σ is the local surface density of the disk (Lynden-Bell & Pringle 1974). In a disk with radially uniform mass flow, the inward flow of mass in the disk is $\dot{M} = 3\pi\,\Sigma\,\nu$ (Lynden-Bell & Pringle 1974; Armitage 2007) and the heating rate per area is $Q = (3/4\pi)\dot{M}\,\Omega^2$. This heating is radiated from the surfaces of the disk with an effective temperature $T_{\rm eff}$ given by $2\sigma_{\rm SB}T_{\rm eff}^4 = Q$. It is common to convert the vertically-averaged heating rate Q into a local heating rate per volume, q, using the gas density ρ, as follows: $q = (9/4)\rho\nu\Omega^2$ (e.g. D'Alessio et al. 1998). The heating is readily seen to be more intense near the disk midplane, and a temperature gradient is required for the energy to reach the disk surface. In the radiative diffusion limit, the midplane temperature is given by $T_{\rm mid} = (8\tau_{\rm R}/3)^{1/4}\,T_{\rm eff}$, where $\tau_{\rm R}$ is the Rosseland-mean optical depth to the disk midplane (e.g. Hubeny 1990). Thus $\sigma_{\rm SB}T_{\rm mid}^4 \approx (\tau_{\rm R}/\pi)\,\dot{M}\,\Omega^2$. Feedbacks arise when $\dot{M}$ or $\tau_{\rm R}$ depend on temperature. Bell et al. (1997) considered realistic opacities and found that τ would increase with T in many temperature regimes. More direct positive feedbacks can exist as well because the turbulent viscosity increases linearly with temperature in the alpha parametrization of Shakura & Sunyaev (1973), in which the viscosity is $\nu = \alpha c_{\rm s}^2/\Omega$. (Other

parametrizations, notably the β viscosity in which $\nu = \beta r^2 \Omega$, do not increase with T (Davis 2003).) In the alpha viscosity formalism, greater temperatures generally lead to greater mass accretion rates and still higher temperatures.

It is important to note that α will not be spatially uniform within a disk, as has been considered by previous models (e.g. Bell et al. 1997). Past models of PPDs did not explore the possibilities of non-uniform α partly due to the unknown nature of the turbulence mechanism. Without this knowledge it is difficult to apply structure to the α parameter. In section 1.3 we will consider different angular momentum transport mechanisms and conclude that accretion is probably due to the magnetorotational instability. This mechanism requires a layered treatment of α, since if magnetorotational instability is responsible, the turbulence will be confined to the surface layers of the disk which can become more readily ionized.

We are strongly motivated to study the temperatures of PPDs, especially at their midplanes, in disks that are actively accreting only in surface layers. To our knowledge, the temperature structure of disks undergoing layered accretion has not yet been studied. It is straightforward to show that such disks can be significantly cooler at their midplanes, compared to disks undergoing uniform accretion. No energy is generated within the dead zone, so within each annulus the dead zone should be roughly isothermal vertically, with temperature equal to that at the base of the active layer. The active layer resembles a uniformly accreting disk, except that at each heliocentric distance the accretion is concentrated into two layers, each with surface density $\Sigma_{\rm a}$ (instead of half of the full surface density of the disk, or $\Sigma/2$). This division has little effect on the temperature at the disk surface, which is still set by $2\sigma_{\rm sB} T_{\rm eff}^4 = Q = (3/4\pi)\dot{M}\Omega^2$. The midplane temperature, on the other hand, is greatly affected, since

$T_{\rm mid} = (3\tau/8)^{1/4}\, T_{\rm eff}$ and τ through the active layer is proportional to $\Sigma_{\rm a}$. A PPD with dead zone and active layer typically has $\Sigma_{\rm a} < 10^2\,{\rm g\,cm^{-2}}$, much smaller than the full column density through the disk ($\Sigma \sim 10^4\,{\rm g\,cm^{-2}}$ in the innermost few AU). The midplane temperature could in principle be reduced by the significant factor $(\Sigma/2\Sigma_{\rm a})^{1/4} \sim 3$ (at least in annuli dominated by viscous heating). The positive feedbacks mentioned above can further amplify this temperature reduction: reduced disk flaring reduces absorption of star light, and the cooler temperatures also reduce the opacity and further decrease τ. To accurately compute the temperatures at PPD midplanes, one must consider the nonuniform nature of the accretion.

In this paper we calculate the temperatures of PPDs in hydrostatic and radiative equilibrium, in which the heating is a combination of absorption of starlight and nonuniform, layered accretion. We present an algorithm for the computation of disk temperatures, based on Rybicki's method commonly used for study of stellar atmospheres. Interestingly, it appears that this method has not previously been applied to the problem of PPD temperatures. This algorithm is well suited to finding temperatures in very optically thick disks ($\tau \gg 10^4$). We apply this code to the problem of temperatures in PPDs undergoing layered accretion, considering cases in which either $\dot{M}$ or α is held fixed while the active layer thickness $\Sigma_{\rm a}$ is changed.

1.3 Angular Momentum Transport Mechanisms

As discussed in the previous section, we are treating accretional heating as a turbulent α-viscosity. We also noted that observations do not yet exist to yield accurate measurements of mass flow through the disk, making it difficult to ascertain the mechanism responsible. In an effort to learn the

source of turbulence, extensive modeling has been conducted to test various mechanisms. Here we review three mechanisms that have been modeled: convection, gravitational instability, and the magnetorotational instability.

Convection

One of the early mechanisms considered for the source of the turbulence was convection. (A thorough review of our evolving understanding of convection's role, or lack thereof, can be found in Klahr (2007).) Briefly, it was first suggested by Cameron (1978) that thermal convection could be responsible for generating the turbulence that leads to accretional heating and the evolution of the disk. In order for convection to be a primary cause, super-adiabatic vertical temperature gradients would be required in disk regions where significant gas pressure gradients are present. However, it was recognized by Cameron (1978) that in many cases, the vertical temperature gradient will be sub-adiabatic; only in situations where $T_{\rm mid} > 2000$ K would vertical temperature gradients be expected to become super-adiabatic. This implies that in most areas of the disk, conditions will not be correct for convection to drive turbulence.

However, even assuming conditions are present for convection, the effects are opposite what are needed to evolve the disk. Under the assumption that vertical convection is primarily responsible for disk turbulence, Canuto et al. (1984) derived a formula for α and determined that for a PPD, the viscosity parameter is dependent on the radius and temperature of the location in the disk in question. In an attempt to model the early solar nebula under this assumption, models were developed using these derived values of α (Cabot et al. 1987a,b). The conclusion drawn from these models is that α due to convection tends to be low and a function of

both opacity and the disk's surface density. This leads to an "inverse accretion rate" with respect to surface density, which decreases with r. The model produces a disk which breaks into rings. They conclude that convection cannot be the dominant source of turbulence in protoplanetary disks.

Bell & Lin (1994) demonstrated with one-dimensional analytical models that the disk opacity will vary with the temperature. They defined a power law opacity of the form $\kappa = \kappa_i \rho^a T^b$ and concluded that only for $b > 1$ would a convective instability be possible. This corresponds to 2 temperature regions: $2,000\,\mathrm{K} \lesssim T \lesssim 20,000\,\mathrm{K}$ and a narrower region located at $T \approx 200\,\mathrm{K}$. These conclusions were consistent with those of Cameron (1978) and support the idea that persistent turbulence due to convection is difficult to achieve in PPDs.

Stone & Balbus (1996) calculated in three dimensions the effects of convection in a shearing-sheet approximation (ZEUS3D code). They found that in an initially unstable, vertically stratified disk layer steady convection produces α values that average out over many orbits (40+) to -4.2×10^{-5} (the negative sign indicates an *inward* movement of angular momentum). Stone & Balbus (1996) also concluded that convective turbulence is not self-sustaining and does not lead to outward transport of angular momentum.

Klahr et al. (1999) and Klahr & Bodenheimer (2003) created three dimensional simulations of thermal convection. While α values in the range $10^{-3} - 10^{-2}$ were found, convection could not be sustained unless a separate heating source at the midplane were present (i.e., the convection could not be self-sustaining). They also observed in their models the same fragmentation into rings seen by Cabot et al. (1987b). The conclusion again was that convection cannot be the sole source of turbulence in accreting

PPDs. A different mechanism must transport angular momentum and mass in protoplanetary disks.

Gravitational Instability

Another possible explanation for how material moves through the disk (and thus exchanges angular momentum) is the gravitational instability, or GI. As reviewed in Stone et al. (2000), the GI will be triggered when the local mass density exceeds a critical value. Finding this critical mass density value involves using what is known as the "Toomre parameter," which is commonly expressed by Q. (This use of Q should not be confused with Q used in the previous section to describe heating integrated over a vertical column.) The expression for Toomre's parameter is as follows:

$$Q = \frac{c_{\rm s}\Omega}{\pi G\Sigma}, \tag{1.1}$$

where $c_{\rm s}$ is the local sound speed, Ω is the Keplerian frequency, G is the gravitational constant, and the disk's local surface density is represented by Σ. When $Q < 1$, the patch of disk being described is gravitationally unstable.

If we consider a fairly standard disk, we can evaluate the likelihood of the gravitational instability playing a major role in mass flow through the disk. Quantities such as surface density, Σ, and temperature, T, can be approximated by power laws. Typical analytical expressions are $\Sigma = 10^4\,(r/1\,{\rm AU})^{-p}\ {\rm g\,cm^{-2}}$ and $T = 300\,(r/1\,{\rm AU})^{-q}\ {\rm K}$, where $p = 3/2$ and $q = 1/2$. A typical protostar has $M_\star \sim 0.5\,{\rm M}_\odot$. Using these adopted values, and solving for Q, we find that the disk will be gravitationally stable out to 300 AU.

This does not mean that the GI plays no role in PPD evolution. It is reasonable that while a PPD might find itself gravitationally stable for a majority of the time, processes that move mass between annuli could

eventually cause a GI to be triggered. While only small portions of the disk may become gravitationally unstable, it has been shown that even locally induced GI events can affect the remaining, largely stable, portions of the disk (Laughlin & Rozyczka 1996). The obvious observed candidates for such an event are the short, heavy outbursts seen in disks such as FU Orionis (Hartmann & Kenyon 1996) and EX Orionis type events. The frequency and duration of FU Orionis and EX Orionis outburst events suggest that GIs punctuate the evolution of PPDs that are otherwise accreting mass in a non-uniform matter, until sufficient mass has accumulated (Bell et al. 2000), leaving unanswered the question of what moves material in the disk to trigger them in the first place.

Magnetorotational Instability

Over the last two decades, attempts to specify the cause of the turbulent viscosity in protoplanetary disks have increasingly converged on one mechanism: the magnetorotational instability, or MRI (Balbus & Hawley 1991, 1998). In a disk threaded by a magnetic field, different parts of the disk can exchange angular momentum via magnetic forces, leading to turbulent viscosity very much like that parametrized by Shakura & Sunyaev (1973). The stress tensor defined therein scales with gas pressure as $T_{r,\phi} = \alpha p$, so that the viscosity depends on temperature (Balbus & Hawley 1998). Where the instability is triggered, α as high as 0.1 has been reported in some numerical simulations (Pessah et al. 2007). It is not immediately clear what value of α is appropriate for PPDs, but a vertically mass-averaged $\alpha \sim 10^{-2}$ is consistent with observed disk properties (Hartmann et al. 1998; Hueso & Guillot 2005), although that value comes with a caveat. The models used to arrive at $\alpha \sim 10^{-2}$ assumed that the disk exhibited accretional heating at all r and z at a uniform α. As will be explored in this section, modeling the

MRI requires a layered accretion model. Within a vertical slice, α will have two different values: an active layer value, $\alpha_{\rm a}$, and a dead zone value, $\alpha_{\rm dz}$. We consider the range $10^{-4} < \alpha_{\rm a} < 1$ to be likely for the active layers.

More clear is the fact that the MRI will not act uniformly in PPDs. The triggering of the MRI requires an instability criterion to be met (see Desch 2004 and references therein). The most stringent condition is the requirement that Ohmic dissipation be weak enough to not suppress the instability. The threshold level for Ohmic dissipation was discovered by Jin (1996), and a useful rule of thumb is that for the MRI to act, the ionization fraction of the gas must satisfy $n_{\rm e}/n_{\rm H2} > 10^{-13}$, where $n_{\rm e}$ and $n_{\rm H2}$ are the number densities of electrons and H_2 molecules respectively (Gammie 1996). This is a low ionization threshold by astrophysical standards, but even so is not met everywhere in PPDs. Since recombination rates of electrons and ions scale as $n_{\rm e}^2$ (assuming $n_{\rm e} = n_{\rm ion}$), but ionization rates driven by protostellar X-rays and galactic cosmic rays scale as $n_{\rm H2}$, it is easily seen that $n_{\rm e}/n_{\rm H2} \propto n_{\rm H2}^{-1/2}$, and the MRI will be suppressed by Ohmic dissipation where the density is sufficiently high. Gammie (1996) first pointed out that densities in PPDs are high enough to suppress the MRI at their midplanes, leaving the MRI to preferentially occur in "active layers" at the surfaces of PPDs, sandwiching inactive "dead zones" near the disk midplanes. This is illustrated in Figure 1.2. Sano et al. (2000) estimated that these dead zones would extend out to $\approx$20 AU, between active surface layers only $\sim 10\,{\rm g\,cm^{-2}}$ thick (assuming X-rays are primary ionization source). The MRI is considered the mechanism most likely to be causing turbulent viscosity and viscous dissipation in protoplanetary disks. The implication is that viscous dissipation occurs non-uniformly in PPDs.

The magnetorotational instability operates as follows: If a PPD has a

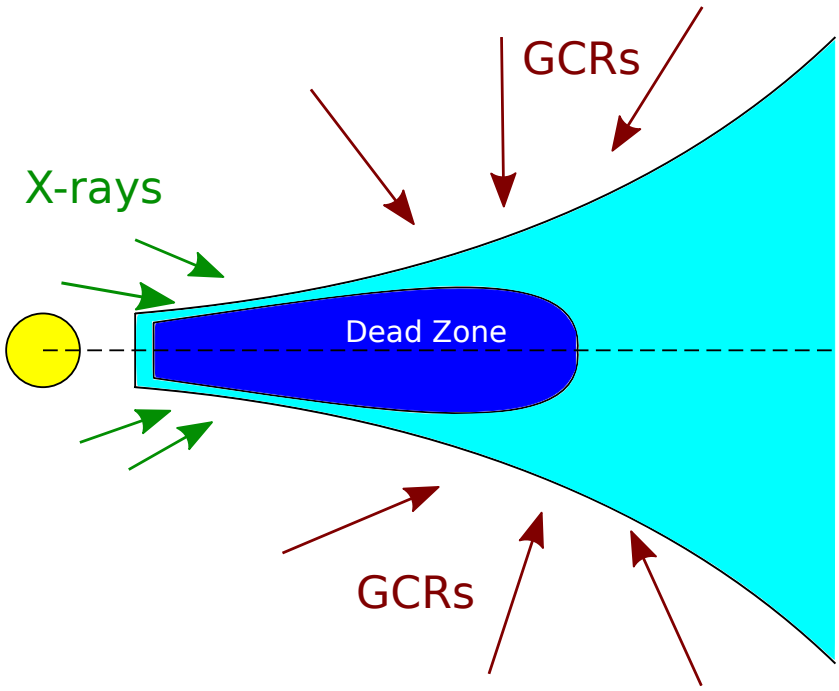

Figure 1.2: Cross section of a protoplanetary disk. Shown is the dead zone first suggested by Gammie (1996) (dark blue). The remainder of the disk is active (light blue). The two major sources of ionization are illustrated as well. Protostellar X-rays (green arrows) dominate at small r. Galactic cosmic rays (dark red arrows) dominate at large r.

magnetic field running through the disk, then particles with non-zero charge will be induced to gyrate about the field lines. Fluctuations in the magnetic field will cause motions of particles within the disk, as charged species will tend to follow the field lines. If a perturbation in a magnetic field line is propagating through the disk, then particles that were initially at radius $r = r_0$ will be shifted to $r = r_0 + \epsilon$, where ϵ is some small perturbation. Figure 1.3 illustrates this. Assuming a simple case for the moment, the direction of $\mathbf{B}$ is parallel to the disk's rotation axis and the field is co-rotating with the disk. That means that before being disrupted, particles "attached" to a particular field line as well as the field line itself are all rotating about the protostar at the same speed, where v is determined by the appropriate Keplerian frequency at that radius.

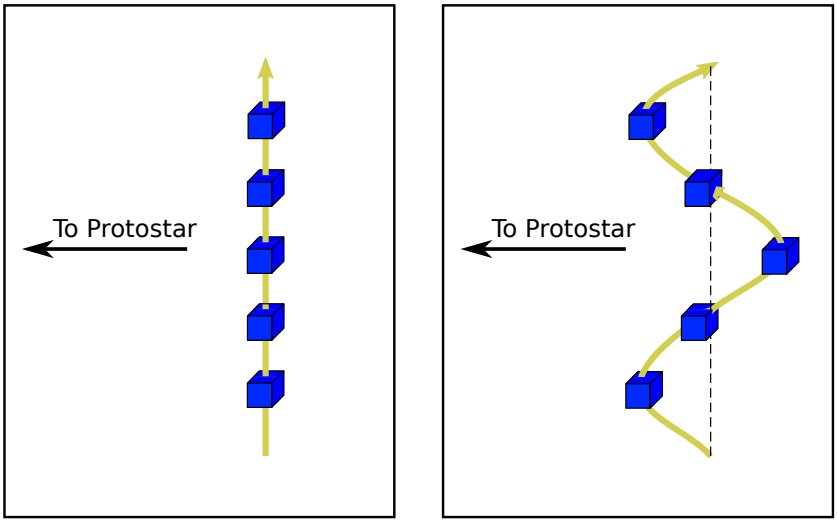

Figure 1.3: Side view of an annulus of a PPD with a magnetic field parallel to its rotation axis. Left: parcels of ionized gas (shown in blue) are frozen to the field line (yellow). Right: the same annulus of the disk after a perturbation to the magnetic field has been introduced. The ionized gas frozen to the field line is perturbed with the field line; some of the gas is now at a smaller distance from the protostar than it was initially, other parcels are further away.

After the disruption, that no longer will be true. The particles will be traveling through the disk at a range of speeds, as is appropriate for particles orbiting a protostar at various radii. The charged particles that are at smaller r will feel a stronger gravitational tug and will want to move faster, while particles at larger r will feel a weaker tug and move slower, as shown in Fig. 1.4. However, these particles are all still "frozen" to the same magnetic field line, causing the field line to be stretched, creating potential energy like a stretched rubber band. The radial component of the magnetic tension serves as a restoring force, attempting to bring the charged particles back to their initial radius. However, due to the disk's differential rotation, there is an azimuthal component as well. This component trades angular momentum between the elements; the outer, slower moving elements gain angular momentum at the expense of the inner, faster moving elements. And while the radial component is stabilizing, the azimuthal component is destabilizing.

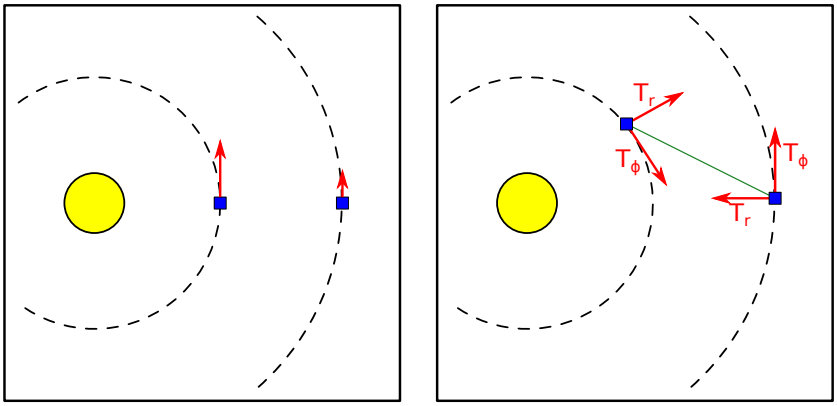

Figure 1.4: Overhead view of the disk after a magnetic field line with gas frozen to it has been disrupted. Left: the parcels have just been perturbed and are at different radii. Right: after some time the parcels have shifted angularly relative to each other. The stretched field line applies a tension force to the gas frozen to it. There are two components to the tension force, radial and azimuthal.

As the angular momentum is traded, the outer parcel will move even further out, and the inner parcel will move further in. This exacerbates the orbital speed differential, stretching the field line connecting them more and increasing the tension. At this point, one of two outcomes will occur. If the magnetic field is strong enough, it will overcome the destabilizing effects and pull the charged particles back to their initial radius. However, if the magnetic field isn't sufficiently strong to achieve this, the particles will get caught in a feedback loop: Shearing further and further apart, putting more and more stress on the magnetic field line.

The seminal work of Balbus & Hawley (1991) investigated the various modes of the MRI. Goodman & Xu (1994) analytically studied the stages of the instability in the nonlinear regime after its formation. Specifically, what happens to the amplitudes of the unstable modes after their formation by magnetic field perturbations. Modes of instability with wavevectors that are parallel to the PPD rotation axis were found to behave similarly whether the magnetic fields were assumed to be incompressible or not. When

incompressibility is assumed they found that the strength of the MRI is subject to 2 "parasitic instabilities" which can make it stronger or weaker. One of the instabilities they found was identified as a Kelvin-Helmholtz instability. Goodman & Xu (1994) also found that relatively weak fields parallel to the rotation axis can evolve into toroidal fields due to these parasites with growth rates of $\omega \propto v_R/\lambda_z \propto sB_R/B_z$, where v_R is the radial velocity, λ_z is the wavelength of the unstable mode, s is the growth rate of the mode, and B_R and B_z are the magnetic field components in the radial and vertical directions, respectively.

Gammie (1996) and Zhu et al. (2010) suggest that material in some protoplanetary disks exchanges angular momentum via the MRI and over time mass accumulates in certain annuli. When enough mass has accumulated in an annulus to drive $Q < 1$, this will trigger a gravitational instability. An understanding of the MRI and how it will act on a disk is important to determining where and when a GI will be initiated. By modeling these disks, we can calculate $\dot{M}_r(r)$ through the disk and find $\dot{\Sigma}(r)$. This will allow us to calculate the timescales required for annuli gaining mass to become gravitationally unstable and for annuli losing mass to evacuate all of their disk material.

In computing the ionization chemistry of the disk, the density and temperature of the disk at all locations must be known. The temperature of the active layer will depend upon the strength of the accretion, which in turn depends upon the ionization. This introduces one of many feedback mechanisms in the disk. This problem will best be solved by a numerical simulation which relaxes to a converged solution by iterating. Based on the strength of the magnetic field and the degree of ionization present in the disk's active layers, the effects of ambipolar diffusion, Ohmic dissipation, and

the Hall effect need to be computed so as to determine what active layer thickness will be necessary for the disk to become unstable and transfer mass.

1.4 Purpose

We have defined unresolved questions regarding accreting protoplanetary disks. Much work has been done to analytically and numerically model the temperatures of disks and their SEDs, however, the calculations have omitted aspects of the disk such as the layered nature of accretional heating and its potential effects on temperatures at the midplane. We intend to include those concepts in order to generate more robust models. In Chapter 2 we lay out our algorithm for calculating the temperature structure of the disk at all radii and heights, with a focus on the midplane temperatures. Our models will be presented in Chapter 3. We will present results for passive, fully active, and layered accretion disks and explore the effects of restricting turbulent heating to the disk's upper layers. The question of whether SEDs can be expected to yield accurate midplane temperatures will be tested.

The effects of the ambient magnetic field strength will be tested as well. In particular, we self-consistently compute what thickness of active layer can be expected for PPDs and what the resulting mass flow rates are throughout the disk. Critical to making those calculations is an ionization chemistry network which correctly simulates the PPD environment. Chapter 4 contains a description of the algorithms used in determining the susceptibility of the disk to the MRI as well as the ionization chemistry we use. The results of our MRI analysis are in Chapter 5. We test 2 different surface density profiles as well as a range of viscosity parameters (α) and magnetic field strengths. Finally, in Chapter 6 the results from our study of layered accretion's effects on temperature and of the disks' susceptibility to

the MRI will be analyzed and discussed. The possibilities for future work will be set forth as well.

Chapter 2

CALCULATING PPD TEMPERATURE STRUCTURE

2.1 Background

Solving for the temperature structure of a PPD is a difficult task in radiative transfer. Dust grains in one part of the disk will absorb infrared radiation emitted by dust grains in all other parts of the disk, coupling temperatures across large distances. Worse, the geometry of the disk is two-dimensional (axisymmetry is usually assumed), with the vertical structure of the gas depending on the scale height and midplane temperature. These quantities in turn depend on the disk flaring angle and the radial structure of the disk. Simple arguments, first advanced by Kenyon & Hartmann (1987), show that the density and temperature structures are tightly coupled. Assuming hydrostatic equilibrium at each annulus, so that the gravitational force per volume acting on gas a height z above the midplane, $-\rho_{\rm g}\Omega^2 z$, is balanced by the pressure gradient force, $-\partial P/\partial z$, we can quickly find a solution for ρ if we also assume an isothermal gas (i.e. $P = \rho c_{\rm s}^2$). The familiar relation $\rho(z) = \rho(0)\ \exp(-z^2/2H^2)$, where $H = c_{\rm s}/\Omega$, is thus achieved. Therefore, density depends on temperature through the scale height H, $\propto T^{1/2}$. The $\tau = 1$ "photosphere" of the disk generally lies at a height $Z \approx 3 - 5\,H$ above the midplane. If this surface were oriented normally to the incoming starlight, then the disk would absorb a flux $L_\star/(4\pi r^2)$; but because the disk surface is nearly edge-on as seen by the star, the disk absorbs a much smaller flux of radiation, reduced by a factor $\cos\theta$, where θ is the angle the incident starlight makes relative to the normal to the disk normal. Simple geometric arguments show that $\cos\theta \approx dZ/dr - Z/r$, so that the heating rate per disk area scales as $r^{-1}d(Z/r)/dr$. Thus the heating rate and temperature of the

disk likewise depend on the density structure. In equilibrium, the heating rate per disk area must balance the emitted flux, which is proportional to $T_{\rm eff}^4$. If the disk is passive and vertically isothermal in each annulus, then $T_{\rm mid} \approx T_{\rm eff}$, so that $T(r)^4 \propto r^{-1} d(T^{1/2} r^{3/2} r^{-1})/dr$, or $T^{7/2} \propto r^{-3/2}$. This leads to $T(r) \propto r^{-3/7}$, and $H(r) \propto r^{9/7}$ (Chiang & Goldreich 1997), justifying the above assumption that $H(r) \propto r^{1+\eta}$, where $\eta = 2/7 \approx 0.29$. It also demonstrates that the temperature and the density structure depend on each other, requiring special techniques for their solution.

To solve for temperature and density structures simultaneously, many algorithms adopt an approach like that of Dullemond et al. (2002). This entails fixing the density structure within an annulus, then solving for vertical temperatures by assuming a 1-D, plane-parallel slab geometry. The updated temperature structure and the assumption of hydrostatic equilibrium are then used to solve for a new density structure in each annulus. Updates to the temperature structure also affect the variation of Z (height of absorbing disk surface) with r and the disk flaring, leading to a new heating rate driven by absorption of starlight. Therefore, after the density and temperature structures are solved for in each annulus, a new flaring index must be computed, and the entire calculation iterated to convergence. The weakly coupled series of 1-D slab-geometry radiative transfer calculations has been termed a "1.5-D" calculation by Dullemond et al. (2002). The geometric configuration of our 1.5-D grid is presented in Figure 2.1. This overall approach works well, but many codes differ in how they calculate the vertical temperature structure of each actively accreting, externally illuminated 1-D slab.

The last two decades have seen concerted efforts to quantify the vertical temperature structure. Some of the pioneering papers on disk

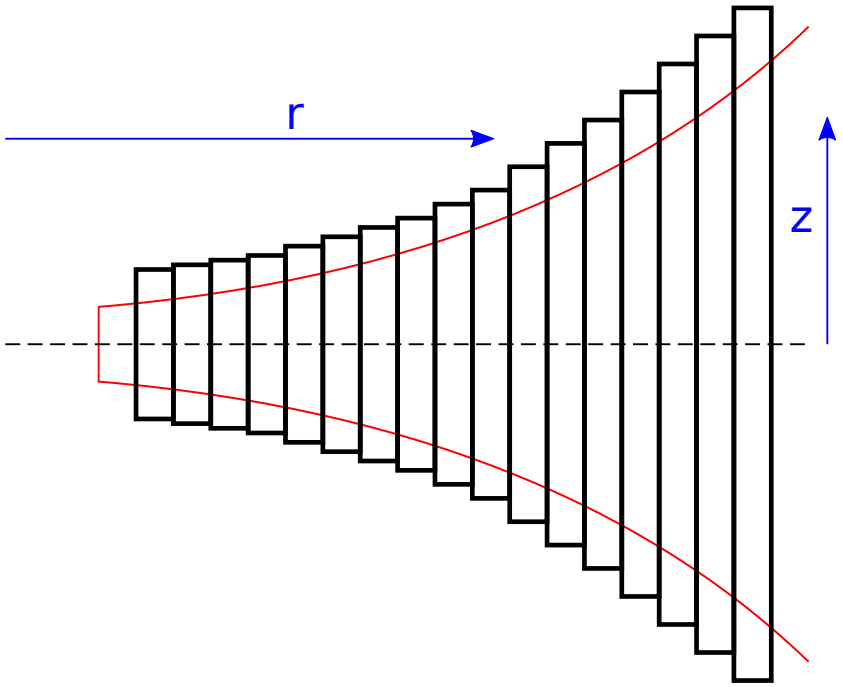

Figure 2.1: The 1.5D computational grid used. Each annulus has its vertical structure determined independently of the others, and the flaring index is recomputed after each pass through the disk's annuli. Overlaid in red is the disk's outline.

temperatures ignored the vertical structure of the disk. In their seminal paper on disk flaring, Kenyon & Hartmann (1987) assumed a uniform temperature, and in their work on the effects of superheated dust on disk spectra, Chiang & Goldreich (1997) and Chiang et al. (2001) considered only two uniform-temperature layers, an isothermal disk with an optically thin layer at the disk surface directly exposed to starlight. An isothermal disk is expected for a truly gray opacity, but vertical temperature gradients are expected when using wavelength-dependent opacities. Dust grains deep in the disk absorb mostly local radiation but tend to emit at longer wavelengths for which the opacity is lower, and radiation can more freely escape the slab. These effects are seen even when using frequency-integrated opacities, because quantities like the Planck-averaged opacity will depend on temperature. To calculate these effects, Hubeny (1990) found an analytic

form for the temperature structure of active disks that includes accretional heating. Calvet et al. (1991) and Malbet & Bertout (1991) found similar formulas in the case of irradiated accretion disks. Approximations to these formulas were used by Bell et al. (1997) in their calculations of disk temperatures, using frequency-averaged opacities that approximated solar nebula dust. D'Alessio et al. (1998) did not use analytic expressions to determine the vertical temperature structure, instead calculating the frequency-integrated mean intensities, $J_{\rm d}$, and fluxes, $F_{\rm d}$, at each height z above the midplane, using the following formulas:

$$\frac{dF_{\rm d}}{dz} = 4\pi\kappa_{\rm P}\rho\left(\frac{\sigma_{\rm SB}T^4}{\pi} - J_{\rm d}\right) \quad (2.1)$$

$$\frac{dJ_{\rm d}}{dz} = -3\chi_{\rm R}\,\rho\,\frac{F_{\rm d}}{4\pi}, \quad (2.2)$$

where $\kappa_{\rm P}$ and $\chi_{\rm R}$ are the Planck- and Rosseland- averaged opacities, and the Eddington approximation has been used to close the moment equations. (The subscript d refers to the disk radiation field only. D'Alessio et al. (1998) considered other fluxes that transport energy, but focusing on just these terms captures the spirit of the calculation.) D'Alessio et al. (1998) used these equations to solve for $F_{\rm d}$ and $J_{\rm d}$ at all heights, treating the equations as a two-boundary eigenvalue problem; the temperature was then found essentially from $\kappa_{\rm P}\sigma_{\rm SB}T^4/\pi \approx \kappa_{\rm P}J_{\rm d} + q/4\pi$, where q is the net heating rate per volume. Stellar radiation was included by calculating its attenuation through the upper disk, and including absorbed radiation as an effective increase in q.

Dullemond et al. (2002) used the same equations as D'Alessio et al. (1998), again using frequency-integrated variables. They used an iterative approach to solve for the vertical temperature structure. Some key differences are that Dullemond et al. (2002) did not necessarily assume the Eddington approximation to close the moment equations, instead using ray

tracing to calculate the (frequency-integrated) Eddington factor, f, at each height (they found the Eddington approximation turns out to be sufficiently accurate, making a difference of only a few percent in the midplane temperatures). Another difference is that Dullemond et al. (2002) integrated the equations of hydrostatic equilibrium and updated the density structure in a separate iterative step, whereas D'Alessio et al. (1998) updated density and temperature simultaneously. Also, whereas D'Alessio et al. (1998) included heating from accretion (and incorporated convection as well), Dullemond et al. (2002) considered only passive disks (for which convection is not important). An important difference of the Dullemond et al. (2002) approach lies in the way they handled frequency-integrated opacities. Instead of using the approximate Planck-averaged opacity $\kappa_{\rm P}$, they used the opacity weighted against the actual radiation field, $\kappa_{\rm J}$, and instead of using a term like $\kappa_{\rm R}H$ (the Rosseland opacity times the frequency-integrated Eddington flux), they used $\int_0^\infty \kappa_\lambda H_\lambda d\lambda$. A surprising result of their calculations was the difference this change made in the computed midplane temperatures at high optical depths. For their canonical case, midplane temperatures at 1 AU dropped from 100 K (using $\kappa_{\rm P}$ and $\kappa_{\rm R}$) to 65 K (using $\kappa_{\rm J}$ and $\int_0^\infty \kappa_\lambda H_\lambda d\lambda$). This result shows that subtle changes in how the frequency-dependent opacity is handled can have a major impact on the predicted midplane temperature, and that a calculation of the full frequency-dependent radiation field is warranted.

More recently, other approaches based on Monte Carlo methods have been taken to find the vertical temperature structures of PPDs. A number of authors (Bjorkman & Wood 2001; Stamatellos & Whitworth 2003; Whitney et al. 2003a,b, 2004; Dullemond & Dominik 2004; Niccolini & Alcolea 2006; Jonsson 2006; Robitaille et al. 2006) have simulated the absorption of stellar

radiation by propagating discrete packets of radiation in a Monte Carlo fashion. The advantage of this method is that arbitrary disk geometries can be considered. Monte Carlo methods also allow for easier inclusion of complex scattering functions and for the polarization of the radiation field to be computed. The disadvantage of the Monte Carlo approach is that it is improbable for radiation to propagate many optical depths into the disk interior, so large numbers of radiation packets must be included to obtain sufficient statistics on the radiation field of deep interior points. As the number of radiation packets is limited by computing resources to $< 10^8$, and because the fraction of packets that diffuse to optical depths τ is $\propto 1/\tau^2$, in practice the Monte Carlo method is limited to situations where $\tau < 10^4$. To circumvent this problem, some hybrid algorithms have been developed that use the Monte Carlo approach in the optically thin limit and transition to a temperature structure calculated using other techniques (e.g., that of Dullemond et al. 2002) in the optically thick region, or use other means to accelerate the calculation in the radiative diffusion limit (Min et al. 2009; Andrews et al. 2009; Robitaille 2010)). Comparisons between various codes on benchmark problems can be found in Pascucci et al. (2004) and Pinte et al. (2009).

Although these approaches are valuable, they tend to place a premium on predicting emergent spectral energy distributions (SEDs) from protoplanetary disk systems, as opposed to accurate midplane temperatures. In light of the large volume of high-quality infrared spectra of protoplanetary disks made possible by the *Spitzer Space Telescope* this focus is entirely understandable. Since the midplane temperatures are effectively masked by many optical depths of dust in the disk, an accurate prediction of SEDs does not require more than a reasonable approximation of the midplane

temperature in order to define the scale height of the disk. However, if the focus of the simulation is to accurately predict the chemistry of the disk's midplane, for example, the formation of CAIs, then a more accurate midplane temperature is paramount. This point was recognized by Woolum & Cassen (1999), who used SEDs of T Tauri stars to estimate $T_{\rm mid}$. The high temperatures associated with CAIs and a possible globally hot solar nebula occur only early in disk evolution, when accretion rates are high enough to be significant. We therefore seek an algorithm that readily computes the propagation of radiation at the disk midplane, i.e. at high optical depth, in a disk experiencing significant and spatially nonuniform accretional heating.

2.2 Justification for 1.5 D model

A fundamental assumption underlying the 1.5 D approximation is the neglect of radial radiative fluxes when computing the radiative equilibrium of an annulus. Assume an annulus, with inner and outer radii r and $r + \Delta r$, and total vertical thickness $2H$, has a total energy content E. The time rate of change of E due to radiative fluxes at the top of the disk (by symmetry all fluxes are zero at the midplane) is

$$\frac{dE}{dt} = \pi r \, \Delta r \int_{\lambda=0}^{\infty} F_z(\lambda) \, d\lambda$$

where $F_z(\lambda)$ is measured at the top of the disk. This equation represents the rate of energy absorption for half of the disk (e.g. the top half). Radiative equilibrium demands that $dE/dt = 0$ and that the wavelength-integrated fluxes in all directions are zero. So, for example,

$$\int_{\lambda=0}^{\infty} F_\lambda(z) \, d\lambda = 0$$

for all z. At some (longer) wavelengths the flux is upwards, at other (shorter) wavelengths it is downward, but integrated over wavelength the net flux is zero. This is imposed in our calculation.

What we do not account for in our calculation are the radial radiative fluxes $F_r(\lambda)$. These potentially matter because radiation can enter or leave each annulus, leading to a change in energy:

$$\frac{dE}{dt} = 2\pi r(2H)\big|_r \, F_r(r) - 2\pi(r+\Delta r)(2H)\big|_{r+\Delta r} \, F_r(r+\Delta r) \qquad (2.3)$$

or

$$\frac{dE}{dt} = 2\pi(\Delta r)\,\frac{\partial}{\partial r}\left(r(2H)F_r(r,\lambda)\right),$$

where we are using the wavelength-integrated radial flux. Putting it all together,

$$\frac{dE}{dt} = 2\pi r\,\Delta r\,\left(F_z^\star + F_z^{\rm disk}\right) + 2\pi(\Delta r)\,(2H)\frac{\partial}{\partial r}\left(rF_r(r)\right).$$

Here $F_z^\star$, $F_z^{\rm disk}$, and F_r are wavelength-integrated, and F_r represents a vertically-averaged quantity (just as the F_z terms represents a radially-averaged quantity). $F_z^\star$ is the short-wavelength radiation adsorbed from the star; this value is negative. $F_z^{\rm disk}$ represents the longer-wavelength radiation absorbed from the disk's thermal radiation and is positive. The sum of the two vertically averaged quantities, $F_z^\star + F_z^{\rm disk}$ is unknown.

If radial fluxes are indeed negligible, then $F_z^{\rm disk} = \sigma T_{\rm eff}^4$ and $T_{\rm mid} \sim \tau^{1/4} T_{\rm eff}$. Neglect of the radial fluxes is justified if $\left|F_r^{\rm disk}\right| \ll \left|F_z^{\rm disk}\right|$. To the extent that radial fluxes are not negligible, the fractional change in both $T_{\rm eff}$ and $T_{\rm mid}$ will be $\epsilon \equiv \left|F_r^{\rm disk}\right| / \left|F_z^{\rm disk}\right|$. Under the assumption that radial fluxes vary on lengthscales comparable to r itself, we find

$$\epsilon \approx \frac{2\pi\,\Delta r\,2HF_r^{\rm disk}}{4\pi\,\Delta r\,rF_z^{\rm disk}} = \frac{H}{r}\frac{F_r^{\rm disk}}{F_z^{\rm disk}}$$

Neglect of radial fluxes requires $\epsilon \ll 1$, or $F_z^{\rm disk} \gg (H/r)F_r^{\rm disk}$.

Now, the vertically averaged radial flux is dominated by the flux at the midplane (temperatures are highest there), where $F_r \sim 4\pi\,\partial B/\partial\tau$, where

τ is the optical depth in the radial direction, or $F_r \sim 4\pi B/(\kappa r)$, where again we have assumed that radial variations in temperatures take place over lengthscales comparable to r. Here κ is the opacity. Using $B \sim \sigma T^4/\pi$, we have $F_r \sim 4\sigma T_{\rm mid}^4/(\kappa r)$. This is to be compared to F_z, which is $\sigma T_{\rm eff}^4$. These two are related by $T_{\rm mid}^4 \sim (3\tau/8) T_{\rm eff}^4$ (e.g. Hubeny 1990). Therefore

$$F_r \sim \frac{4\sigma T_{\rm eff}^4 (3\tau/8)}{\kappa r} \sim \frac{3}{2} \frac{\kappa(z=H)}{\kappa(z=0)} \frac{H}{r} F_z,$$

where the different opacities at the midplane and at height H are considered. Neglect of radial fluxes is justified if

$$\frac{\kappa(z=0)}{\kappa(z=H)} \gg \frac{3}{2} \left(\frac{H}{r}\right)^2. \tag{2.4}$$

Because in general $H/r \ll 1$ (e.g. $H/r \sim 0.05$ at 1 AU), this condition is usually satisfied. In particular, it is satisfied when the opacities are uniform throughout the disk.

The Rosseland mean opacities at $z = 0$ and at $z = H$ are expected to have similar values, differing only due to the temperature difference between the two layers of the disk. Analytic Rosseland mean opacities can be found in Bell et al. (1997). The general form is $\kappa_R = \kappa_n \rho^{\alpha_n} T^{\beta_n}$, where κ_n, α_n, and β_n are chosen from a table based on the temperature of the gas. In PPDs, the temperatures will be such that β is almost always positive, except in the case of dust evaporation. In the outer regions of the disk it is appropriate to consider $T_{\rm eff}$ and $T_{\rm mid}$ to be in the range where $\kappa_R \propto T^{2.1}$ ($T < 132\,{\rm K}$), simplifying the ratio of the opacities to

$$\frac{\kappa(z=0)}{\kappa(z=H)} = \left[\frac{3\tau}{8}\right]^{0.5025} \tag{2.5}$$

which will be $\gg 3/2(H/r)^2$ for even the smallest values of τ. In the extreme case of dust evaporating at the midplane ($T = 1300\,{\rm K}$) this ratio requirement of opacities will usually be satisfied. Based on this analysis, it is safe to neglect radial fluxes between annuli and to apply the 1.5D approximation.

2.3 Algorithm for calculating disk temperatures

Here we present a new algorithm for the calculation of disk temperatures. It is motivated by the Rybicki method of calculating the transfer of radiation through stellar atmospheres (Mihalas 1978). Our code includes a localized accretional heating term that does not necessarily impose a uniform α throughout the disk, thereby simulating layered accretion. We solve for the disk temperatures on a 2-D grid, within annuli positioned logarithmically at various radii, on a grid of vertical heights above the midplane that is different for each annulus. Axisymmetry is assumed. Our disk has inner and outer edges at $r = 0.1\,\mathrm{AU}$ and $r = 100\,\mathrm{AU}$ respectively. Our number of vertical grid points varies between annuli; generally our grid ranges from the midplane to $z/r \approx 0.2 - 0.3$. We solve for gas density, pressure and temperature (ρ, P, T) within each zone using finite-differenced versions of the equations for radiative transfer, radiative equilibrium and hydrostatic equilibrium, as described below.

First we consider the density distribution. Within each annulus, the total column density, Σ, is assumed fixed. For a particular iteration, the vertical temperature structure, $T(z)$, is also assumed fixed. As in Dullemond et al. (2002), we arbitrarily set $\rho(0) = 1$ on the midplane and assume the equation of state is the ideal gas law, $P = \rho kT/\bar{m}$ (with $\bar{m} = 2m_{\mathrm{p}}$), to relate ρ to P. We then integrate the equation of hydrostatic equilibrium (neglecting the disk's self-gravity):

$$\frac{dP}{dz} = -\frac{GM_\star}{r^3}\rho z. \tag{2.6}$$

The equation is integrated upward from $z = 0$, giving P and therefore ρ ($T(z)$ is known) in the next zone. After finding $\rho(z)$ in all vertical zones, the density is normalized so that the total column density equals Σ.

The vertical density structure can then be used to determine the optical depths into the disk. Defining $\tau_\lambda(r,z) = 0$ at the top of the disk, the optical depth along the vertical direction is

$$\tau_\lambda(r,z) = \int_z^\infty \rho(r,z)\,\kappa_\lambda\,dz, \tag{2.7}$$

where κ_λ is the wavelength dependent opacity of the disk. Our opacity grid will be explained below.

The optical depth into the disk determines where starlight is absorbed in the disk. Within a given annulus, it is assumed that the starlight travels along a single direction at an angle θ to the vertical (in this sense the star is considered a point source rather than an extended object). The line-of-sight optical depth traversed by starlight is the vertical optical depth divided by a geometric factor, $\beta = \cos\theta$, defined below. The local flux of starlight at a (vertical) optical depth τ into the disk is therefore

$$F_\lambda(r,z) = \frac{L_\lambda}{4\pi r^2}\,\exp\left(-\tau_\lambda(r,z)/\beta\right). \tag{2.8}$$

The β factor is calculated for each iteration, based on the latest estimate of the location of the disk's absorption layer, $Z(r)$. For a given annulus, Z is defined as the height above which $\approx$63% (i.e., $1 - \mathrm{e}^{-1}$) of the incident starlight is absorbed. Knowing this height in each annulus, we determine the flaring index,

$$\eta = \frac{d\ln(Z/r)}{d\ln(r)}, \tag{2.9}$$

and then the grazing angle:

$$\beta(r) = 0.4\frac{R_\star}{r} + \frac{Z}{r}\eta. \tag{2.10}$$

The first term on the right hand side accounts for the fact that at small r the finite size of the star matters; even though we assume the radiation is unidirectional, it originates from a direction slightly above the disk when r is

small. Finally, the heating per unit volume due to the protostar's irradiance is found by integrating the local absorption of stellar flux over all wavelengths:

$$q_{\rm irr}(r,z) = \int_0^\infty \rho(r,z)\,\kappa_\lambda\,F_\lambda(r,z)\,d\lambda. \tag{2.11}$$

This quantity is found at all locations, and allows the heating by starlight to be considered separately from the calculation of the radiation field within the disk.

The heating rate from viscous accretion can be calculated from

$$q_{\rm acc}(r,z) = \frac{9}{4}\,\rho\,\nu\,\Omega^2, \tag{2.12}$$

where ν is the viscosity of the disk. We use two different methods to constrain ν. In the first, we fix $\dot{M}$ through the disk and assume $\dot{M} = 3\pi(2\Sigma_{\rm a})\nu$ to solve for ν, where $\Sigma_{\rm a}$ is the column density of each of the two active layers. In the second method, we assume a local value of α and set $\nu = \alpha(kT_{\rm mid}/\bar{m})/\Omega$. We set $\alpha = 0$ in dead zones and allow $10^{-4} < \alpha < 1$ in the active layers. These methods are described more fully in Chapter 3. The sum of these two heating rates, $q = q_{\rm irr} + q_{\rm acc}$, yields the total heating rate per volume at all locations in the disk.

Once the total heating rate q is found everywhere, the temperature structure is updated using the equations of radiative transfer and radiative equilibrium. In practice, the temperature structure is solved for iteratively using an appropriate initial condition (e.g., uniform T or $T(z)$ obtained from a previous simulation with a similar set of disk parameters). On each iteration we solve for ΔT at all heights (in each annulus), update the density (as described above), and repeat until convergence to 0.01% in T is achieved (as many as 10 iterations per annulus may be required on the first pass through the disk, depending on the initial "guess"; usually < 4 iterations per

annulus are required for subsequent passes). Once the densities and temperatures in all annuli have converged, we update the flaring index η and grazing angle β. Updating of η is carried out in pairs, as described in the appendix of Chiang et al. (2001).

Our algorithm differs from previous work primarily in how we calculate the temperature structure. As stated above, each annulus' vertical structure is calculated separately, and each is assumed to be a plane-parallel slab. We do not use frequency-integrated moments of the radiation field, instead utilizing the equations of radiative transfer to solve for the specific intensity and higher moments on a grid of wavelengths. For calculations of the continuum radiation emitted by dust grains, a coarse grid of $\approx$60 wavelengths is sufficient. As is standard, we define the moments of the radiation field as integrals over the angle θ, or $\mu = \cos\theta$, as follows:

$$\begin{aligned} J_\lambda &= \frac{1}{2}\int_{-1}^{1} I_\lambda(\mu)\, d\mu \\ H_\lambda &= \frac{1}{2}\int_{-1}^{1} I_\lambda(\mu)\, \mu\, d\mu \\ K_\lambda &= \frac{1}{2}\int_{-1}^{1} I_\lambda(\mu)\, \mu^2\, d\mu \end{aligned} \tag{2.13}$$

Here J_λ is the mean intensity, H_λ the Eddington flux, and K_λ is proportional to the radiation pressure. We define μ such that $H_\lambda > 0$ if radiation is streaming up (i.e. to larger z, away from the midplane). Of course, by symmetry, $H_\lambda = 0$ on the midplane. Integrating the radiative transfer equations over μ yields the following set of equations:

$$\frac{\partial H_\lambda}{\partial z} = -\rho\kappa_\lambda\, [J_\lambda - B_\lambda(T)] \tag{2.14}$$

$$\frac{\partial K_\lambda}{\partial z} = -\rho\kappa_\lambda\, H_\lambda, \tag{2.15}$$

where $B_\lambda(T)$ is the Planck function at the local temperature.

A third equation is needed to close the moment equations, and we employ the standard technique of Eddington factors, in which $K_\lambda \equiv f_\lambda J_\lambda$, and $H_\lambda(\tau=0) = h_\lambda J_\lambda(\tau=0)$ on the boundary. Our code retains the ability to solve for the Eddington factors with each iteration, using ray-tracing techniques. Within each annulus we create a plane-parallel slab and solve for the specific intensity along rays over a discrete grid of about 8-20 angle cosines, μ. [Actually, we solve for $u = (I(+\mu) + I(-\mu))/2$ at each vertical zone, using Feautrier's method, as described in Mihalas (1978), which involves inversion of a tridiagonal matrix to solve the second-order differential equation with two-point, second-order boundary conditions.] Integration over angle by quadratures yields an estimate of K_λ and J_λ, and therefore f_λ, at all locations. We find, however, as did Dullemond et al. (2002), that the Eddington approximation ($f_\lambda = 1/3$ everywhere, $h_\lambda = 1/2$ on the boundary) works quite well for calculation of the temperature structure, yielding temperatures within $< 10\%$ of those found using the full angular dependence. We therefore adopt the Eddington approximation. This closes the moment equations and yields two differential equations with two unknowns.

This set of coupled first-order differential equations can be converted to a single second-order differential equation. Differentiating Eq. 2.14 and combining it with Eq. 2.15 yields an equation in terms of J_λ:

$$J_\lambda - \frac{\partial^2}{\partial \tau_\lambda^2}\left(f_\lambda J_\lambda\right) = B_\lambda(T), \tag{2.16}$$

which is subject to the boundary conditions $\partial(f_\lambda J_\lambda)/\partial\tau_\lambda = 0$ at the midplane, and $\partial(f_\lambda J_\lambda)/\partial\tau_\lambda = h_\lambda J_\lambda$ at the surface $\tau = 0$. This form of the equations of radiative transfer allows an inversion to find J_λ in terms of $B_\lambda(T)$ at each wavelength, as discussed below. We note that isotropic scattering can be incorporated by this same equation through an altering of the opacities. If χ_λ represents the scattering opacity and κ_λ the absorption

opacity, isotropic scattering can be accommodated by using an effective opacity $\kappa'_\lambda = \kappa_\lambda^{1/2}(\kappa_\lambda + \chi_\lambda)^{1/2}$ (Mihalas 1978).

The radiative transfer equations that solve for J_λ at all wavelengths are also subject to the constraint of radiative equilibrium. When integrated over λ, the the dust's radiative cooling is balanced by the sum of energy absorption from the local radiation field plus the energy generated by the disk. Treating these quantities as rates per volume, we integrate Eq. 2.14 over all wavelengths to yield

$$\frac{\partial H}{\partial z} = -\rho \int_0^\infty \kappa_\lambda \, [J_\lambda - B_\lambda(T)] \, d\lambda, \tag{2.17}$$

where $H = \int_0^\infty H_\lambda \, d\lambda$. Under the condition of radiative equilibrium, the change in radiative flux ($= 4\pi$ times the Eddington flux) across a zone equals the rate at which energy is generated within the zone (by accretional heating of absorption of starlight), so that $\partial H/\partial z = q/4\pi$, or

$$Q + \int_0^\infty \kappa_\lambda \, [J_\lambda - B_\lambda(T)] \, d\lambda = 0, \tag{2.18}$$

where we have introduced heating rate per mass $Q = q/(4\pi\rho)$, not to be confused with heating rate per integrated column as used in an earlier discussion.

The two unknowns in Eq. 2.18, $J_\lambda(\tau_\lambda)$ and $B_\lambda(T)$, are solved for iteratively using a reasonable starting guess for each and finding the corrections δJ_λ and δB_λ. That is, we replace J_λ and B_λ with

$$J_\lambda \to J_\lambda + \delta J_\lambda$$

$$B_\lambda \to B_\lambda + \delta B_\lambda$$

Substituting these expressions into Eq. 2.18 yields

$$\int_0^\infty \kappa_\lambda \, (\delta J_\lambda - \delta B_\lambda) \, d\lambda = -Q - \int_0^\infty \kappa_\lambda \, (J_\lambda - B_\lambda) \, d\lambda. \tag{2.19}$$

Provided δJ_λ can be written in terms of δB_λ, the left-hand side of Eq. 2.19 depends only on δB_λ, and therefore only the local values of the temperatures, i.e., δT at all locations. After each iteration, T is updated, $B_\lambda(T)$ found, J_λ solved for, and the temperatures updated again, iteratively. The left-hand side starts off non-zero for initial guesses of Q, J_λ and B_λ that do not satisfy all the constraints, but approaches zero as these quantities (which are always solutions of the equations of radiative transfer) also converge to conform to radiative equilibrium as well. This iterative relaxation technique thus resembles a Newton-Raphson method.

The key to this approach is finding J_λ everywhere given the source function $B_\lambda(T)$ at all locations (for many different wavelengths), i.e., inverting Eq. 2.16 to solve for J_λ. This is accomplished on a grid by finite differencing. We define the array of all J_λ at a given wavelength (indexed by $l = 1...N$), at all locations indexed by $i = 1...D$, as $\vec{J}_l$. Likewise, the array of temperatures at all locations is $\Delta\vec{T}$, and the array of blackbody radiation mean intensities at all locations, at wavelength l, is $\vec{B}_l$. Finite-differencing the derivative in Eq. 2.16 yields

$$J_{l,i} - \left[\frac{f_{l,i-1}}{\Delta\tau_{l,i}\,\Delta\tau_{l,i-1/2}}\, J_{l,i-1} - \frac{f_{l,i}}{\Delta\tau_{l,i}} \left(\frac{1}{\Delta\tau_{l,i-1/2}} + \frac{1}{\Delta\tau_{l,i+1/2}} \right) J_{l,i} + \frac{f_{l,i+1}}{\Delta\tau_{l,i}\,\Delta\tau_{l,i+1/2}} J_{l,i+1} \right] = B_{l,i}, \tag{2.20}$$

where we have defined

$$\begin{aligned} \Delta\tau_{l,i+1/2} &= \frac{1}{2} \left(\kappa_l \rho_{i+1} + \kappa_l \rho_i \right) |z_{i+1} - z_i| \\ \Delta\tau_{l,i-1/2} &= \frac{1}{2} \left(\kappa_l \rho_{i-1} + \kappa_l \rho_i \right) |z_{i-1} - z_i| \\ \Delta\tau_{l,i} &= \frac{1}{2} \left(\Delta\tau_{l,i-1/2} + \Delta\tau_{l,i+1/2} \right), \end{aligned}$$

as in Mihalas (1978). At each of the boundaries, a Taylor expansion in $f_\lambda J_\lambda$ is used to ensure the boundary conditions are second-order. Casting the

equations in vector form, we obtain

$$\vec{J_l} - \overline{\mathbb{T}}_l \vec{J_l} = \vec{B_l}, \tag{2.21}$$

where $\mathbb{T}_l$ is a $(D \times D)$ tridiagonal matrix. Solving for the radiation field simultaneously at all locations amounts to inverting the matrix equation, to find

$$\vec{J_l} = \left(\overline{\mathbb{I}} - \overline{\mathbb{T}}_l\right)^{-1} \vec{B_l}, \tag{2.22}$$

where $\overline{\mathbb{I}}$ is the identity matrix. The inverted matrix $(\overline{\mathbb{I}} - \overline{\mathbb{T}})^{-1}$ thus plays the role of the Lambda operator. In terms of this,

$$\delta\vec{J}_l = \left(\overline{\mathbb{I}} - \overline{\mathbb{T}}_l\right)^{-1} \delta\vec{B}_l. \tag{2.23}$$

(It is assumed that opacities are insensitive to temperature, appropriate for the solid-state opacity of dust in a protoplanetary disk.) Finally, substituting this into the equation of radiative equilibrium, and using the identity $\delta B_\lambda = (\partial B_\lambda / \partial T)\, \delta T$, we find

$$\left\{ \sum_{l=1}^{N} \kappa_l \, w_l \, \left[\left(\overline{\mathbb{I}} - \overline{\mathbb{T}}_l\right)^{-1} - \overline{\mathbb{I}} \right] \left(\frac{\partial \vec{B}_l}{\partial T} \right) \right\} \Delta\vec{T} = \vec{Q} - \sum_{l=1}^{N} \kappa_l \, w_l \, \left(\vec{J_l} - \vec{B_l} \right), \tag{2.24}$$

where the values of $\partial B_\lambda / \partial T$ at all depths have been arranged into N arrays of length D, one for each wavelength, and the w_l are the weights needed to integrate over wavelength by quadrature. Inversion of this matrix equation enables ΔT to be found at all depths *simultaneously*, accounting for the absorption of radiation emitted at distant points, and all subject to the constraint of radiative equilibrium. It is the difficult inversion of this non-sparse matrix that changes this calculation from a simple Lambda iteration.

The sequence of calculations is as follows. For a given temperature structure in a given annulus, we recalculate the density structure using the equations of hydrostatic equilibrium, and also update the temperature

structure inverting Eq. 2.24. This step is repeated until the annulus' temperature structure has converged (usually no more than 4-5 times). After all annuli have updated temperatures, the flaring index is recalculated based on the new temperature structure, and the heating by absorption of starlight recomputed. We iterate on the flaring index about 4 times, so that ≈ 20 calculations of the temperature structure in each annulus are made in total. We typically use 85-180 vertical zones in each annulus and 50 radial zones, and a grid of 60 wavelengths. On our 2 GHz processor, convergence (defined to be when temperatures change by $< 1\%$ from one iteration to the next) may take hours with a bad starting guess, but is reduced to less than an hour of computing time with a reasonable starting solution, due to the quadratic nature of the convergence. For active disks, we must further limit the temperature increase between iterations, to avoid instabilities. For very active disks, the calculation may therefore take tens of hours to converge. These computing times are long but not prohibitive, and they do allow the full wavelength dependence of the radiation field to be retained at all steps in the calculation.

2.4 Dust Opacity

Most models of PPDs assume a dust population of silicates and consider them the dominant source of opacity in the disk. We will do likewise, since our focus here is on presenting the algorithm for calculating the radiation field. For the opacities $\kappa(\lambda)$, we have assumed a monodispersion of spherical dust grains with radii $0.1\,\mu$m, with optical constants for "astronomical silicate" grains from Draine & Lee (1984). Figure 2.2 presents our opacity grid. A uniform (well-mixed) dust-to-gas mass ratio of 1% was assumed. Real dust in protoplanetary disks will exhibit a large range of sizes and compositions, and may even settle (sediment) relative to the gas, but such

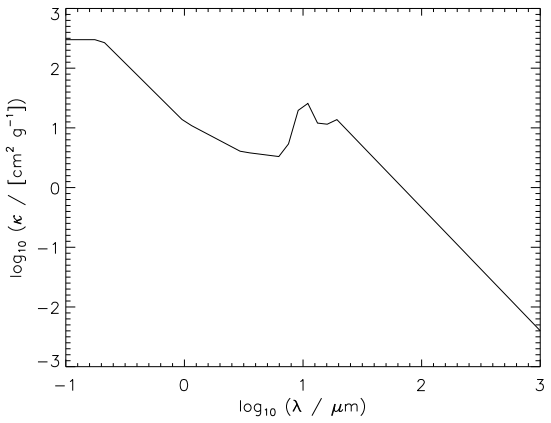

Figure 2.2: The opacity used in all of the models presented in this paper, corresponding to a single population of spherical silicate grains with $a = 0.1\,\mu$m, and a dust-to-gas mass ratio of 1%, taken from Draine & Lee (1984).

complications lie beyond the scope of the present paper. However, while Fig. 2.2 represents the opacities nominally used, there are two departures that we sometimes make, as we now discuss.

When considering disks where accretional heating is present, it is expected that temperatures may exceed the evaporation temperature, $T_{\rm evap}$, of silicate dust in locations close to the central protostar (see D'Alessio et al. 1998). Exact temperatures vary, but $T_{\rm evap} \approx 1350\,$K is appropriate for forsterite (Lodders 2003); we shall adopt this temperature in our model. Therefore the effects of dust evaporation have to somehow be accounted for, especially since failure to do so has a strong (and aphysical) positive feedback on irradiation and disk temperatures. To prevent this we reduce the opacities of dust by a factor of 100 below the values predicted by Draine & Lee (1984) in regions of the disk that exceed the evaporation temperature (see Lenzuni et al. 1995).

The second modification accounts for the effects of convection. As was discussed in §1, it is expected that convection will play a minor (if any) role in providing the turbulence responsible for transporting angular momentum. Nevertheless, accretional heating can lead to a temperature gradient that can initiate convection. We expect that energy will be transferred via radiation

in nearly all disk locations; however, there may be areas where the temperature gradient is too large for convective stability. To account for this, we define the adiabatic temperature gradient,
$(dT/dz)_{\rm ad} = ((\gamma - 1)/\gamma)\,(\bar{m}\,\Omega^2\,z/k)$, where $\gamma = 7/5$ is the ratio of specific heats, $\bar{m}$ the mean molecular weight, k Boltzmann's constant, and z the height above the midplane. If the actual temperature gradient exceeds the adiabatic temperature gradient in a zone by a factor $|dT/dz|/|dT/dz|_{\rm ad}$, then the opacity (at each wavelength) is reduced in that zone by that factor. In practice, this opacity change is only required near the midplane for fully active disks and for a small number of areas in disks with layered accretion.

2.5 Comparison to Previous Results

To check the accuracy of the code, we conducted a benchmark run adopting the same protostar parameters as those of Dullemond et al. (2002) ($M_\star = 0.5\,{\rm M}_\odot$, $R_\star = 2.0\,{\rm R}_\odot$, $T_\star = 3000\,{\rm K}$, $L = 0.92{\rm L}_\odot$), as well as their disk parameters ($\Sigma_{\rm disk} = 1000\,{\rm g\,cm^{-2}}\,(R/1\,{\rm AU})^{-1}$, $\mu = 2.3$, gas-to-dust mass ratio $100:1$). The case they tested was of a passive disk, so our code was run with $\alpha = 0$ for comparison. While our code finds the same general trends, the midplane temperatures tend to be slightly higher in our models. We find that at 1 AU our superheated layer temperatures are in fair agreement: the temperature of 210.2 K found by Dullemond et al. (2002) is only 1.6% different than our value of 213.7 K, indicating that our dust opacities match very closely. On the other hand, the temperature of 61.3 K at the midplane at 1 AU reported by Dullemond et al. (2002) is 13.3% cooler than our value of 70.8 K. We do not attribute this discrepancy to differences in dust opacities. Instead, we attribute the discrepancy to the way the vertical temperature structure was found in each annulus. Specifically, we suggest that including the full wavelength dependence of the radiation field (as

opposed to using κ_J and frequency-integrated opacities and radiation field) may be the determining factor. Dullemond & Dominik (2004) note that calculating the full wavelength-dependent radiation field, using the Monte Carlo algorithm of Bjorkman & Wood (2001), led to temperature differences of 5-10% from those of Dullemond et al. (2002). Whether or not this is the cause of the discrepancy, we consider our code to be at least as valid as that of Dullemond et al. (2002).

Chapter 3

PPD TEMPERATURE RESULTS

3.1 Model Parameters

We have generated a number of models with different input parameters. For the protostar, we used commonly assumed T Tauri star parameters ($M = 0.5\,\mathrm{M}_\odot$, $R = 2\,\mathrm{R}_\odot$, and $T = 4000\,\mathrm{K}$). This protostar could be an analog of the Sun at an early stage, when it was still accreting heavily from the PPD. For the disk itself, we assumed a power-law surface density, $\Sigma(r) = 10^3\,(r/1\,\mathrm{AU})^{-3/2}\,\mathrm{g\,cm^{-2}}$, which mimics the minimum mass solar nebula (Hayashi 1981), but which has a total mass $\approx 0.014\,M_\odot$ inside 100 AU. We assumed the disk gas is uniformly mixed with dust, with a dust-to-gas mass ratio 0.01. Unless otherwise specified, these protostar and disk parameters will be used for all models presented in this paper.

We divided our disk into 50 logarithmically spaced annuli between the inner edge (0.1 AU) and outer edge (100 AU). At each annulus we imposed a vertical grid with between 85 and 180 linearly spaced zones (with the exact number depending on how flared the disk has become at that radius). The algorithm iterates until both temperature and flaring index converge to within our criteria. If a convergence criteria of 5% is imposed on both temperature and flaring index, the resulting temperature structure typically converges to within 1%, due to the nesting of the temperature iterations within the flaring index iteration.

3.2 Passive Disk

We apply our code first to the case of a passively heated disk with the parameters above, in which viscous heating is neglected. This case

corresponds to that analytically solved for by Chiang & Goldreich (1997) using their two-layer approach, and is similar to the case studied by Dullemond et al. (2002) using different protostar and disk parameters. Figure 3.1 displays the vertical structure of the passive disk for 3 distances from the central protostar: 0.3 AU, 1 AU, and 3 AU. The temperature panes show the familiar two-tiered profiles, with temperatures near the disk's surface much warmer than those near the midplane in the same annulus. This is due to the bulk of the protostar's radiation being absorbed in the layers directly below the superheated layer, as indicated by the peak in the plots of energy absorbed per unit volume q, which matches the height where the temperature drops off at each annulus. For the annulus at 1 AU, we found a midplane temperature of 117 K and superheated layer dust temperature of 355 K. The maximum heat absorption rate was found at $Z = 0.16\,\mathrm{AU}$, about 3.7 times the density scale height at 1 AU ($H = 0.043\,\mathrm{AU}$). This is consistent with the findings of Chiang & Goldreich (1997) in which Z/H is expected to be between 3 and 4.5. These results provide justification for the assumption of Chiang & Goldreich (1997), that two roughly isothermal layers exist at each radius in a passive disk.

Figure 3.2 shows the midplane temperatures, surface layer temperatures, and superheated layer height as a function of radius. For the passive disk the superheated layer is warmer than the midplane at each annulus. The superheated layer height Z monotonically increases with radius and this relationship approximates a power law, with $Z/r \approx 0.162\,(r/1\,\mathrm{AU})^{+0.204}$. This is similar to, but implies less disk flaring than, the power law predicted by Chiang & Goldreich (1997), $Z/r \propto r^{0.29}$. We attribute the difference to the more complicated opacity law we used.

Our surface density profile was chosen arbitrarily, but the

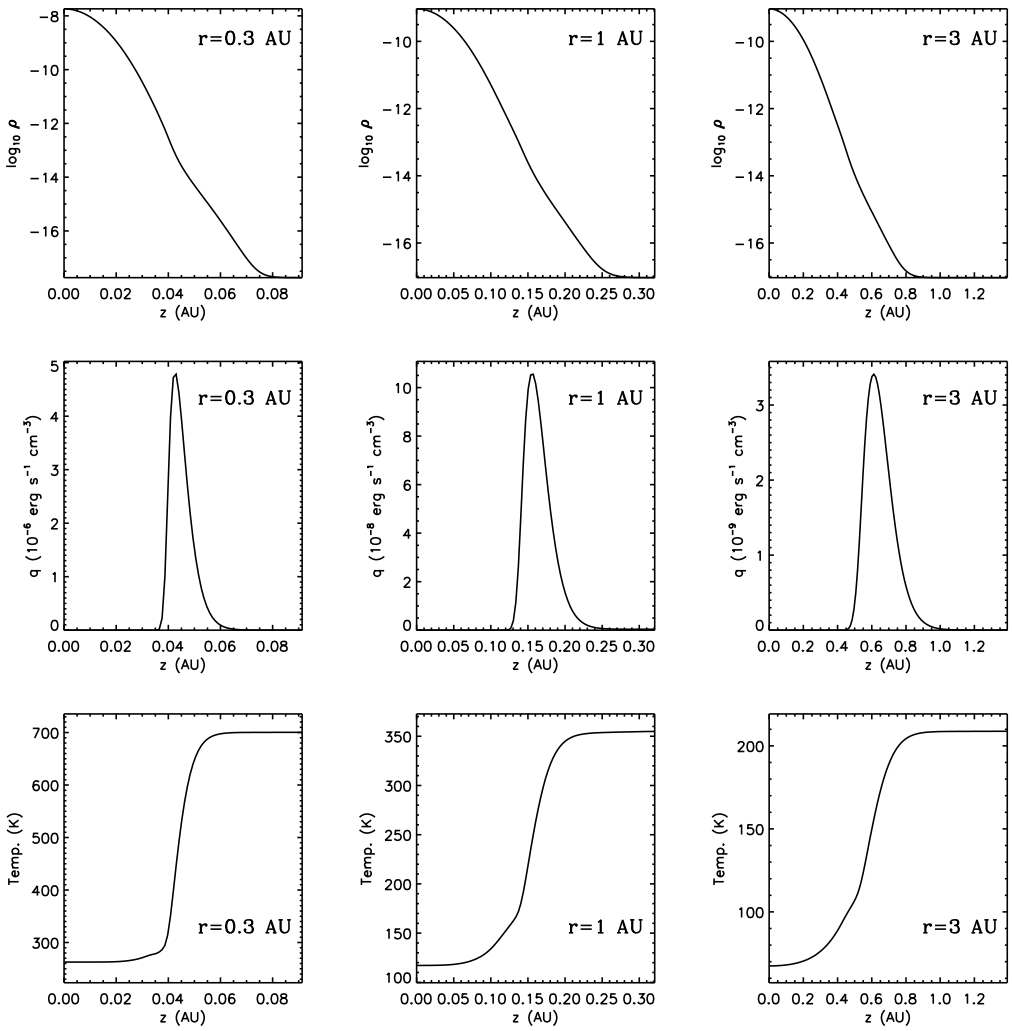

Figure 3.1: Vertical structure of the mass density (top row), heating rate per volume (middle row), and temperature (bottom row) at 3 radii from central protostar: 0.3 AU (left column), 1 AU (middle column), and 3 AU (right column), for the case of the passive disk.

temperature structure of the disk is insensitive to the magnitude of $\Sigma(r)$. We tested passive disks following the same power law ($\Sigma \sim (r/\mathrm{AU})^{-3/2}$) but with different values at 1 AU. With a disk 10 times as massive, that is $\Sigma(r = 1\,\mathrm{AU}) = 10^4\,\mathrm{g\,cm^{-2}}$, $T_{\mathrm{mid}}(r)$ changed by less than 6%. This is understandable since for a passive disk the temperature of the midplane is driven by the amount of energy the disk's annulus intercepts, which in turn depends on the height of the superheated later, Z. We calculate Z by finding

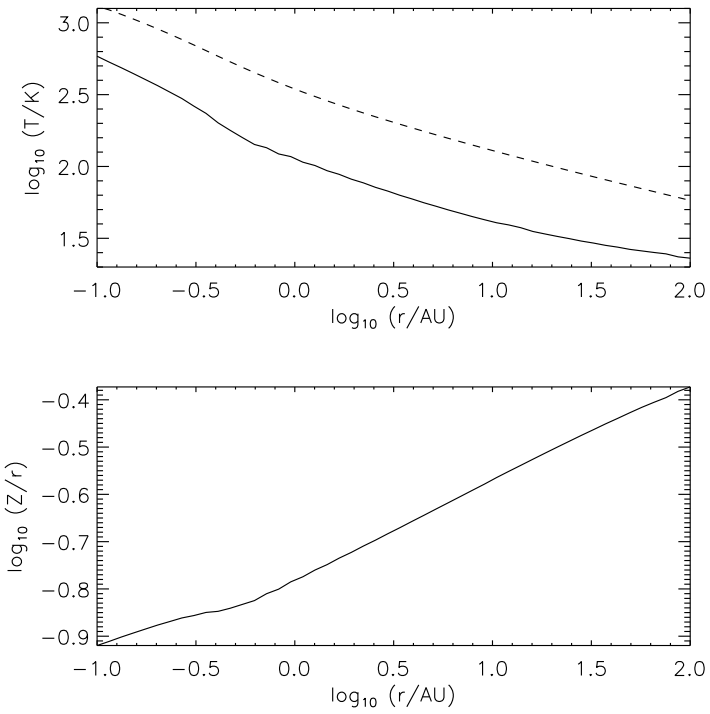

Figure 3.2: Top frame: Midplane temperatures (solid line) and superheated dust layer temperatures (dashed line) at all radii, for the passive disk. Bottom frame: Height of the superheated dust layer as a function of radius for the disk.

where the optical depth, τ, as measured along the line of sight to the protostar, is unity ($\tau = \Sigma_{\rm Z}\kappa/\beta = 1$, where $\Sigma_{\rm Z}$ is the column density above Z, κ the opacity, and β is the starlight's angle of incidence). Since $\Sigma_{\rm Z} \ll \Sigma$, we can use the fact that density follows a Gaussian profile and replace it by $\rho_Z H/(Z/H)$, where ρ_Z is the mass density at the photosphere, Z, and H is the pressure scale height of the annulus. For passive disks $Z/H \approx 4$, yielding $\rho_Z = 4\beta/(H\kappa)$. Assuming the annulus is isothermal (which is true for most of the mass, located below the superheated layer),
$\rho = \Sigma(2\pi H^2)^{-1/2}\exp(-z^2/2H^2)$. Setting $\rho = \rho_Z$ yields
$Z = [2H^2 \ln(\tau_{\rm mid}(2\pi\beta^2)^{-1/2})]^{1/2}$, where $\tau_{\rm mid} = \kappa\Sigma$ is our proxy for column density of the annulus. The dependence of Z on the square root of the logarithm of $\tau_{\rm min}$ means that the photospheric height is only very weakly

dependent on the surface density of the annulus. This crude treatment predicts that increasing the surface density by a factor of 10 will yield only an 8% increase in Z (for an assumed $\beta = 0.01$), which matches well our computed 6% increase in Z. Because the midplane temperature in a passive disk depends only on the amount of sunlight intercepted and therefore the height of the photosphere, passive disk midplane temperatures will depend only very weakly on total surface density.

Our temperature solution converged to within 1% in all zones, after about 7 hours of runtime (on a 2 GHz processor) and approximately 25 flaring index iterations. Convergence to within 0.01% required a factor of 3 more computational effort, with a runtime of 24 hours and 80 iterations over flaring index. These runtimes are consistent with the expected quadratic convergence. While a large amount of computation time is required to generate a passive disk solution in the absence of an appropriate starting approximation, models that use this case as an initial guess (e.g. layered accretion disks presented below) will reach convergence much quicker; typically an hour or less.

3.3 Active Disk – Uniform Accretion

We next apply our code to the case of an active disk which is uniformly accreting. That is, we assume the viscous heating rate is $q = (9/4)\rho\,\nu\,\Omega^2$, where $\nu = \alpha\, c_{\rm s}^2/\Omega$ is vertically uniform in each annulus ($c_{\rm s}$ being the sound speed as determined by the midplane temperature $T_{\rm mid}$), and where α is assumed uniform throughout the disk. In the example that follows we set $\alpha = 10^{-2}$ everywhere, as in D'Alessio et al. (1998). Convergence times were longer for the active disk model than for the passive disk, due to the greater number of feedbacks between heating and structure. Convergence of

temperatures everywhere to within 1% required 30 hours of computation, and convergence to 0.01% required 69 hours.

Figure 3.3 shows our computed vertical temperature structure of the disk at 1 AU. The temperature structure is slightly more complicated than that of the passive disk. Instead of two isothermal zones with a transition zone between them, the fully active disk has a high midplane temperature (1056 K in this example), dropping with height to a minimum temperature (215 K) at $z = 0.25\,\mathrm{AU}$; the temperature then rises with increasing height within the superheated dust layer (to a local maximum of 361 K). The high midplane temperature and negative temperature gradient throughout most of the disk are due to the accretional heating that peaks near the midplane, and the sign of the implied radiative flux. Above $\approx 0.25\,\mathrm{AU}$, the disk is optically thin to its own emission; however, the temperature is rising due to exposure to the protostellar radiation. This interpretation is confirmed by the vertical variation of the local heating rate, which is depicted in Figure 3.4. There are two peaks in the structure of $q(z)$: a sharper peak that corresponds to heating by protostellar irradiation (reaching a maximum at $z = 0.26\,\mathrm{AU}$, tapering to near-zero at $z = 0.24\,\mathrm{AU}$), and a broader peak centered on the midplane that is due to accretional heating. For comparison, the curves of $T(z)$ and $q(z)$ for the passive disk are overlaid on Figures 3.3 and 3.4. The differences between these curves reflect the fact that the active disk is intrinsically hotter and has a large scale height, so that it is more "puffed up". Its superheated dust layer thus begins only above about 0.3 AU elevation (as opposed to 0.2 AU for the passive disk).

In Figure 3.5 we show the variation of midplane temperature, T_{mid}, and superheated dust layer temperature, T_{s}, with distance from the star, r, for both the passive disk and the uniformly accreting disk. As expected, $T_{\mathrm{s}}(r)$

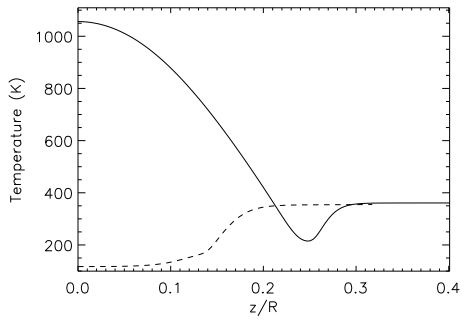

Figure 3.3: Temperature as a function of height above the midplane at $r = 1\,\mathrm{AU}$, in a uniformly accreting disk with $\alpha = 10^{-2}$ (solid line). For comparison the temperature profile of the passive disk is shown as well (dashed line).

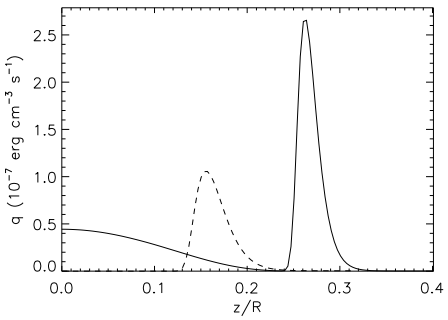

Figure 3.4: Energy absorption rate (q) vs. vertical height at $r = 1\,\mathrm{AU}$ for the uniformly accreting disk (solid line). The passive disk's profile is shown for comparison (dashed).

is the same for both cases, although the superheated dust layer is located at a higher elevation for the active layer case. Beyond about 5 AU, the midplane temperatures are the same for the two cases, reflecting the fact that at large radii, accretional heating becomes negligible compared to the absorption of starlight. In a disk with $\Sigma(r) \propto r^{-p}$ and $T(r) \propto r^{-q}$, the heating rate (per disk area) due to absorption of starlight scales as $r^{-3/2-q/2}$, whereas the accretional heating rate scales as $r^{-3/2-q-p}$, so that the ratio of accretional heating to irradiation scales as $r^{-p-q/2}$. For $p = 3/2$ and $q \approx 1/2$, the ratio of accretional to starlight heating drops off steeply, as $r^{-1.75}$. Only inside about 5 AU does accretional heating affect the midplane temperature, causing it to rise with decreasing r. Figure 3.5 also demonstrates the effects of dust evaporation. Once midplane temperatures are high enough to evaporate dust (1350 K), the midplane region becomes effectively optically thin; the ease of radiation escaping at all wavelengths inhibits the disk from heating up much more. Midplane temperatures inside of 0.8 AU are therefore essentially isothermal and do not rise much above the evaporation temperature of dust.

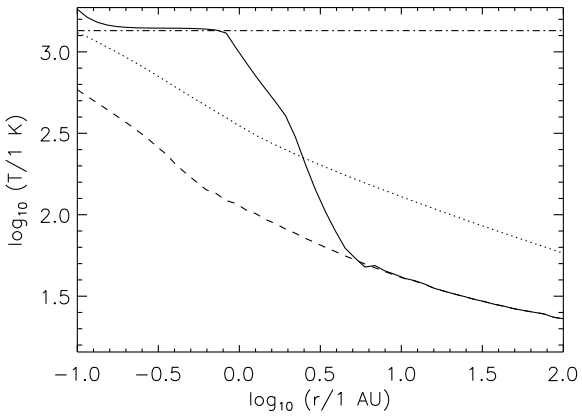

Figure 3.5: Midplane temperature (solid line) and superheated dust layer temperature (dotted line) as a function of radius for the uniformly accreting disk. For comparison, the passive disk's midplane temperature profile is plotted (dashed line). The adopted evaporation temperature of silicate dust ($T = 1350$ K) is shown with a dot-dash line.

Intimately connected with the scale height is the flaring index, $\eta = d\ln(Z/r)/d\ln r$. Figure 3.6 shows the variation in flaring index η as a function of distance from the star, for both the active disk and the passive disk. Especially at radii < 1 AU, the active disk has a much greater flaring index than the passive disk, and Z rises with r much more steeply than in the passive disk. The scale height of the active disk is a factor of 3 larger at 1 AU than in the passive disk. This is mostly due to the extra accretional heating experienced by the disk, but is also due to the greater amount of starlight absorbed due to the greater flaring index. Beyond 1 AU, however, accretional heating diminishes in importance, and the disk temperatures begin to fall off steeply; so steeply that Z increases with r less rapidly than r^1, and the flaring index is driven to negative values. Physically, this refers to the case where the annuli beyond 1 AU (out to 5 AU) are shadowed by areas of the disk interior to 1 AU, which are puffed up because of the additional accretion heating inside 1 AU. Bell et al. (1997) found similar behavior in their accretion disk models. To improve the stability of the code, we arbitrarily set a floor of 0.10 on the flaring index η, which is why $\eta = 0.1$ between 1.3 and 4.5 AU. We found very little change in temperatures with a floor of $\eta = 0.01$. Self-shadowing is irrelevant beyond 10 AU and the active

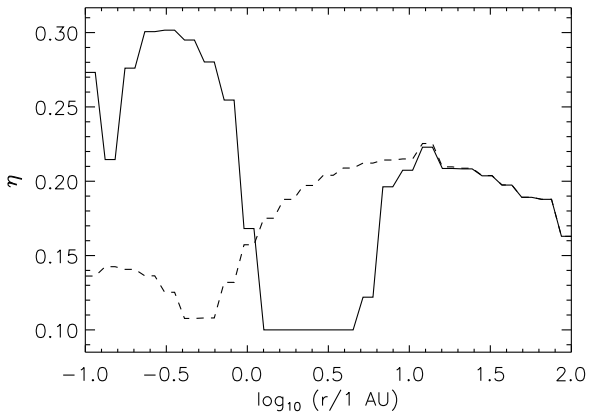

Figure 3.6: Flaring index $\eta = d\ln(Z/r)/d\ln r$ as a function of radius for the passive disk (dashed line) and the uniformly accreting disk (solid line).

and passive disks have the same variations of temperature and flaring index with r, reflecting that those annuli are not affected by accretion, either directly (because accretional heating is negligible there), or indirectly (because those annuli are far enough from the star to not be shadowed by inner gas puffed up by accretion).

In summary, the uniformly active disk tends toward a self-shadowing state with high midplane temperatures at small radii (at least for $\alpha = 10^{-2}$). With both the passive and uniformly accreting cases computed, we now show the results of a parameter study in which the accretion is non-uniform, and either $\Sigma_{\rm a}$ and α are varied at fixed $\dot{M}$, or $\Sigma_{\rm a}$ and $\dot{M}$ are varied at fixed α.

3.4 Active Disks – Fixed $\dot{M}$

Our first set of layered accretion models will consist of those where viscosity is defined in terms of a mass accretion rate, $\dot{M}$, and an active layer thickness, $\Sigma_{\rm a}$, of our choosing. For the purposes of calculating viscosity, α is ignored. This set of models thus resembles that studied by Bell et al. (1997), in which $\dot{M}$ was considered uniform throughout the disk. In the case that $\dot{M}$ is uniform, it is straightforward to show (Armitage 2007) that $\dot{M} = 6\pi\Sigma_{\rm a}\nu$, where ν is the viscosity (assumed vertically uniform) in the active layers.

$\dot{M}$ ($M_\odot\,yr^{-1}$)	Σ_a ($g\,cm^{-2}$) 1.0	3.0	10.0	30.0	100.0
1.0×10^{-9}	117.2	118.1	120.0	123.1	145.0
1.0×10^{-8}	117.5	119.4	140.4	191.7	280.1
1.0×10^{-7}	160.5	206.5	275.8	368.4	471.1
1.0×10^{-6}	301.9	364.4	471.9	610.8	787.2

Table 3.1: Midplane temperatures (in K) at 1 AU for various active layer column densities and mass accretion rates.

Note that we consider the accretion to occur only in two active surface layers, sandwiching a dead zone with $\nu = 0$, as outlined by Gammie (1996); we assume that within the dead zone there is no accretional heating. As in Gammie (1996), we assume a radially uniform Σ_a and we consider 5 different values: $1\,g\,cm^{-2}$, $3\,g\,cm^{-2}$, $10\,g\,cm^{-2}$, $30\,g\,cm^{-2}$, and $100\,g\,cm^{-2}$. In choosing a value of Σ_a we are implicitly defining the column density of the dead zone as well. For annuli where $2\Sigma_a < \Sigma$, the dead zone thickness is $\Sigma_{dz} = \Sigma - 2\Sigma_a$. We consider 3 mass accretion rates typical of T Tauri disks, in the range $10^{-9} - 10^{-7}\,M_\odot\,yr^{-1}$ (Gullbring et al. 1998). Fixing $\dot{M}$ and Σ_a yields $\nu = \dot{M}/(6\pi\Sigma_a)$, which is sufficient to calculate the local heating rate in the disk, although an equivalent α (in the active layer) can be found from the relation $\nu = \alpha c_s^2/\Omega$. Note that this calculation of α is purely for comparison purposes and is not used in the model.

Table 3.1 lists, for the 20 combinations of $\dot{M}$ and Σ_a, the midplane temperatures at 1 AU. Based on these T_{mid} values, the equivalent α in the active layer at 1 AU can be computed, these are presented in Table 3.2. The run of midplane temperature with radius for all 15 cases is shown in Figure 3.7. As expected, the deviations from $T_{mid}(r)$ of the passive disk are greatest for disks with higher mass accretion rates and in areas of the disk closer to the central protostar, consistent with the fact that the accretional heating rate varies as $(3/8\pi)\,\dot{M}\Omega^2 \propto r^{-3}$.

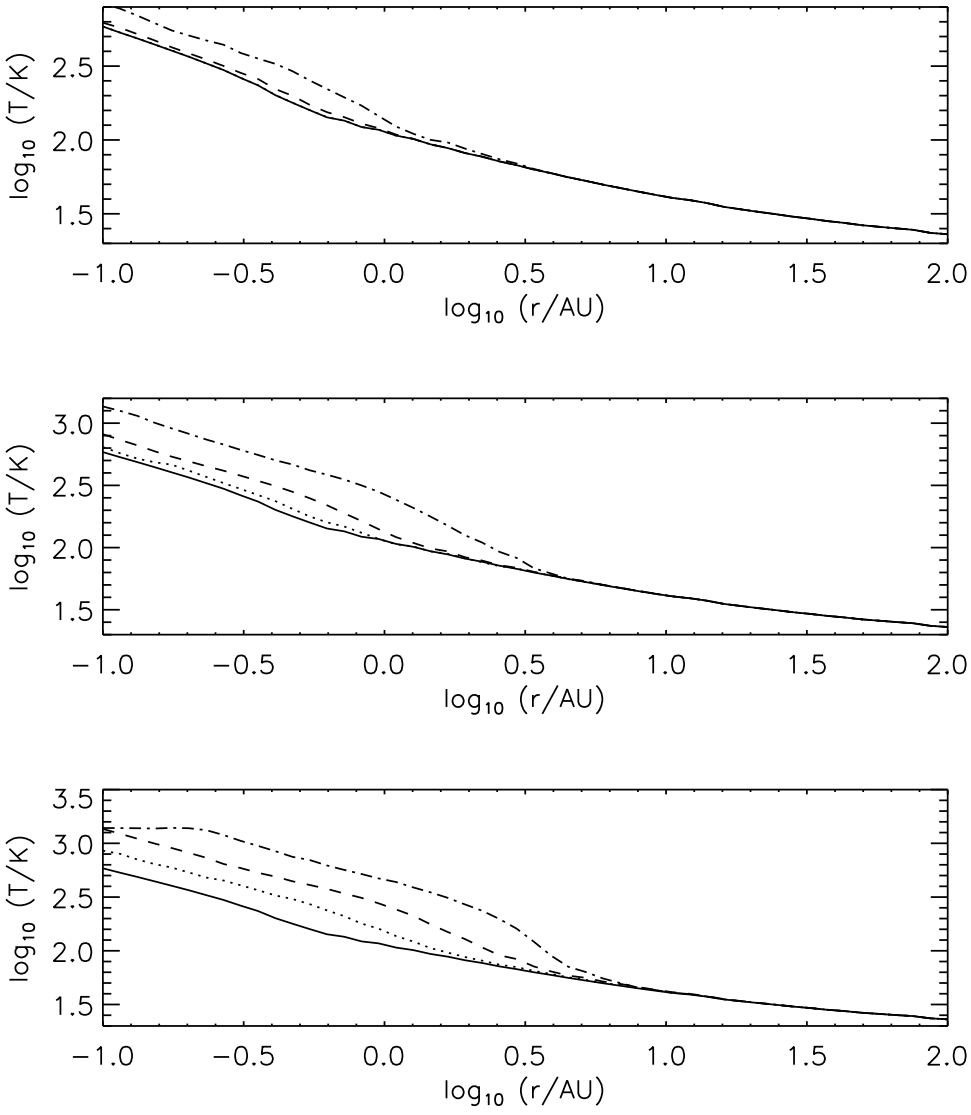

Figure 3.7: Midplane temperatures $T_{\rm mid}(r)$ in actively accreting disks with viscosities calculated from the disk's mass accretion rates. Cases shown are $\dot{M} = 10^{-9}$ $\rm M_\odot\,yr^{-1}$ (top), 10^{-8} $\rm M_\odot\,yr^{-1}$ (middle), and 10^{-7} $\rm M_\odot\,yr^{-1}$ (bottom). For each mass accretion rate, 3 different layer thicknesses are shown: $\Sigma_{\rm a} = 1.0\ \rm g\,cm^{-2}$ (dotted), $10.0\ \rm g\,cm^{-2}$ (dashed), and $100.0\ \rm g\,cm^{-2}$ (dot-dashed) The passive disk is included for comparison as well (solid line).

$\dot{M}$ ($M_\odot$ yr^{-1})	Σ_a (g cm^{-2}) 1.0	3.0	10.0	30.0	100.0
1.0×10^{-9}	0.052	0.017	0.0051	0.0016	0.00042
1.0×10^{-8}	0.52	0.17	0.043	0.011	0.0022
1.0×10^{-7}	3.8	0.98	0.22	0.055	0.013
1.0×10^{-6}	41.1	11.3	2.63	0.677	0.157

Table 3.2: Equivalent values of α in the active layer at 1 AU for the same models presented in Table 3.1.

We introduce a nomenclature for our layered accretion models generated. The simulations following the prescription in this section carry the letter prefix m (for fixed $\dot{M}$) followed by a number corresponding to the logarithm of $\dot{M}$. The second number given is the logarithm of Σ_a. For example, model number m8-1 corresponds to fixed $\dot{M} = 10^{-8}\,M_\odot\,\mathrm{yr}^{-1}$ with an active layer of thickness $\Sigma_a = 10^1\,\mathrm{g\,cm}^{-2}$. Fifteen such models are generated. Five models are with $\dot{M} = 10^{-9}\,M_\odot\,\mathrm{yr}^{-1}$: m9-0, m9-0.5, m9-1, m9-1.5, and m9-2. Five with $\dot{M} = 10^{-8}\,M_\odot\,\mathrm{yr}^{-1}$: m8-0, m8-0.5, m8-1, m8-1.5, and m8-2. The models with $\dot{M} = 10^{-7}$ are m7-0, m7-0.5, m7-1, m7-1.5, and m7-2. The last five have $\dot{M} = 10^{-6}\,M_\odot\,\mathrm{yr}^{-1}$: m6-0, m6-0.5, m6-1, m6-1.5, and m6-2.

The vertical temperature profiles at selected radii (0.3 AU, 1 AU, and 3 AU), for a variety of active layer column densities Σ_a ($1\,\mathrm{g\,cm}^{-2}$, $10\,\mathrm{g\,cm}^{-2}$, and $100\,\mathrm{g\,cm}^{-2}$), are shown in Figures 3.8 ($\dot{M} = 10^{-9}\,M_\odot\,\mathrm{yr}^{-1}$), 3.9 ($\dot{M} = 10^{-8}\,M_\odot\,\mathrm{yr}^{-1}$), and 3.10 ($\dot{M} = 10^{-7}\,M_\odot\,\mathrm{yr}^{-1}$). The passive disk is also plotted for comparison. The 10^{-9} $M_\odot\,\mathrm{yr}^{-1}$ models all show little difference in temperature structure compared to the passive disk, especially at 3 AU and beyond. At $r \leq 1\,\mathrm{AU}$, accretion raises the temperature near the midplane and, paradoxically, lowers it slightly below the superheated dust layer. This is a consequence of differences in the scale height and the elevation of the superheated dust layer, relative to the passive disk case. In all cases the

effect of increasing Σ_a is to increase the midplane temperature, thereby increasing the disk scale height and the height of the superheated dust layer. These differences are more pronounced in disks with higher $\dot{M}$.

3.5 Active Disks – Fixed α

We also investigate the effects of layered accretion by fixing α in the active layer, rather than $\dot{M}$. This means we define viscosity in the active layer as $\nu = \alpha\, c_s^2/\Omega$, where c_s is the sound speed at the disk midplane. Unlike the cases discussed in the previous section, here ν is independent of $\dot{M}$. We consider 4 values of α (10^{-4}, 10^{-3}, 10^{-2} and 10^{-1}) and the same 5 values of Σ_a as above in the range $1 - 100\,\mathrm{g\,cm^{-2}}$. As with the models in §3.4 by choosing a value of Σ_a we are implicitly defining the dead zone column density to be the remainder of the column. Table 3.3 lists the midplane temperatures for these 20 models. Table 3.4 presents the equivalent $\dot{M}$ (at 1 AU) for these 20 models. As in the previous section, an equivalent $\dot{M}$ is computed only for comparison purposes and is not used to calculate temperatures.

There are 20 combinations of layered accretion parameters to be tested here. We name these models in a similar fashion to those in §3.4. These simulations have the letter prefix *a* (for fixed α). The number following it would be the logarithm of α. Similar to the fixed $\dot{M}$ models described

	$\Sigma_a\,(\mathrm{g\,cm^{-2}})$				
α	1.0	3.0	10.0	30.0	100.0
10^{-3}	117.2	117.2	117.3	117.7	143.2
10^{-2}	117.2	117.2	117.8	140.0	376.2
10^{-1}	117.2	117.8	149.6	362.0	713.1

Table 3.3: Midplane temperatures (in K) at 1 AU for various active layer column densities and values of α in the active layer.

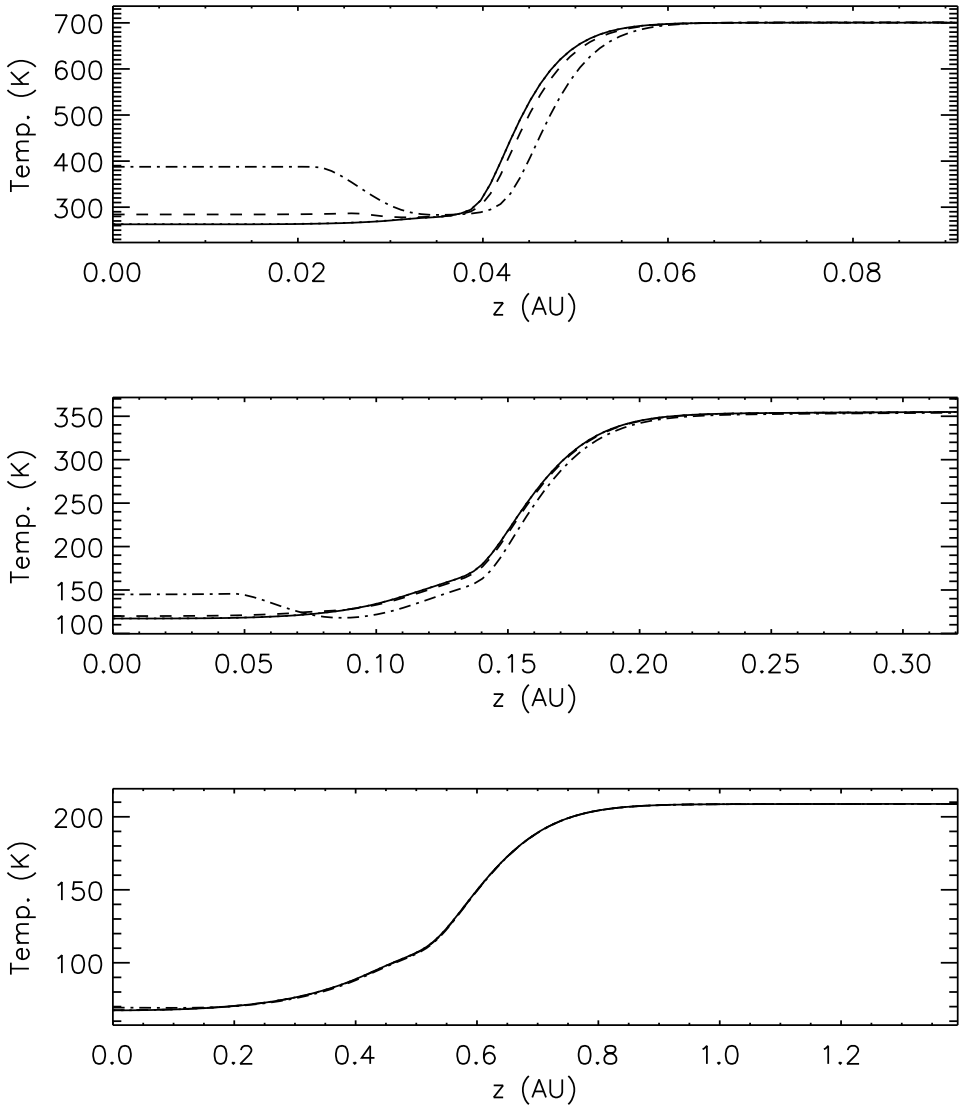

Figure 3.8: Vertical temperature structure of active disk with $\dot{M} = 10^{-9}\,\mathrm{M}_{\odot}\,\mathrm{yr}^{-1}$. Plotted are profiles at radii of 0.3 AU (top), 1 AU (middle), and 3 AU (bottom). The various active layer thicknesses are plotted in the same fashion as Figure 3.7: [$\Sigma_a = 1.0\ \mathrm{g\,cm^{-2}}$ (dotted), $10.0\ \mathrm{g\,cm^{-2}}$ (dashed), and $100.0\ \mathrm{g\,cm^{-2}}$ (dot-dashed)].

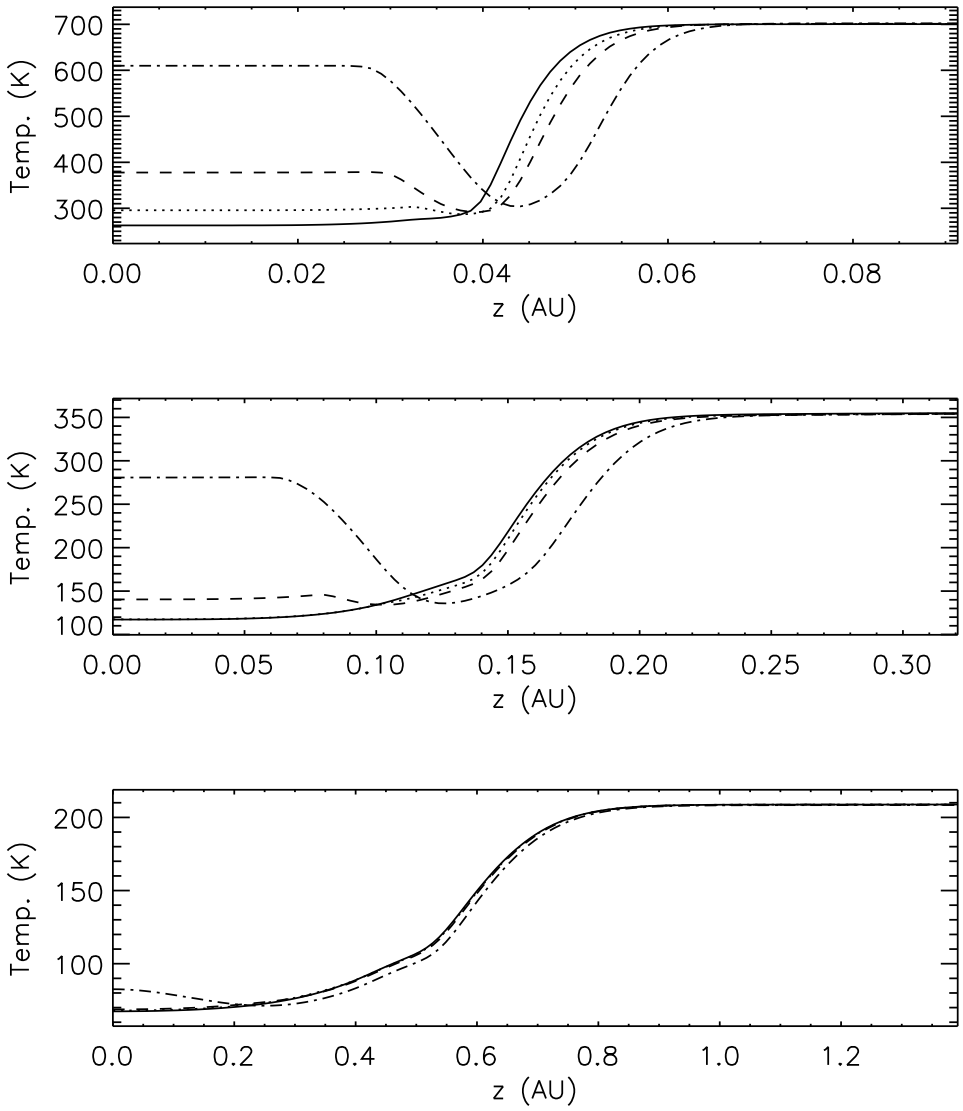

Figure 3.9: Same as Figure 3.8, but with $\dot{M} = 10^{-8}\,\mathrm{M}_{\odot}\,\mathrm{yr}^{-1}$.

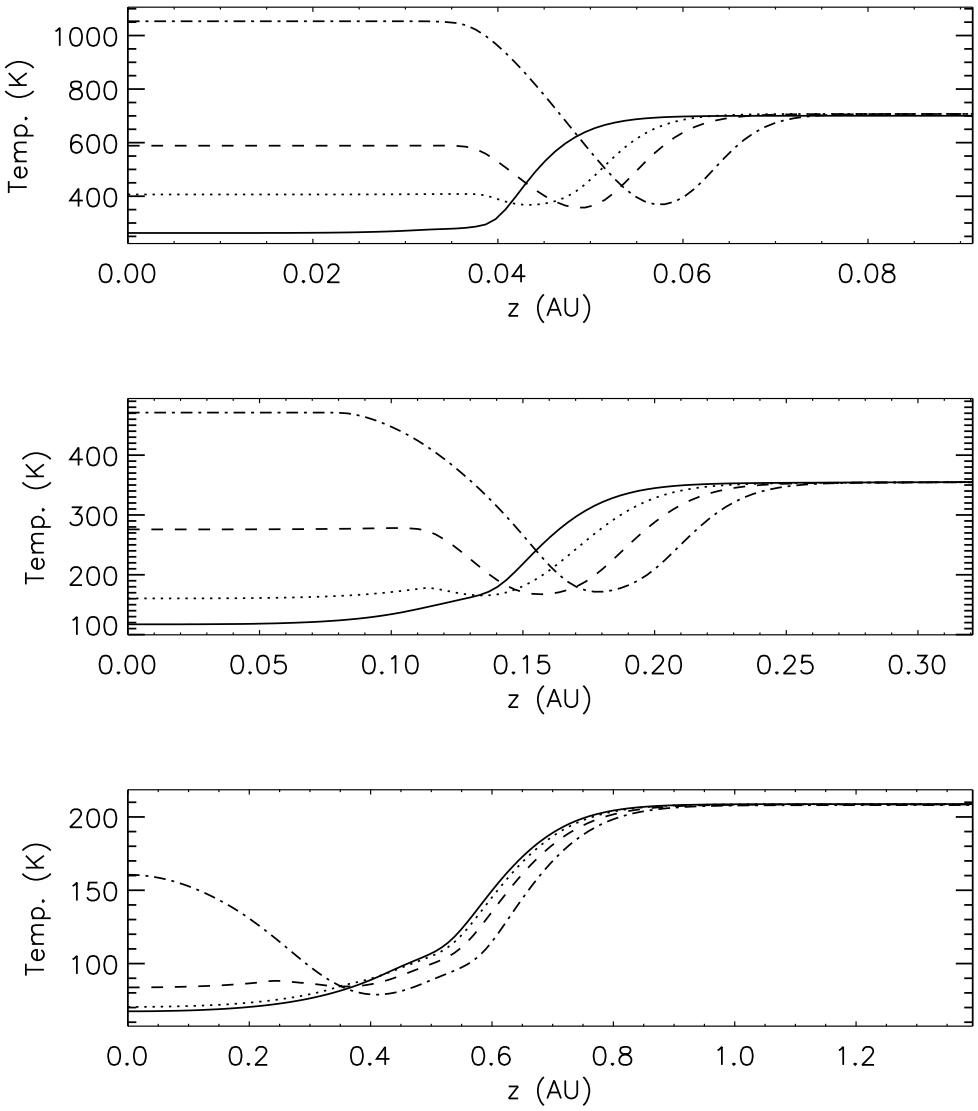

Figure 3.10: Same as Figure 3.8, but with $\dot{M} = 10^{-7}\,\mathrm{M}_{\odot}\,\mathrm{yr}^{-1}$.

above the 2nd number given would be the logarithm of Σ_a. For example, model number a1-2 would be a simulation with $\alpha = 10^{-1}$ and $\Sigma_a = 10^2$.

In Figure 3.11 we show the run of midplane temperature with distance from the star, $T_{mid}(r)$ for $\alpha = 10^{-3}$, 10^{-2} and 10^{-1}, for $\Sigma_a = 1\,g\,cm^{-2}$, $10\,g\,cm^{-2}$, and $100\,g\,cm^{-2}$. Higher values of α, as expected, lead to higher mass accretion rates and higher midplane temperatures. The case with $\alpha = 10^{-4}$ is indistinguishable from the passive disk case, even for an active layer of thickness $100\,g\,cm^{-2}$. Even for $\alpha = 0.1$ in the active layer, though, the temperature structure is little different from the passive disk case if $\Sigma_a \leq 10\,g\,cm^{-2}$.

We show the vertical temperature profiles at 0.3, 1, and 3 AU from the star, for various values of α, in Figures 3.12 ($\alpha = 10^{-3}$), 3.13 ($\alpha = 10^{-2}$), and 3.14 ($\alpha = 10^{-1}$). The vertical structures resemble those in Figure 3.8 through 3.10.

The $\alpha = 10^{-4}$ case was not displayed because its temperature structure matches the passive disk case. In fact, out of the 20 "layered-alpha models" that we generated, only 5 had a resultant temperature structure that differed significantly from the passive disk (assuming that the viscosity in the dead zone is 0). The models that were different were a3-2, a2-2, a1-1, a1-1.5, and a1-2. In all of these cases the temperature profiles match the passive disk at large enough r; only at small r do temperatures differ. In

	Σ_a ($g\,cm^{-2}$)				
α	1.0	3.0	10.0	30.0	100.0
10^{-3}	1.9×10^{-11}	5.8×10^{-11}	1.9×10^{-10}	5.8×10^{-10}	2.4×10^{-9}
10^{-2}	1.9×10^{-10}	5.8×10^{-10}	1.9×10^{-9}	6.9×10^{-9}	6.2×10^{-8}
10^{-1}	1.9×10^{-9}	5.8×10^{-9}	2.5×10^{-8}	1.8×10^{-7}	1.2×10^{-7}

Table 3.4: Equivalent mass accretion rates at 1 AU (in $M_\odot\,yr^{-1}$) for the same models presented in Table 3.3.

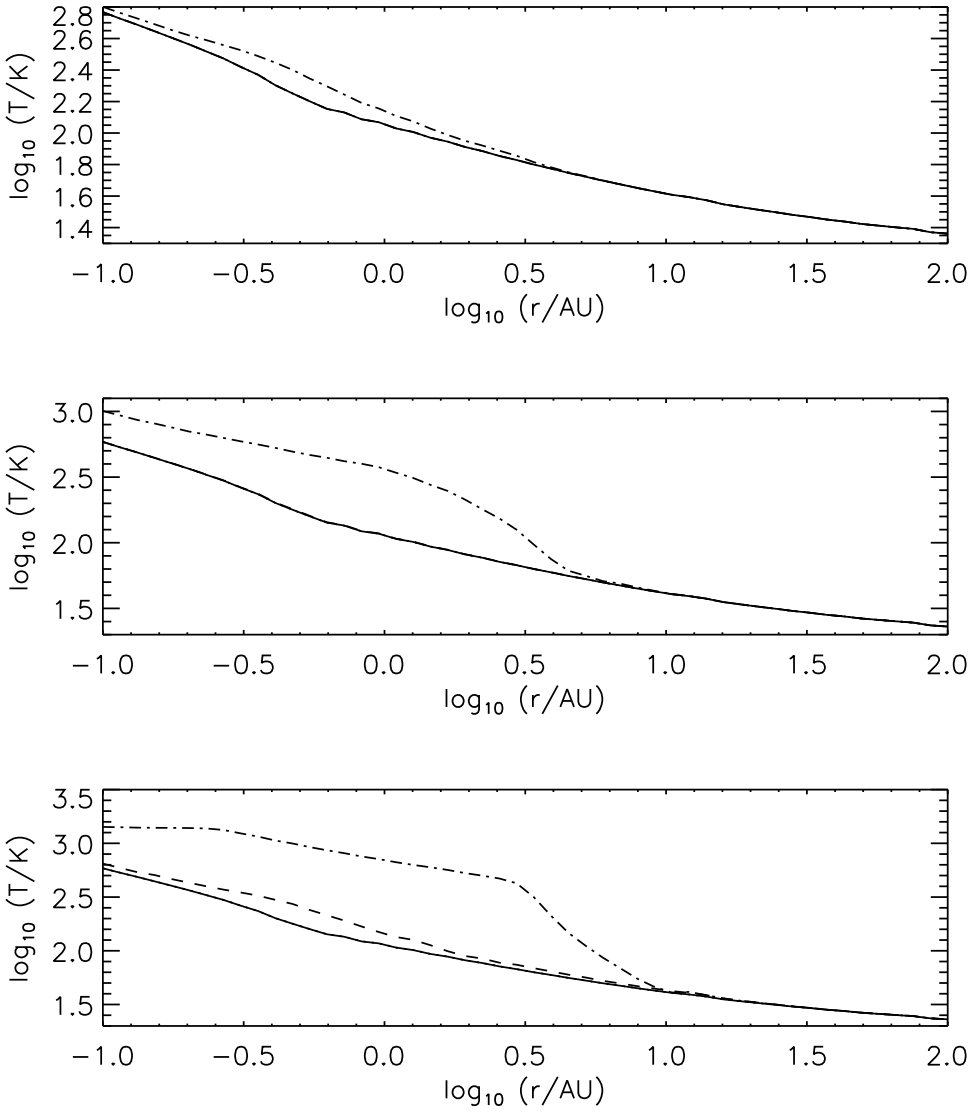

Figure 3.11: Midplane temperature $T_{\rm mid}(r)$ in actively accreting disks with viscosities calculated from the parametrized turbulent viscosity $\nu = \alpha c_s H$. Cases shown are $\alpha = 10^{-3}$ (top), 10^{-2} (middle), and 10^{-1} (bottom). For each α, 3 different layer thicknesses are shown: $\Sigma_a = 1.0$ g cm^{-2} (dotted), 10.0 g cm^{-2} (dashed), and 100.0 g cm^{-2} (dot-dashed) The passive disk is included for comparison as well (solid line).

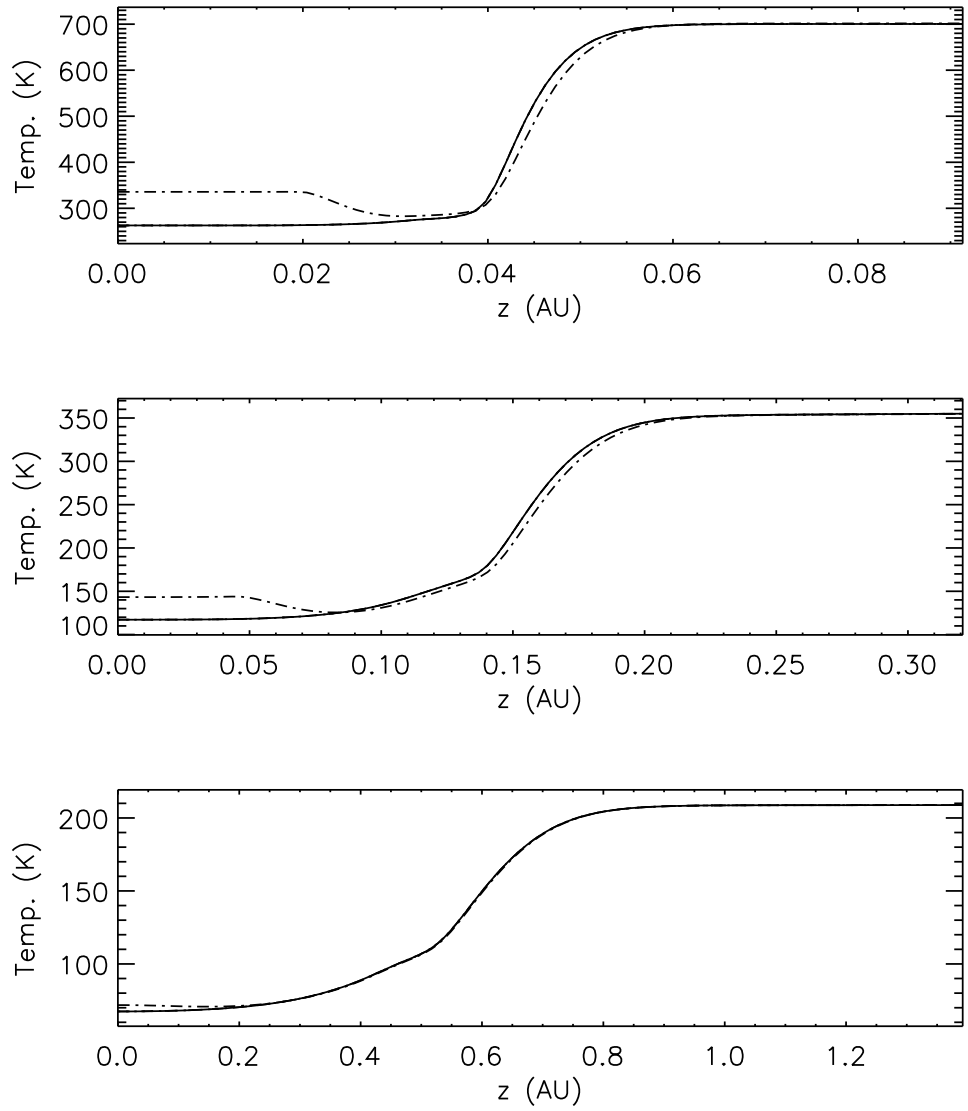

Figure 3.12: Vertical temperature structure of active disk with $\alpha = 10^{-3}$. Shown are vertical profiles from radii of 0.3 AU (top), 1 AU (middle), and 3 AU (bottom). The various active layer thicknesses are plotted in the same fashion as Figure 3.11: [$\Sigma_a = 1.0$ g cm^{-2} (dotted), 10.0 g cm^{-2} (dashed), and 100.0 g cm^{-2} (dot-dashed)].

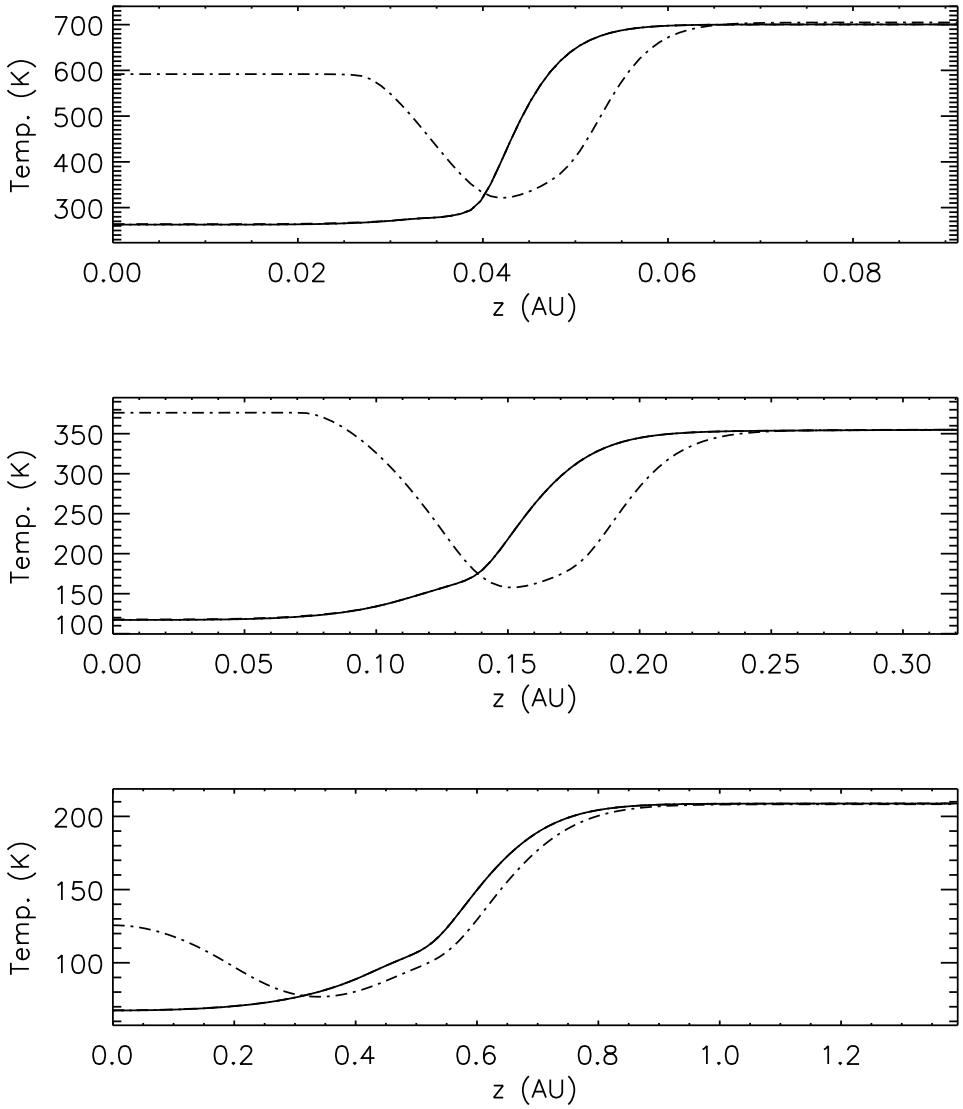

Figure 3.13: Same as Figure 3.12, but with $\alpha = 10^{-2}$.

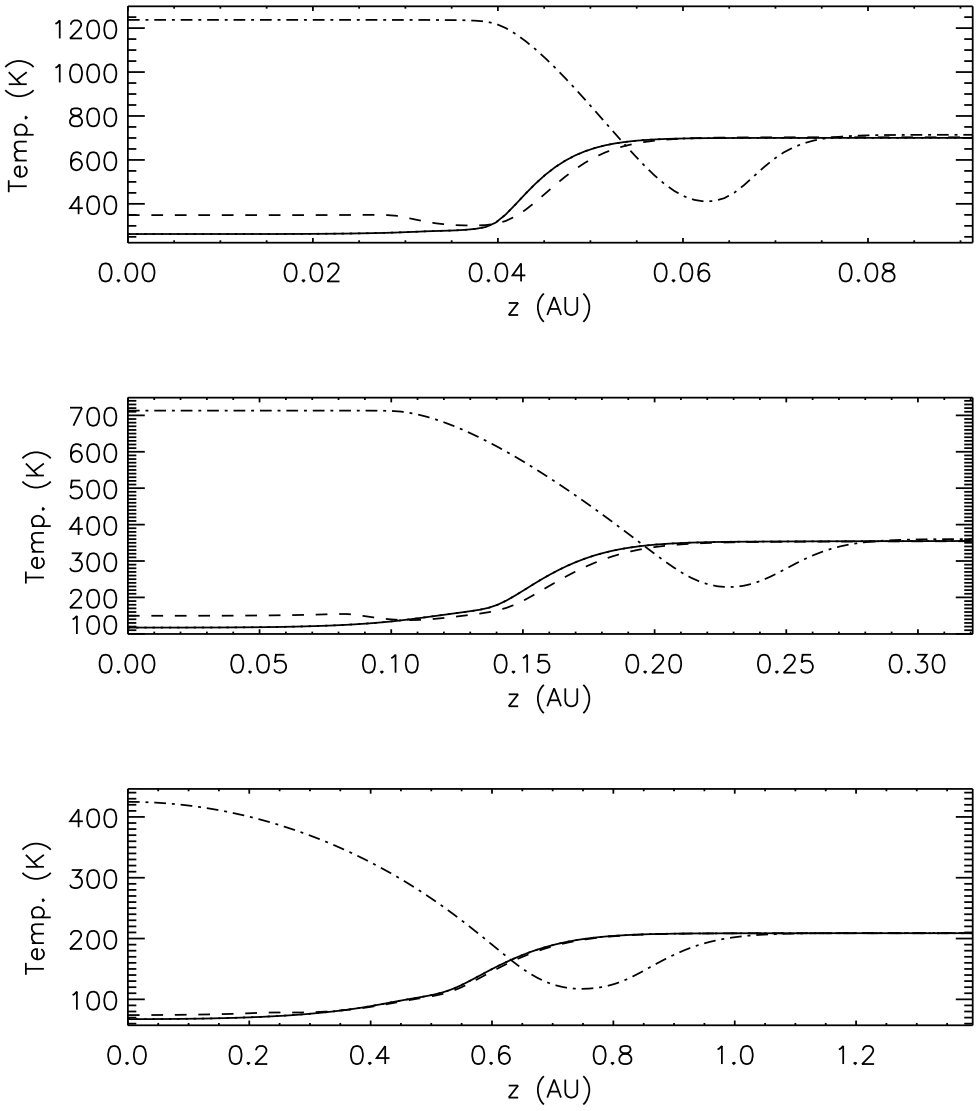

Figure 3.14: Same as Figure 3.12, but with $\alpha = 10^{-1}$.

general, the higher the quantity $\Sigma_a \alpha$ is, the further out accretional heating remains significant. Layered accretion does lead to changes in the temperature above the passive disk case, but they are relatively small.

3.6 Convection

It is instructive to consider the role of convection in these models. In Chapter 1 it was discussed how convection has been modeled to determine the source of the turbulence responsible for transporting material and exchanging angular momentum in the disk. The results of such modeling in each case found that convection cannot be the primary source of turbulence (Cabot et al. 1987a,b; Stone & Balbus 1996; Klahr et al. 1999; Klahr & Bodenheimer 2003). However, the characteristics of the temperature profiles (warmer layers lying about cooler layers) present the possibility for convection to play a secondary role in PPDs. Bell et al. (1997) found, in their models of uniformly accreting PPDs with fixed $\dot{M}$, that disks are generally unstable to convection at radii where the midplane temperature was between about 40 and 800 K. The energy flux carried by convection never exceeded about 10-20% of the total energy flux. However, the driving of convection nonetheless lowered the midplane temperature and increased the midplane density, and could, of course, lead to vertical transport. We investigated whether convection was present in disks accreting only in their surface layers. The criterion for instability is discussed in Chapter 2.

Table 3.5 lists whether convection was present (at any radii) for various combinations of $\dot{M}$ and Σ_a (both assumed uniform through the disk). The cases with $\dot{M} = 10^{-9}\, M_\odot\, \mathrm{yr}^{-1}$ were found to be stable against convection throughout. A handful of models with other $\dot{M}$ values were found to be convectively unstable. Model m8-2 exhibits convection for r ranging from 0.8

$\dot{M}$	Σ_a (g cm^{-2}) 1.0	3.0	10.0	30.0	100.0
10^{-9}	stable	stable	stable	stable	stable
10^{-8}	stable	stable	stable	stable	(0.8 AU $\lesssim r \lesssim$ 1.5 AU)
10^{-7}	stable	stable	stable	(1 AU $\lesssim r \lesssim$ 2.5 AU)	(1 AU $\lesssim r \lesssim$ 4 AU)

Table 3.5: Locations of convective instability in the uniform $\dot{M}$ models. If the entire disk is stable, it is labeled as "stable." Otherwise the range of unstable r is given. The units of $\dot{M}$ are $M_\odot$ yr^{-1}.

α	Σ_a (g cm^{-2}) 1.0	3.0	10.0	30.0	100.0
10^{-4}	stable	stable	stable	stable	stable
10^{-3}	stable	stable	stable	stable	stable
10^{-2}	stable	stable	stable	stable	(0.8 AU $\lesssim r \lesssim$ 4 AU)
10^{-1}	stable	stable	stable	(1 AU $\lesssim r \lesssim$ 4 AU)	(1.5 AU $\lesssim r \lesssim$ 7 AU)

Table 3.6: Same as Table 3.5, but for the models in which α in the active layer is fixed.

to 1.5 AU, m7-1.5 is unstable to convection for r between 1.0 and 2.5 AU, and m7-2 has convection for radii between 1.0 and 4.0 AU. In addition to m7-2 having the largest range in r where convection is relevant, it also was the only model where convection extended down to the midplane.

Convection information for our fixed α models is contained in Table 3.6. As before, almost all cases were stable against convection. Model a2-2 is unstable to convection between $r = 0.8$ and 4 AU, model a1-1.5 has convection for an r range of 1.0 to 4.0 AU, and model a1-2 (the most unstable case) exhibited convection for r between 1.5 and 7.0 AU.

Even with layered accretion, convection can occur, but it is much less widespread than the uniformly accreting case, even in PPDs with the same $\dot{M}$. For $\dot{M} = 10^{-7}\, M_\odot\, \mathrm{yr}^{-1}$, the entire disk is convectively stable if $\Sigma_a \leq 10\, \mathrm{g\, cm}^{-2}$. Disks with higher $\dot{M}$ are expected to be convectively unstable over larger portions of the disk, but again this depends on the value

of Σ_a.

3.7 The Snow Line

In this chapter we have presented our temperature results for passive disks, fully active disks, and disks undergoing layered accretion. As discussed in chapter 2, temperatures are solved for self-consistently with the rest of the disk's parameters. The importance of solving for temperatures in this fashion is of course that it reduces the assumptions made by the model and allows for an analysis of the temperature structure (such as spectral energy distributions) that would not be possible otherwise. However, it is also of considerable interest to determine where in disks midplane temperatures allow for water to sublimate and exist in the ice state. This physical location is known as the "snow line." Knowledge of where this demarcation exists in PPDs is important to the understanding of grain growth (Grigorieva et al. 2007), the formation of planetesimals (Kretke & Lin 2007), and eventually, planets, both gas giant and terrestrial (Kennedy et al. 2006; Garaud & Lin 2007). In the solar nebula, the snow line refers to the location of the $T_{\rm mid} = 170\,{\rm K}$ at the time when planetesimals began to form.

Due to varying conditions within disks, there is no one temperature value to trace for the snow line. In early models $T_{\rm snow} = 170\,{\rm K}$ was used as the snow line temperature in models of the minimum-mass solar nebula regardless of disk conditions (Hayashi 1981; Sasselov & Lecar 2000). However, Podolak & Zucker (2004) have recently shown that the snow line temperature depends on local mass density and can be as low as 145 K for more optically thin areas of a disk or nebula. Lecar et al. (2006) applied that to typical PPD conditions and calculated $T_{\rm snow}$ values for a gas densities ranging from 10^{-11} to $10^{-4}\,{\rm g\,cm^{-3}}$. Using those snow line temperatures Lecar

et al. (2006) find that for a disk with a mass of the minimum-mass solar nebula, the snow line varies between $r_{\rm snow} = 1.7$ if $\dot{M} = 1.0 \times 10^{-8}\,{\rm M}_\odot\,{\rm yr}^{-1}$ and $r_{\rm snow} = 2.7$ for $\dot{M} = 8.0 \times 10^{-8}\,{\rm M}_\odot\,{\rm yr}^{-1}$. These models included accretion heating at all heights in the disk by assuming a constant $\alpha = 0.01$ at all locations within the disk.

Using the gas density dependent snow line temperatures of Lecar et al. (2006) we have traced the snow line through my models presented here. The snow line temperatures were taken from Figure 3 in Lecar et al. (2006) by noting that when $T_{\rm snow}$ is plotted against $\log \rho_{\rm gas}$ the relation is close to linear. The temperatures are approximated by applying a 2-component piecewise linear fit to the figure. The snow line temperatures approximated were derived with the following relations:

$$T_{\rm snow} = 148\,{\rm K} + K_1 \log\left(\frac{\rho}{\rho_1}\right), \quad \rho < 10^{-7.5}\,{\rm g\,cm^{-3}} \tag{3.1}$$

$$T_{\rm snow} = 192\,{\rm K} + K_2 \log\left(\frac{\rho}{\rho_2}\right), \quad \rho > 10^{-7.5}\,{\rm g\,cm^{-3}} \tag{3.2}$$

where $K_1 = 10.7\,{\rm K/dex}$, $K_2 = 17.7\,{\rm K/dex}$, and ρ_1 and ρ_2 are 10^{-11} and $10^{-7}\,{\rm g\,cm^{-3}}$, respectively.

The passive disk model has a snow line radius of $r_{\rm snow} = 0.48\,{\rm AU}$. Our uniformly accreting disk (with $\alpha = 0.01$) has $r_{\rm snow} = 2.90\,{\rm AU}$. The results of the snow line analysis for our layered accretion models are shown in Tables 3.7 and 3.8. For the models with viscosities set directly by a uniform $\dot{M}$, the snow line increases with accretion rate and with active layer thickness, $\Sigma_{\rm a}$. Model m9-0 has the smallest $r_{\rm snow}$ value of 0.48 AU and model m7-2 has the largest value, 5.11 AU. This wide range in snow line positions, and its dependence upon accretion rate demonstrates how the snow line can move as the disk evolves. This will be explored in our subsequent discussion. The alpha-defined viscosity models show far less variance in the snow line

position. This is self-consistent with the temperature structures presented in §3.5. Since $T_{\rm mid}$ varies little for many of the models tested, a significant change in $r_{\rm snow}$ would be unexpected. Most of the models have $r_{\rm snow} = 0.48\,{\rm AU}$. As would be predicted from the midplane temperatures, model a1-2 has the largest change in $r_{\rm snow}$, placing it at 4.57 AU.

3.8 Residual Dead Zone Viscosity

The models presented here are generated under the assumption that within the dead zone, viscosity is zero. The extent of viscous dissipation in the dead zone is currently debated, and it is not clear whether the dead zone is associated with non-zero viscosity. Fleming & Stone (2003) have argued that the presence of an instability in the active layer can produce non-axisymmetric waves in the dead zone that would produce some residual turbulent viscosity with $\alpha \sim 10^{-4}$. Further numerical simulations of this have been run in 2D to test the effects of a non-zero dead zone viscosity on the time evolution of the disk (Wünsch et al. 2006). These simulations demonstrated that with a non-zero viscosity the dead zone boundary can fluctuate with time and can lead to time-varying accretion rates. Ilgner & Nelson (2008) created a series of shearing box models for disks depleted of dust grains (simulating late-stage PPDs) and found that for inner regions ($r < 10\,{\rm AU}$) where timescales of recombination are less than those of

	$\dot{M}\,({\rm M}_\odot\,{\rm yr}^{-1})$			
$\Sigma_{\rm a}\,({\rm g\,cm}^{-2})$	1.0×10^{-9}	1.0×10^{-8}	1.0×10^{-7}	1.0×10^{-6}
1.0	0.48	0.56	0.90	1.89
3.0	0.49	0.57	1.19	2.50
10.0	0.53	0.80	1.59	3.62
30.0	0.61	1.07	2.32	5.11
100.0	0.84	1.60	3.08	5.03

Table 3.7: Snow line locations (in AU) for layered accretion models with active layer viscosity defined by a uniform $\dot{M}$.

Σ_a (g cm^{-2})	$\alpha = 10^{-4}$	$\alpha = 10^{-3}$	$\alpha = 10^{-2}$	$\alpha = 10^{-1}$
1.0	0.48	0.48	0.48	0.48
3.0	0.48	0.48	0.48	0.48
10.0	0.48	0.48	0.48	0.82
30.0	0.48	0.48	0.73	2.87
100.0	0.48	0.75	2.58	4.57

Table 3.8: Snow line locations (in AU) for layered accretion models with active layer viscosity defined by a uniform parameter α.

turbulent mixing the interior regions of the disk were unable to sustain appreciable turbulence. They find that $10^{-6} \lesssim \alpha \lesssim 10^{-4}$ with a marginal increase for models where the magnesium gas content is elevated (which slows the recombination rates); however, even with extra magnesium $\alpha < 10^{-3}$. Oishi & Mac Low (2009) investigated investigated the ability for turbulence in the active layers to drive motions in the dead zone using three-dimensional, stratified, local, shearing-box, non-idea, magnetohydrodynamical simulations. They were testing whether vortexes could form. They found that vortexes could not be sustained and that the resulting turbulence (measured in α) reached a maximum sustained value of $\alpha \sim 10^{-3}$ for cases where dead zone material was perturbed at velocity dispersions of $\sigma = 0.8 c_s$. For smaller perturbations of $\sigma = 0.1 c_s$, the sustained α oscillated between 10^{-8} and 10^{-5}.

Turner & Sano (2008) have run numerical simulations of the MRI and have found that while the dead zone does not contain ionization strong enough to interact with the magnetic field, there is still nonzero magnetic stress in the dead zone, indicating turbulence. On the other hand, these simulations have been done where the ratio of dead zone mass to active layer mass is relatively small ($\lesssim 10$). Computational limits preclude numerical simulations with higher dead zone masses. With a massive enough dead zone, it is conceivable that these effects which enliven the dead zone may not

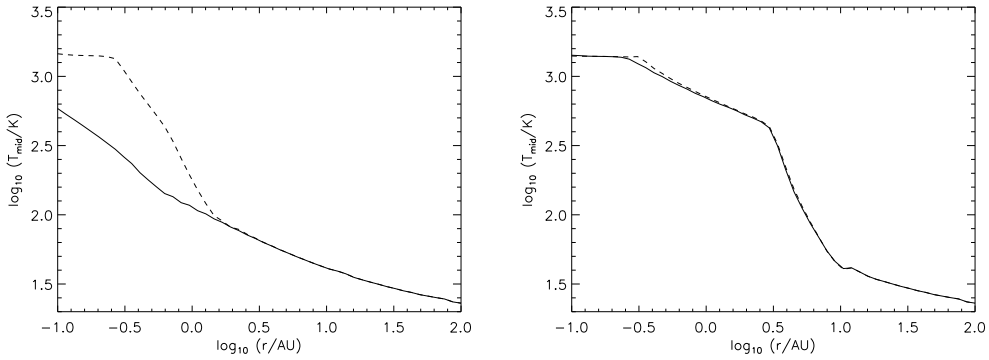

(a) $\Sigma_{\rm a} = 1\,{\rm g\,cm^{-2}}$ (b) $\Sigma_{\rm a} = 100\,{\rm g\,cm^{-2}}$

Figure 3.15: Midplane temperature, $T_{\rm mid}(r)$, for actively accreting disks with active layer $\alpha_{\rm a} = 10^{-1}$ and dead zone $\alpha_{\rm dz} = 10^{-4}$. Two active layer thicknesses are tested: (a) $\Sigma_{\rm a} = 1\,{\rm g\,cm^{-2}}$ and (b) $\Sigma_{\rm a} = 100\,{\rm g\,cm^{-2}}$. Each non-zero $\alpha_{\rm dz}$ run (dashed line) is compared to the case of $\alpha_{\rm dz} = 0$ (solid line). active zone $\alpha_{\rm a} = 10^{-1}$.

reach down to the midplane (Terquem 2008). For our layered models, $\Sigma_{\rm dz}/\Sigma_{\rm a}$ at 1 AU ranges between 10 and 1000. Nevertheless, non-zero α in the dead zone is a distinct possibility.

To test the effects of a non-zero accretion rate on midplane temperatures, we have lifted the assumption of $\alpha = 0$ in the dead zone and instead will set α to 10^{-4}. It has been suggested by Zhu et al. (2010) that dead zone α values of order magnitude smaller than that will have no effect on disk evolution and too large an α wouldn't be consistent with a residual viscosity. Therefore we consider two α values: a dead zone value, $\alpha_{\rm dz}$, and an active layer value, α. We have run 2 tests with active layer $\alpha_{\rm a} = 10^{-1}$ and $\alpha_{\rm dz} = 10^{-4}$: one with $\Sigma_{\rm a} = 1\,{\rm g\,cm^{-2}}$ and a second with $\Sigma_{\rm a} = 100\,{\rm g\,cm^{-2}}$ (see Figure 3.15). These are the smallest and largest active layer thickness considered in any of our models presented here. Since we are operating with a fixed power law surface density profile, this means that these two runs will also feature the smallest and largest dead zones ($\Sigma_{\rm dz} = \Sigma - \Sigma_{\rm a}$).

Fig. 3.15a demonstrates that allowing the dead zone viscosity to be a small non-zero number can have drastic effects on midplane temperature for radii inside a few AU. The midplane temperatures get warm enough in the inner 0.3 AU for the dust to reach its evaporation temperature. However, Fig. 3.15b shows that in other circumstances the effect of a residual dead zone viscosity can be relatively minor as well. In this case the change in $T_{\rm mid}$ is $<2\%$ at most radii, peaking to $\approx 12\%$ at $r \approx 0.3$ AU. This difference in the effects of adding a residual dead zone viscosity can be understood quantitatively in terms of accretional energy production. The accretional energy produced per annulus is $Q = (9/2)\Sigma_{\rm a}\nu_{\rm a}\Omega^2$, where ν is understood to be uniform within an annulus' active region. If we give the dead zone non-zero viscosity and impose $\alpha_{\rm dz} \ll \alpha_{\rm a}$, we find that the change to Q is to multiply it by $\xi = [1 + (\nu_{\rm dz}\Sigma)/(\nu_{\rm a}\Sigma_{\rm a})]$. ξ will be of order unity (little to no change in Q) when $\Sigma_{\rm a}/\Sigma \gg \nu_{\rm dz}/\nu_{\rm a}$. When $\Sigma_{\rm a} = 100\,{\rm g\,cm^{-2}}$, at 1 AU $\Sigma_{\rm a}/\Sigma = 0.1$, which is easily larger than $\nu_{\rm dz}/\nu_{\rm a} \sim 10^{-3}$. However, when $\Sigma_{\rm a} = 1\,{\rm g\,cm^{-2}}$, $\Sigma_{\rm a}/\Sigma = 10^{-3}$ at 1 AU, which is $\sim(\nu_{\rm dz}/\nu_{\rm a})$. This means that Q with a residual dead zone viscosity is roughly double Q with $\alpha_{\rm dz} = 0$.

Based on model results from the literature, we can perform a second analysis to compute ξ. Based on the shearing box models (Ilgner & Nelson 2008) and the dead-zone vortex analysis (Oishi & Mac Low 2009) an upper limit on $\alpha_{\rm dz}$ of 10^{-5} appears to be a conservative estimate. Based on the results presented in Chapters 3 and 5, an active layer thickness of $10\,{\rm g\,cm^{-2}}$ is appropriate. This yields $\xi = 1 + (10^{-5})(10^4)/(10^{-1})(10) = 1.1$, which is near unity. Lowering $\alpha_{\rm dz}$ further (which the models of Oishi & Mac Low (2009) suggest may be appropriate), would bring ξ closer to unity.

The net effect of residual viscosity in the dead zone depends sensitively on such factors as $\Sigma_{\rm a}$ and of course $\alpha_{\rm dz}$. Unfortunately, it is

unclear whether the dead zone viscosity should be in the important range $\alpha \geq 10^{-4}$. Because of this uncertainty we do not pursue further calculations of temperatures with nonzero dead zone viscosity. We note that constraints on dead zone viscosity are vital for computing PPD temperature structures.

3.9 Spectral Energy Distributions

Our models predict the temperature and density structure of PPDs, but direct tests of the model by astronomical observation require the prediction of spectral energy distributions, or SEDs. Having established the temperature structure of the disk, we use ray tracing techniques (the same used to find the variable Eddington factors) to determine the emergent spectra at a variety of disk inclinations to the line of sight. Because our emphasis is on predicting the differences made to the temperature structure by assuming layered accretion rather than uniform accretion, we have not focused on realistic dust models. Our opacity is that of a monodispersion of particles made of astronomical silicate, so we would not expect our models to predict actual PPD spectra. They can, however, be used to determine the magnitude of the difference in SEDs when considering layered vs. uniform accretion.

Figure 3.16 shows the emergent spectrum from face-on ($i = 0°$) disks experiencing a uniform inward accretion rate of $\dot{M} = 10^{-8}\,M_{\odot}\,\mathrm{yr}^{-1}$ (models m8-0, m8-1, and m8-2). The differences in emergent spectrum, which manifest themselves in the $3 - 20\,\mu$m wavelength region, are slight. Notably, they are no greater in magnitude than the $10\,\mu$m emission feature due to silicate grains in the superheated dust layer. It would be very difficult to disentangle the effects of layered accretion from the effects of varying composition and grain size. In Figure 3.17 we zoom in on the $3 - 30\,\mu$m wavelength region of emergent spectra for various $\dot{M}$. The emergent

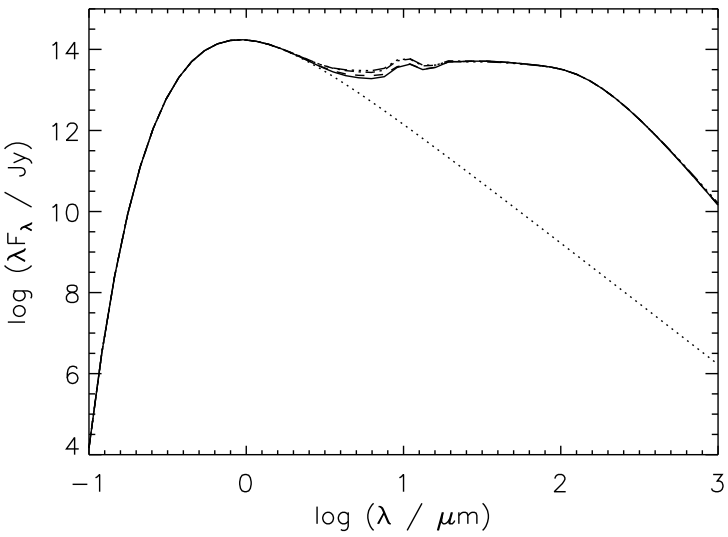

Figure 3.16: The spectral energy distributions (SEDs) for the models with mass flux set to a uniform $\dot{M} = 10^{-8}\,\mathrm{M}_\odot\,\mathrm{yr}^{-1}$ in the active layer. Three different active layer thicknesses are plotted: $\Sigma_\mathrm{a} = 1\,\mathrm{g\,cm}^{-2}$ (dashed), $10\,\mathrm{g\,cm}^{-2}$ (dot-dashed), and $100\,\mathrm{g\,cm}^{-2}$ (triple-dot-dashed). For comparison, the SED from the passive disk is shown as well (solid line). The dotted line represents the blackbody flux from the central protostar.

spectrum of the passive disk is shown for comparison in each. The $\dot{M} = 10^{-9}\,M_\odot\,\mathrm{yr}^{-1}$ layered accretion disk cases differ little from the passive disk case (models m9-0, m9-1, and m9-2 are shown). Slight differences with the passive disk arise when models m8-1 and m8-2 are compared to the passive case. When $\dot{M} = 10^{-7}\,M_\odot\,\mathrm{yr}^{-1}$ (models m7-0, m7-1, and m7-2) the layered accretion disks differ significantly from the passive disk, but there is relatively little variation in the SED as Σ_a is varied from $1\,\mathrm{g\,cm}^{-2}$ to $100\,\mathrm{g\,cm}^{-2}$.

We conclude that the degree of mass accretion does manifest itself in the SED of a disk, especially in the $3 - 30\,\mu$m wavelength region, but that the spatial distribution of that mass accretion (i.e. Σ_a) is equally important. It may be difficult to separate these effects, especially since dust composition, grain size, and degree of settling are also important factors in

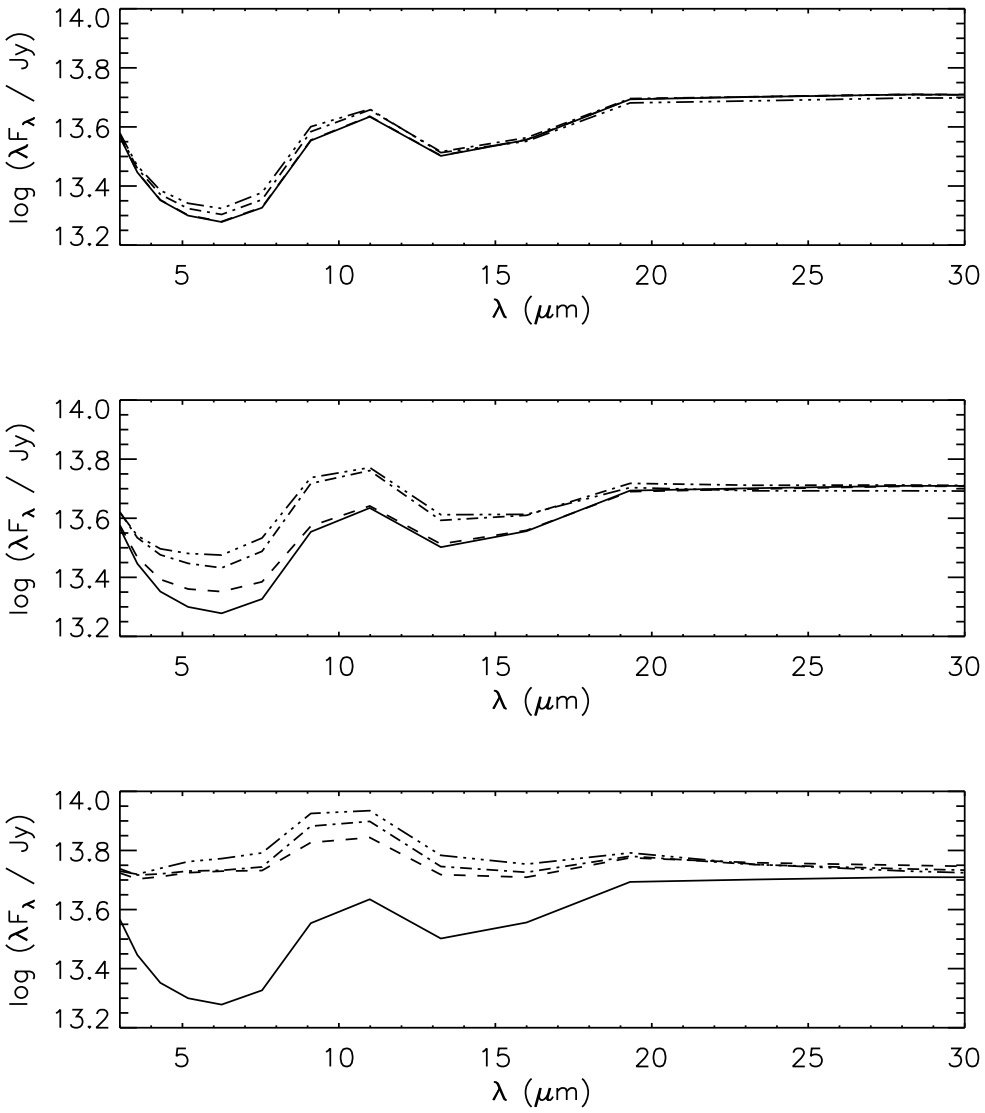

Figure 3.17: SEDs of disks undergoing layered accretion. Unlike Fig. 3.16, only the range $3\,\mu\mathrm{m} < \lambda < 30\,\mu\mathrm{m}$ is shown, as this is where differences between the model are manifested. Three $\dot{M}$ values are displayed: $\dot{M} = 10^{-9}\,\mathrm{M}_\odot\,\mathrm{yr}^{-1}$ (top), $\dot{M} = 10^{-8}\,\mathrm{M}_\odot\,\mathrm{yr}^{-1}$ (top), and $\dot{M} = 10^{-7}\,\mathrm{M}_\odot\,\mathrm{yr}^{-1}$ (top). Σ_a values shown are $1\,\mathrm{g\,cm}^{-2}$ (dashed), $10\,\mathrm{g\,cm}^{-2}$ (dot-dashed), and $100\,\mathrm{g\,cm}^{-2}$ (triple-dot-dashed). For comparison, the SED from the passive disk is shown as well (solid line).

setting the SED.

Chapter 4

Determining Active Layer Thicknesses

In Chapter 3 we demonstrated that the midplane temperatures in disks undergoing layered accretion depend on the thickness of the active layer. In that investigation, we allowed for Σ_a to be a free parameter and tested a range of appropriate values based on previous analyses and models (Gammie 1996; Sano et al. 2000). Additionally, each model was constrained to one uniform value of Σ_a over the whole disk, which is a gross simplification. It is of interest to self-consistently calculate Σ_a in all areas of the disk. In this chapter we will now calculate the active layer thickness assuming a fixed temperature.

As discussed in Chapter 1, the magnetorotational instability is most likely the means by which angular momentum is exchanged within the disk. Therefore, we assume that the MRI is present in PPDs. As noted previously, protoplanetary disks tend to be electrically neutral; however, a functional MRI requires ionized disk material. External sources of ionization will only be efficient at producing ionized gas in the surface layers of disks, which is the justification for layered accretion. In order for the instability to exist, the gas must be sufficiently ionized to couple with the **B**-field. An ionization level of $n_e/n_{\rm H2} \gtrsim 10^{-13}$ is commonly adopted as a criterion for an MRI to operate; however, this itself is a complicated condition which is dependent on the ability of the gas to decouple from the magnetic field via the processes of Ohmic dissipation, ambipolar diffusion, and the Hall effect. These processes, in turn, depend on the strength of the B-field, ρ, and T. Since density and temperature are height-dependent quantities, we need to know the ionization state of the disk at all heights as well. This chapter will be dedicated to

establishing these values.

If the gas in the disk is sufficiently ionized to become coupled to the field, an MRI can occur. Electrons and ions frozen to the field will become radially displaced as perturbations pass through the magnetic field. Differential rotation of the material along a common field line will attempt to shear the ions and electrons apart, stretching the field line and introducing tension. The radial component of the tension will serve as a restoring force, providing stability. The azimuthal component, by imposing a torque on the fluid elements, is destabilizing. If the magnetic field is strong enough that the restoring radial force dominates, or if the gas is insufficiently coupled to the magnetic field, then the instability will grow. Angular momentum will be transferred via the magnetic field, the instability will feed off the disk's differential rotation, and the magnetic field will become turbulent and tangled.

Our goal in this chapter is to determine where protoplanetary disks are locally unstable to the linear growth of the MRI. In §4.1 we outline the magnetic diffusion processes that can potentially stabilize the disk against the MRI: Ohmic dissipation, ambipolar diffusion, and the Hall effect. The effects of these processes on the growth of the MRI depends on the ionization state of the gas in the disk. Our method for calculating this is presented in §4.2.

4.1 Magnetic Diffusion and the MRI

We begin the discussion of where the MRI can operate with a review of the primary magnetic diffusion processes. The first, Ohmic dissipation, is a process by which magnetic flux is decreased via collisions with the charged particles gyrating about the field lines. Left alone, these particles would gyrate indefinitely and be frozen to the **B**-field. However, collisions with

neutral gas molecules and with other ions and electrons will interrupt this motion, providing resistance to the currents generated by the moving charges and changing the current density. The changes to the current will serve to dissipate the magnetic flux. Jin (1996) included Ohmic dissipation in his linear analytic analysis of the MRI and found that the instability will be damped if the Ohmic diffusion rate is higher than the growth rate of the instability. Ohmic dissipation is especially important in the midplane regions of PPDs, where high number densities and low ionization rates from X-rays and cosmic rays lead to a suppression of the instability (Jin 1996; Gammie 1996). Fleming et al. (2000) numerically simulated the effects of Ohmic dissipation in the non-linear regime. Their simulations during linear growth phases of the MRI largely agreed with the linear analyses performed previously.

Ambipolar diffusion as a magnetic flux reducing effect exists due to the relatively small population of charged particles. The neutral material in the gas will not be directly effected by the **B**-field. Therefore, while the neutral gas moves inward toward the protostar, the electrons and ions will resist the motion, being frozen to the magnetic field. This effect is significant when the direction of neutral gas motion is at a right angle to the **B**-field (e.g. gas moving in the $\hat{\mathbf{e}}_r$ direction, with $\mathbf{B} = B\hat{\mathbf{e}}_z$). In the frame of the gas, the electrons, ions, and field lines are moving outward, resulting in a decreasing magnetic flux in the disk. The analytical model of Regos (1997) shows that ambipolar diffusion becomes important in regions of low density and high ionization fractions. According to the linear analysis of Blaes & Balbus (1994), instabilities will exist in this "ambipolar regime" when the collision frequency between ions and neutral particles is greater than the orbital frequency. As the frequency between collisions decreases, weaker

magnetic fields are necessary for instabilities to avoid damping. The results of this linear analysis were supported by the modeling work of Mac Low et al. (1995), which introduced ambipolar diffusion into the ZEUS magnetohydrodynamic code. Fluid simulations presented in Hawley & Stone (1998) found that in order to achieve instability in a non-linear environment, a larger coupling of neutrals to ions is required (than would be for linear instability).

Finally, the Hall effect is the well known process by which charged particles move not only in response to an imposed electric field, but will also move in response to a magnetic field. The direction of the drift will be at right angles to **E** and **B**. Wardle (1999) found that in order for the Hall effect to make the MRI grow, the ratio of collision frequency to orbital frequency, χ, must be $> (v_{\rm A}/c_{\rm s})^2$. Hall conductivity will substantially modify the behavior of the MRI when $\chi \lesssim 1$ and there is a limited range of χ for all wavenumbers of the instability to grow (Wardle 1999). Wardle & Ng (1999) demonstrated that for single-size dust grains of $a_{\rm gr} = 0.1\,\mu$m, the Hall term is not significant.

Desch (2004) studied the MRI via a linear analysis assuming small amplitude perturbations to find the dispersion relation, the relationship between MRI growth rate and wavenumber. In this analysis arbitrary wavevector directions and magnetic fields were considered. The goal was to find a positive growth rate in the linear regime. From this linear stability analysis, Desch (2004) was able to derive a general case instability criterion for instability. For our purposes, we do not need to apply the general case, but can rather make further simplifications. First, we assume that the magnetic field is aligned with the disk's rotation axis (i.e. $\mathbf{B} = B_z\hat{\mathbf{e}}_z$), where we have adopted a cylindrical coordinate system for the disk with rotation

axis in the $\hat{\mathbf{e}}_z$ direction. We consider a wavevector of the instability in the $\hat{\mathbf{e}}_k$ direction and define θ as the angle between $\hat{\mathbf{e}}_z$ and $\hat{\mathrm{e}}_k$. The magnitude and sign of $\hat{\mathbf{e}}_z \cdot \hat{\mathbf{e}}_k$ is $\cos\theta$ and s, respectively. For the simplified case described here for a PPD with a magnetic field aligned with the rotation axis, Desch (2004) found that the disk will be unstable if

$$\frac{1}{\cos^2\theta}\left(\frac{D_{\mathrm{OD}}}{v_{\mathrm{A}}^2/\Omega}+\frac{D_{\mathrm{AD}}}{v_{\mathrm{A}}^2/\Omega}\right)\left(\frac{D_{\mathrm{OD}}}{v_{\mathrm{A}}^2/\Omega}\right)+\left(\frac{D_{\mathrm{OD}}}{v_{\mathrm{A}}^2/\Omega}+\frac{D_{\mathrm{AD}}}{v_{\mathrm{A}}^2/\Omega}\right)\left(\frac{D_{\mathrm{AD}}}{v_{\mathrm{A}}^2/\Omega}\right) + \left(\frac{5}{4}+\frac{sD_{\mathrm{H}}}{v_{\mathrm{A}}^2/\Omega}\right)^2-\frac{9}{16}<\frac{3\Omega^2}{k^2v_{\mathrm{A}}^2}\left(1+\frac{1}{2}\frac{sD_{\mathrm{H}}}{v_{\mathrm{A}}^2/\Omega}\right), \tag{4.1}$$

where D_{OD}, D_{AD}, and D_{H} are the diffusion coefficients of Ohmic dissipation, ambipolar diffusion, and the Hall effect (to be defined below), respectively, v_{A} is the Alfven wave speed, $\cos\theta = \hat{\mathbf{e}}_k \cdot \hat{\mathbf{e}}_z$ (specific to a magnetic field aligned with the z-axis), and Ω is the Keplerian frequency of the disk.

The diffusion coefficients can be defined in terms of the conductivities of the gas. As stated above, the dissipative effects are dependent on how the current direction compares to the direction of $\mathbf{B}$. Therefore, it is important to define the conductivities relative to $\mathbf{B}$ as well. From Desch (2004):

$$\sigma_{\parallel} = \sum_a \sigma_a \tag{4.2}$$

$$\sigma_{\perp} = \sum_a \frac{\sigma_a}{1+(\omega_a\tau_{an})^2} \tag{4.3}$$

$$\sigma_{\mathrm{H}} = \sum_a \frac{\sigma_a(\omega_a\tau_{an})}{1+(\omega_a\tau_{an})^2}, \tag{4.4}$$

where $w_a = q_aB/m_ac$ is the gyrofrequency of species a of charged particles about the magnetic field (q_a and m_a are the charge and mass of the species, respectively), τ_{an} is the mean timescale for momentum exchange with neutral particles, and $\sigma_a = n_aq_a^2\tau_{an}/m_a$ is the species' electrical conductivity. Based on Desch & Mouschovias (2001), Desch (2004) assumed that for typical conditions in a PPD, electrons will interact with neutral molecules on timescales of $\tau_{en} \approx 0.6\,(\rho_n/10^{-9}\,\mathrm{g\,cm^{-3}})^{-1}\,\mu$s and ions will interact on

timescales of $\tau_{in} \approx 6\,(\rho_n/10^{-9}\,\mathrm{g\,cm^{-3}})^{-1}\,\mu$s. With these conductivities defined, we can now define the diffusion coefficients D_{OD}, D_{AD}, and D_{H} (Desch 2004):

$$\begin{aligned} D_{\mathrm{OD}} &= \frac{c^2}{4\pi}\left(\frac{1}{\sigma_\parallel}\right) \\ D_{\mathrm{AD}} &= \frac{c^2}{4\pi}\left(\frac{\sigma_\perp}{\sigma_\perp^2+\sigma_{\mathrm{H}}^2}\right) \\ D_{\mathrm{H}} &= -\frac{c^2}{4\pi}\left(\frac{\sigma_{\mathrm{H}}}{\sigma_\perp^2+\sigma_{\mathrm{H}}^2}\right) \end{aligned} \tag{4.5}$$

Calculating the thickness of the active layer (with fixed temperature) means first establishing the ionization state of the disk material (to be covered in the next section). The ionization state is then used along with the magnetic field strength, B, to calculate the diffusion coefficients D_{OD}, D_{AD}, and D_{H}. These coefficients are then put into the instability criterion. We test various altitudes. We start at the top of the disk and test for stability. If the layer is found to be unstable, we test a lower altitude. This process is repeated until we find an altitude that produces a stable layer and works because of the density sensitivity of stability. Details of how we make those computations will be discussed in the following subsections.

4.2 Calculating Ionization States in the Disk

Protoplanetary disks are composed of gas (mostly H_2, but also H, He, CO and other molecules) as well as dust grains. The disk in bulk is electrically neutral. However, some of the disk material can become ionized, usually via external processes. We define ionization rates as the rate at which electrons are liberated from hydrogen molecules, the primary constituent of the PPD gas. Galactic cosmic rays (Umebayashi & Nakano 1981), protostellar x rays (Glassgold et al. 1997a), and radioactivity within the disk (primarily ^{26}Al, which has a half-life of 0.717 Myr producing an ionization rate of

$3.7 \times 10^{-19}\,\mathrm{s}^{-1}$ per H_2, see Turner & Drake 2009) all can cause a fraction of the disk material to become electrically charged. There are also ionization events that result from the thermal motions of the gas particles, collisions with potassium atoms can yield free electrons. However, this thermal ionization is inefficient at $T \lesssim 10^3\,\mathrm{K}$ (Gammie 1996). The Monte Carlo code of Igea & Glassgold (1999) demonstrated that for regions near the star, x-ray ionizations dominate over all other sources. Appropriate x-ray ionization rates for PPDs can be calculated via the following equation (from equations 7, 8, and 9 in Glassgold et al. 1997a,b)

$$\zeta_{\mathrm{xr}} = \left(6 \times 10^{-11}\,\mathrm{s}^{-1}\right) \left(\frac{r}{1\,\mathrm{AU}}\right)^{-2} \sigma_{-22} E_{\mathrm{xr}}^{-n} L_{\mathrm{xr}} A \tau_{\mathrm{xr}}^{-a} \exp^{-B\tau_{\mathrm{xr}}^{b}}, \qquad (4.6)$$

where r is the distance from the central star, σ_{-22} is the x-ray photoionization cross section, scaled to $10^{-22}\,\mathrm{cm}^2$, E_{xr} is the mean energy of the x rays (typically, a mean value of 5 keV is assumed and will be used here), L_{xr} is the x-ray luminosity of the protostar (similar to Glassgold et al. (1997a) we use $L_{\mathrm{xr}} = 10^{29}\,\mathrm{erg\,s}^{-1}$ here), and τ_{xr} is the optical depth to x rays as measured vertically from the top of the disk. The values A, B, a, and b are coefficients chosen by Glassgold et al. (1997a) to best approximate the actual dependence of ionization rate with τ_{xr} found from their Monte Carlo runs. These constants depend on the metal abundances of the disk material. Glassgold et al. (1997a) presented two sets of equation constants for different abundance assumptions. We chose the set appropriate for the case of severe heavy element depletion: $n = 2.81$, $\sigma_{-22} = 0.85$, $a = 0.606$, $b = 0.262$, $A = 0.686$, and $B = 1.778$. The x-ray optical depth is computed via

$$\tau_{\mathrm{xr}} = 763 \left(\frac{r}{1\,\mathrm{AU}}\right) \Sigma_{\mathrm{a}} \sigma_{-22} E_{\mathrm{xr}}^{-n} \qquad (4.7)$$

It is important to note that the x-ray ionization discussed in Glassgold et al. (1997a) is dependent upon an assumed flaring index,

$\eta = d/dr(H/r)$. In Glassgold et al. (1997a), $\eta = 0.25$ was assumed. This is a fairly typical value for PPDs (e.g. Dullemond et al. (2002) use $\eta = 2/7$ as a starting guess when they self-consistently calculate that value in their models). As discussed in Chapter 3, our uniformly active disk has η ranging from 0.1 to 0.3 through the disk. Our layered accretion disks have flaring indices that range between 0.16 and 0.22. Altering the flaring index has the net effect of modifying the coefficients a, b, A, and B discussed above. However, given that our flaring index values are generally close to the value in Glassgold et al. (1997a), we expect that the differences in these coefficients would be minimal. In any event, there aren't x-ray ionization models available for an range of η, which is what would be needed in any situation where the flaring index is a self-consistently calculated parameter that is not held at a single uniform value throughout the disk. Determining those ionization parameters is well beyond the scope of this paper and we will be using the coefficients of Glassgold et al. (1997a) with that caveat.

Naturally, recombinations will bring the level of ionization to an appropriate equilibrium. For a disk entirely composed of gas, the recombination timescales depend on the gas density, n_g, density of electrons, n_e, ion density, n_i, and the temperature, T. However, there are also a significant number of dust grains present (dust-to-gas ratios of order 10^{-2} are commonly considered). Dust grains serve as catalysts for recombination: the grains' surfaces are places where electrons and ions can interact more frequently (see Draine & Sutin (1987)). Additionally, the dust grains can themselves become negatively or positively charged if electrons or ions stick to them following a collision. The ionization chemistry of the disk is therefore complicated: Electrons are being liberated from gas molecules, resulting in a soup of electrons, ions, and neutral gas. Electrons and ions can

either recombine via a series of reactions (as a function of dust grain density, $n_{\rm gr}$) or stick to dust grains following collisions. Charge is constantly being exchanged between gas species and dust grains. Evaluating the ionization state of the disk takes more than an analysis of ionization sources, the chemical network of the disk must be solved as well.

Previous Charge Chemistry Networks

A variety of networks have been used in recent years, each of which has its own strengths and weaknesses. The MRI calculations of Sano et al. (2000) were done using the ionization network of Umebayashi & Nakano (1990) and Nishi et al. (1990), which were created to describe charge exchange reactions in dense interstellar cloud circumstances. In his treatment, Sano et al. (2000) included 7 ion species (H^+, $H_2^+, H_3^+, He^+, C^+, m^+, M^+$) along with grains with a net electric charge range of $|Z| \leq 3$, where grain charge $q = Ze$. The ions m^+ and M^+ are a molecular and metal ion, respectively. A total of 38 charge exchange reactions are considered in their model. Three are through dissociation, 16 are ion/molecule interactions, 7 are recombination reactions, and 12 involve grain collisions. (For a detailed list see Sano et al. 2000.)

Ilgner & Nelson (2006) extended the ionization network utilized by Sano et al. (2000) to include 173 neutral and ion species. This list of species contained the elements H, He, C, O, N, S, Si, Mg, and Fe (for a full list of molecules used see Ilgner & Nelson 2006). They also reduced the range of allowed grain charges slightly; only 5 charge states were used ($|Z| \leq 2$). Neutral and charged gas molecules were allowed to inelastically collide and stick. Grains also were permitted to collide with gas molecules/ions without sticking, exchanging charge between the particles. Grain-grain collisions were considered as well with charge exchange resulting. In general, 18 different

gas-grain and grain-grain charge exchange reactions were considered.

While these two models were not the first to include gas-grain collisions in their ionization simulations (Willacy et al. 1998; Willacy & Langer 2000; Markwick et al. 2002 developed prior models with gas-grain collisions), they were the first to include charged grains. The above discussed chemistry networks used collision rates between ions, electrons, and grains determined using the treatment of Draine & Sutin (1987). They then expanded by using a broad spectrum of gas species. While their attention to detail regarding the gas reactions is appropriate for the calculations, the small range of grain charges considered leaves open the possibility that a broader population of grain charge states could significantly affect the electron and ion densities and therefore the electrical conductivities and extent of the dead zone. We attempt to address that in our method.

Our Charge Chemistry Network

As with the previous models addressed above, our ionization network consists of two components: gas-phase chemistry and grain chemistry. We will outline our gas-phase chemistry first. Table 4.1 lists the ionization and recombination reactions we assume occur in a PPD. Since the disk is in bulk electrically neutral, we assume that the reaction sequence begins with the liberation of a free electron and ends with a recombination of a free electron. Reaction 1 is considered the source of free electrons. Since an overwhelming majority of the disk material is gas (dust to gas ratios of 0.01 are typical in PPD models) and the dominant gas species in cold environments is H_2, ionization sources will most likely interact with molecular hydrogen. In general, the reaction cycle proceeds in numerical order through Table 4.1. Not all of these reactions happen at the same rate. The bottleneck is

No.	Reaction
1	$H_2 \rightarrow H_2^+ + e^-$
2	$H_2^+ + H_2 \rightarrow H_3^+ + H$
3	$H_3^+ + CO \rightarrow HCO^+ + H_2$
4	$HCO^+ + e^- \rightarrow H + CO$
A	$X^+ + g(Z) \rightarrow g(Z+1)$
B	$e^- + g(Z) \rightarrow g(Z-1)$

Table 4.1: Gas-phase (reactions 1-5) and dust-phase (reactions 6-7) chemistry reactions taking place in our model. X^+ represents any positive molecular ion and g(Z) is a dust grain with net charge $q = Ze$.

reaction 4: the recombination of electrons with HCO^+ ions. Therefore, for the purposes of modeling the gas-phase ionization in the disk, we can use its reaction rate as our rate of molecular dissociative recombination, $\beta_{\rm dr}$. A temperature dependent rate coefficient of $\beta = (2 \times 10^{-6}) T^{-1/2}\,{\rm cm^3\,s^{-1}}$ is appropriate for dissociative recombination of electrons with molecular ions in the presence of large grains (Umebayashi & Nakano 1988, 1990).

To accurately simulate the electron and ion fractions in the gas, it is important to also model grain chemistry. It is not unreasonable to only consider charged gas populated by particles with $q = \pm 1e$ (neutral gas, singly ionized gas, and electrons); however, ions and electrons can be absorbed by dust grains without chemically reacting, causing them to occupy a range of charge states. We define charge state, Z, such that the grain's charge is $q = Ze$. Table 4.1 lists the two general grain chemistry reactions. In reaction "A," a singly ionized molecule collides and sticks to a grain, increasing its net charge by $1e$. Reaction "B" decreases the net charge of a grain through a collision with a free electron. While simple in concept, the complexity of the model grows exponentially as the range of allowed charge states grows. For example, the simplest case would be to consider grains in 3 charge states: $Z = -1, 0, +1$. However, the Coulomb force dictates that the interaction

timescales will be different for each charge state; each of these six timescales would need to be calculated in order to correctly simulate the disk's grain and ion populations. This limited consideration of charge states is inadequate to ascertain an accurate calculation of the disk's ionization with respect to grain charge. First, the number of charge states neglects the presence of doubly or more ionized dust grains. Second, such a charge setup assumes that even with ionization effects acting on the disk, the median grain charge is near zero. This last assumption is made in the ionization models used by Sano et al. (2000) and Ilgner & Nelson (2006). This introduces a potential source of error in the chemistry network: The range of Z considered by the model may either not contain the median grain charge or it may be so close to one of the endpoints that a significant fraction of dust grains have their charges incorrectly calculated. This then affects the calculated rates of electrons/ions sticking to grains. To account for this we need to estimate an appropriate value for the median charge of a particle and consider a large enough range of charge states about it.

To calculate the rates of grains interacting with ions and electrons, we start with the model of Draine & Sutin (1987). They derived a rate for grain interaction with particles of various mass and charge, including the induced dipole moment of grains previously neglected. We introduce rates of ions and electrons colliding with grains:

$$J_{\rm i}(z) = \pi a_{\rm gr}^2 \left(\frac{8kT}{\pi m_{\rm i}}\right)^{1/2} n_{\rm i} \tilde{J}_{\rm i}(T, Z) \tag{4.8}$$

$$J_{\rm e}(z) = \pi a_{\rm gr}^2 s_{\rm e} \left(\frac{8kT}{\pi m_{\rm e}}\right)^{1/2} n_{\rm e} \tilde{J}_{\rm e}(T, Z), \tag{4.9}$$

where the i and e subscripts refer to ions and electrons, respectively, $a_{\rm gr}$ is the dust grain radius, $s_{\rm e}$ is the electron sticking coefficient for collisions with grains (a similar value for ions is approximated to unity), and $\tilde{J}_n(T, Z)$ is the

normalized charge-dependent collision rate for ions and electrons, as derived by Draine & Sutin (1987).

$$\tilde{J}_{\rm n}(T,Z) = \int_0^\infty dx\, x\, e^{-x}\, \tilde{\sigma}\left(\epsilon = x\,\frac{akT}{q_i^2},\, \nu = \frac{Ze}{q_i}\right)$$

where $\tilde{\sigma}$ is a reduced cross section (see Appendix B of Draine & Sutin 1987).

We assume ionization equilibrium, that is, the rate of free electron "production" (ionization) is equal to electron "destruction" (dissociative recombination and inelastic charge sticking to grains) and the rate of ion production is equal to ion destruction. This assumption yields the following equations:

$$\zeta n_{\rm H2} = \beta_{\rm dr} n_{\rm i} n_{\rm e} + \sum_Z n_{\rm gr}(Z) J_{\rm i}(Z) \tag{4.10}$$

$$\zeta n_{\rm H2} = \beta_{\rm dr} n_{\rm i} n_{\rm e} + \sum_Z n_{\rm gr}(Z) J_{\rm e}(Z) \tag{4.11}$$

We also apply the condition that the disk is electrically neutral. The net charge per unit volume should be 0.

$$n_{\rm i} - n_{\rm e} + \sum_q Z_q n_{\rm gr}(Z_q) = 0 \tag{4.12}$$

We solve for the disk's ionization in a three step process, each step further refining the solution. Our goal is to determine $n_{\rm i}$, $n_{\rm e}$, an appropriate range of charge states for the dust grains, Z_q, and the fractional population of each charge state, $f_q(Z)$. Instead of centering our grain charge range on $Z = 0$, we will make an estimate of the median charge, $\langle Z \rangle$, and center our grid on that.

The first step will determine $\langle Z \rangle$ by finding a solution to the ionization assuming all grains are at the same charge. Once we reach a solution the resulting grain change will be used as $\langle Z \rangle$. Together, equations 4.10 and 4.11 contain 2 unknowns if we adopt $\beta_{\rm dr}$ for the limiting reaction

discussed above (reaction 4b) and a dust to gas ratio. Simplifying the sum over grain charge states and expanding the collision rates $J_n(\langle Z \rangle)$ yields:

$$\zeta = \beta_{\rm dr} n_{\rm H2} x_{\rm i} x_{\rm e} + \pi a_{\rm gr}^2 n_{\rm gr}(\langle Z \rangle) \left(\frac{8kT}{\pi m_{\rm i}} \right)^{1/2} x_{\rm i} \tilde{J}_{\rm i}(T, \langle Z \rangle) \tag{4.13}$$

$$\zeta = \beta_{\rm dr} n_{\rm H2} x_{\rm i} x_{\rm e} + \pi a_{\rm gr}^2 n_{\rm gr}(\langle Z \rangle) s_{\rm e} \left(\frac{8kT}{\pi m_{\rm e}} \right)^{1/2} x_{\rm e} \tilde{J}_{\rm e}(T, Z), \tag{4.14}$$

where we have introduced $x_{\rm i} = n_{\rm i}/n_{\rm H2}$ and $x_{\rm e} = n_{\rm e}/n_{\rm H2}$, the fractional ion and electron populations, respectively.

Subtracting Eq. 4.14 from Eq. 4.13 leaves a linear relation between $x_{\rm i}$ and $x_{\rm e}$:

$$x_{\rm e} = x_{\rm i} \left(\frac{m_{\rm e}}{m_{\rm i}} \right)^{1/2} \frac{\tilde{J}_{\rm i}}{s_{\rm e} \tilde{J}_{\rm e}} \tag{4.15}$$

Combining Eqs. 4.13 and 4.15 yields a quadratic equation in terms of the ion population, $x_{\rm i}$:

$$0 = \beta_{\rm dr} \left(\frac{m_{\rm e}}{m_{\rm i}} \right)^{1/2} \frac{n_{\rm H2} \tilde{J}_{\rm i}}{s_{\rm e} \tilde{J}_{\rm e}} x_{\rm i}^2 + \pi a_{\rm gr}^2 n_{\rm gr} \left(\frac{8kT}{\pi m_{\rm i}} \right)^{1/2} \tilde{J}_{\rm i} x_{\rm i} - \zeta \tag{4.16}$$

Assuming a value for our median charge state allows us to find values for $x_{\rm i}$ and $x_{\rm e}$ using Eqs. 4.16 and 4.15. We then check to see if those values are consistent with the net charge per volume being neutral (Eq. 4.12). By starting our $\langle Z \rangle$ guess at an arbitrarily high value, we can step down the median charge state until we reach a value that satisfies bulk disk charge neutrality. Upon fulfilling that condition we have estimates for $x_{\rm i}$ and $x_{\rm e}$ and a defined range of allowed grain charge states centered on $\langle Z \rangle$.

In step 2 of our ionization calculation we relax the restriction that all grains occupy the same charge state. We now consider $2N_q + 1$ states, where $N_q = 10$ in our code (by comparison, the ionization chemistry considered by Sano et al. (2000) had $N_q = 3$ and Ilgner & Nelson (2006) used $N_q = 2$). Returning to the pair of equations describing ion and electron equilibrium,

we now have $2N_q + 3$ unknowns: x_i, x_e, and the populations of the $2N_q + 1$ grain charge states. There are also more grain collision rates to calculate. When all grains have the same charge, it is sufficient to calculate 2 values of $J_n(Z)$, one for ions impacting grains and a second for electrons impacting grains. Since the collision rate is grain charge dependent, each of the equilibrium equations has $2N_q + 3$ terms. To simplify the calculation we can compute average values for $\tilde{J}_\mathrm{i}$, $\tilde{J}_\mathrm{e}$ and Z:

$$\left\langle \tilde{J}_\mathrm{i} \right\rangle = \sum_{q=1}^{2N_q+1} f_q \tilde{J}_\mathrm{i}(q) \tag{4.17}$$

$$\left\langle \tilde{J}_\mathrm{e} \right\rangle = \sum_{q=1}^{2N_q+1} f_n \tilde{J}_\mathrm{e}(q) \tag{4.18}$$

$$Z_\mathrm{avg} = \sum_{q=1}^{2N_q+1} f_q Z_q, \tag{4.19}$$

where f_q is the fractional population of grains in each charge state. This yields the following equilibrium equations for ions and free electrons:

$$\zeta = \beta_\mathrm{dr} n_\mathrm{H2} x_\mathrm{i} x_\mathrm{e} + \pi a_\mathrm{gr}^2 n_\mathrm{gr} \left(\frac{8kT}{\pi m_\mathrm{i}}\right)^{1/2} x_\mathrm{i} \left\langle \tilde{J}_\mathrm{i} \right\rangle \tag{4.20}$$

$$\zeta = \beta_\mathrm{dr} n_\mathrm{H2} x_\mathrm{i} x_\mathrm{e} + \pi a_\mathrm{gr}^2 n_\mathrm{gr} s_\mathrm{e} \left(\frac{8kT}{\pi m_\mathrm{e}}\right)^{1/2} x_\mathrm{e} \left\langle \tilde{J}_\mathrm{e} \right\rangle . \tag{4.21}$$

Similar what was done in step 1, we subtract Eq. 4.21 from Eq. 4.20 to yield a relation between x_i and x_e,

$$x_\mathrm{e} = x_\mathrm{i} \left(\frac{m_\mathrm{e}}{m_\mathrm{i}}\right)^{1/2} \frac{\left\langle \tilde{J}_\mathrm{i} \right\rangle}{s_\mathrm{e} \left\langle \tilde{J}_\mathrm{e} \right\rangle}, \tag{4.22}$$

giving us another quadratic equation when coupled with one of the equilibrium equations.

$$0 = \beta_\mathrm{dr} \left(\frac{m_\mathrm{e}}{m_\mathrm{i}}\right)^{1/2} \frac{n_\mathrm{H2} \left\langle \tilde{J}_\mathrm{i} \right\rangle}{s_\mathrm{e} \left\langle \tilde{J}_\mathrm{e} \right\rangle} x_\mathrm{i}^2 + \pi a_\mathrm{gr}^2 n_\mathrm{gr} \left(\frac{8kT}{\pi m_\mathrm{i}}\right)^{1/2} \left\langle \tilde{J}_\mathrm{i} \right\rangle x_\mathrm{i} - \zeta \tag{4.23}$$

The difference between step 1 and step 2 is that while in step 1 we were testing values of $\langle Z \rangle$, in this step we are testing the populations of the

$2N_q + 1$ grain charge states. Following the "detailed balance approximation" of Draine & Sutin (1987), we can calculate the values of f_q from the fractional gas populations $x_{\rm i}$ and $x_{\rm e}$. This approximation assumes that any two adjacent grain charge states are in equilibrium with each other. That is, the rate of ions sticking to grains with charge state $Z - 1$ is equal to the rate of electrons colliding and sticking to grains with charge state Z. This approximation is fundamentally incorrect for any scenario with more than 2 charge states; however, it serves as a useful tool to refine the ionization chemistry.

Since we obtained an estimate of $x_{\rm i}$ and $x_{\rm e}$ in step 1, we have an initial estimate for f_q. The goal is the same as in the previous step, to obtain populations that are consistent with each other and satisfy the bulk disk neutrality equation (Eq. 4.12). We define $r = x_i/x_e$ and use modifications to the ratio with the "detailed balance approximation" to produce f_q. We solve for r using a Newton-Raphson method: each iteration uses $r = r_0 + \epsilon$, where r_0 is the most recent solution's ratio, and ϵ is a small correction. After obtaining grain charge population f_q, $\left\langle \tilde{J}_{\rm i} \right\rangle$ and $\left\langle \tilde{J}_{\rm e} \right\rangle$, we solve Eq. 4.23 for $x_{\rm i}$ and use equation 4.15 to compute $x_{\rm e}$. We then test for charge neutrality. By measuring the effects of changing r by an amount ϵ, we can home in on a solution. This step yields values for x_i, x_e, and grain charge populations, f_q, for the $2N_q + 1$ charge states.

The third and final step adds refinement to the solution provided by step 2. The difference is that we now remove the detailed balance approximation. We begin with the gas population quantities $x_{\rm i}$ and $x_{\rm e}$, as well as the grain charge fractional populations f_q (we use the same grain charge grid as defined for step 2). There are a total of $2N_q + 3$ unknowns: $2N_q + 1$ possible net grain charges and non-neutral gas populations $x_{\rm i}$ and $x_{\rm e}$.

We therefore need to find $2N_q + 3$ equations to solve our chemistry network.

First, we assume that the population of each grain charge state is in equilibrium. Since charged particles in the gas can only have a charge of $q = \pm 1e$, only the immediate neighbors of each charge states need to be considered. If we're not considering grain charge states on the endpoints of our grid, then grains with charge $q = Ze$ can be produced by electrons colliding and sticking to grains in charge state $Z + 1$ or if ions collide and stick to a grain in charge state $Z - 1$. Likewise, grains in charge state Z can be lost by colliding with either electrons to produce a grain of charge $q = (Z - 1)e$ or with ion to create a grain in charge state $Z + 1$.

$$\left[J_{\rm i}(Z) + J_{\rm e}(Z)\right] n_{\rm gr} f_Z = J_{\rm i}(Z-1) n_{\rm gr} f_{Z-1} + J_{\rm e}(Z+1) n_{\rm gr} f_{Z+1} \tag{4.24}$$

Expanding the collision rates and removing common factors yields:

$$\left[\frac{x_{\rm i}}{\sqrt{m_{\rm i}}}\tilde{J}_{\rm i}(Z) + \frac{s_{\rm e} x_{\rm e}}{\sqrt{m_{\rm e}}}\tilde{J}_{\rm e}(Z)\right] f_Z = \frac{x_{\rm i}}{\sqrt{m_{\rm i}}}\tilde{J}_{\rm i}(Z-1) f_{Z-1} + \frac{s_{\rm e} x_{\rm e}}{\sqrt{m_{\rm e}}}\tilde{J}_{\rm e}(Z+1) f_{Z+1} \tag{4.25}$$

There are $(2N_q - 1)$ such equations (one for each grain charge state that is not an endpoint).

We also impose the ion and electron equilibrium equations presented earlier; the rate of ion (electron) production is equal to ion (electron) destruction. Taking Eq. 4.10 & 4.11 and substituting in expressions for J_n yields

$$\zeta = \beta_{\rm dr} n_{\rm H2} x_{\rm i} x_{\rm e} + \sum_Z \pi a_{\rm gr}^2 n_{\rm gr}(Z) \left(\frac{8kT}{\pi m_{\rm i}}\right)^{1/2} x_{\rm i} \tilde{J}_{\rm i}(T, Z) \tag{4.26}$$

$$\zeta = \beta_{\rm dr} n_{\rm H2} x_{\rm i} x_{\rm e} + \sum_Z \pi a_{\rm gr}^2 n_{\rm gr}(Z) s_{\rm e} \left(\frac{8kT}{\pi m_{\rm e}}\right)^{1/2} x_{\rm e} \tilde{J}_{\rm e}(T, Z), \tag{4.27}$$

Included as well is the condition that the disk be in sum electrically neutral (Eq. 4.12). The final equation for our system is conservation of grain

number. We assume that grains are neither created nor destroyed, they simply change charge states after collisions with electrons and ions:

$$\sum_{Z} f_Z = 1. \tag{4.28}$$

We now have a system of $(2N_q + 3)$ equations for $(2N_q + 3)$ unknowns and can solve the equations simultaneously using a Gauss-Jordan matrix inversion.

Figures 4.1 and 4.2 present results of this chemistry algorithm when tested on a parcel of disk material at temperature T, density ρ, composed of a well mixed population of dust grains of size, $a_{\rm gr}$, and gas molecules at a dust-to-gas mass ratio, ϕ. Ranges of typical disk temperatures ($20\,{\rm K} \leq T \leq 2000\,{\rm K}$) and densities ($10^{-20}\,{\rm g\,cm^{-3}} \leq \rho \leq 10^{-9}\,{\rm g\,cm^{-3}}$) are tested. An X-ray source, such as a protostar, is assumed to be 1 AU away and is radiating X-rays as calculated by Igea & Glassgold (1999) with $L_{\rm X} = 10^{29}\,{\rm erg\,s^{-1}}$. A single grain size of $a_{\rm gr} = 0.1\,\mu{\rm m}$ is used. A range of dust-to-gas ratios are tested, ranging between 10^{-4} and 10^{-1}.

Figure 4.1 shows the fraction of the gas that is ionized, x_i, over the range of parameters discussed above. As expected, the primary driver of x_i is the mass density of the material, lower densities lead to higher amounts of ionized gas. Temperature has a relatively minor effect on x_i. Regardless of the grain size or dust/gas ratio, x_i appears to reach a maximum value of $\sim 10^{-6}$ at the minimum tested density of $\rho = 10^{-20}\,{\rm g\,cm^{-2}}$. The minimum value of x_i (encountered at the largest density tested) ranges between $\sim 10^{-14}$ and $\sim 10^{-17}$, depending on $a_{\rm gr}$ and ϕ. Increasing the ratio (while holding grain size constant) makes the minimum ionization fraction decrease.

The electron fraction, x_e, is also presented in Figure 4.1. The trends are similar: x_e reaches its maximum value at the minimum density, and temperature plays little role. The maximum values of x_e are roughly uniform

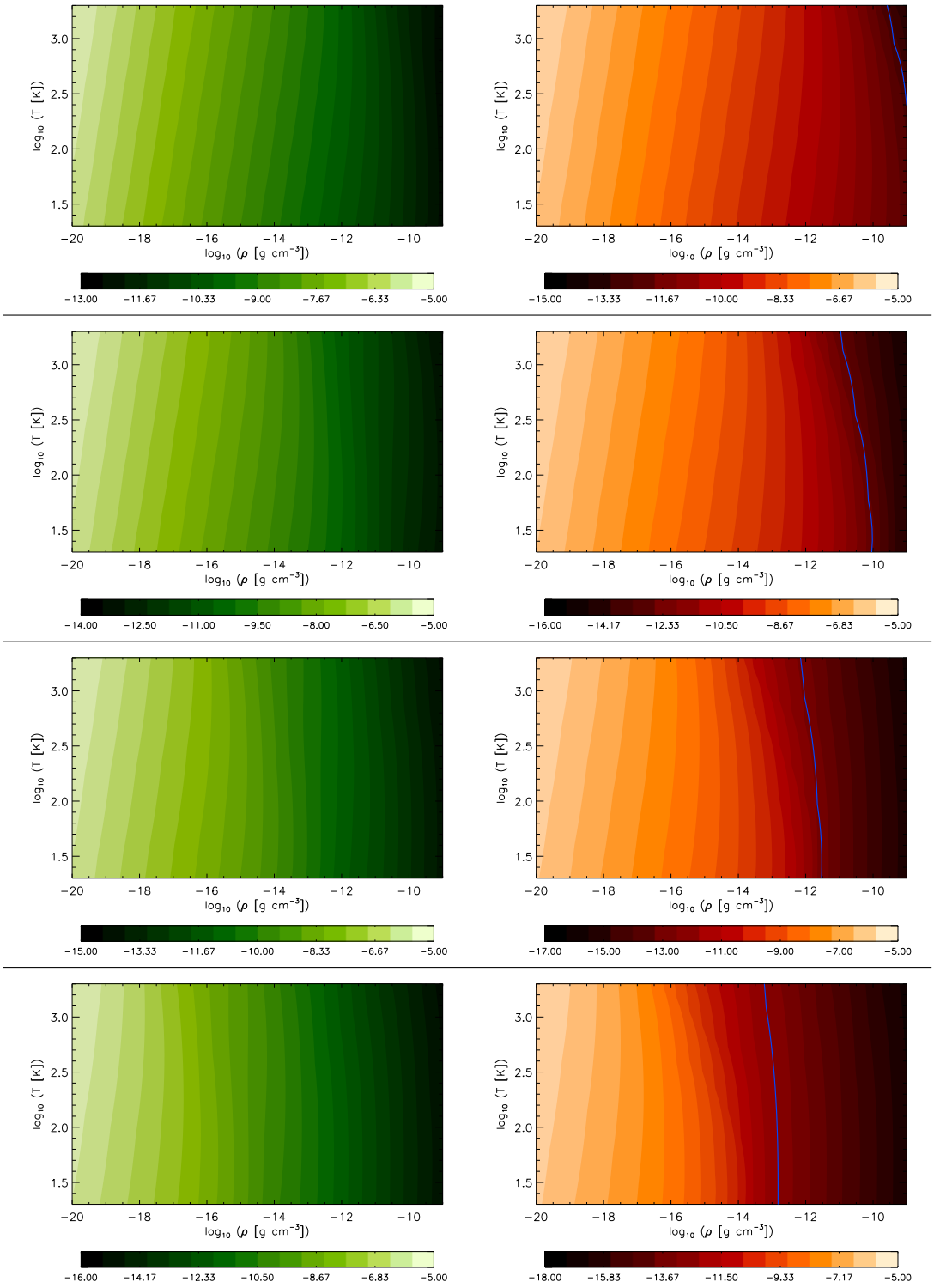

Figure 4.1: $x_i(\rho, T)$ (left column) and $x_e(\rho, T)$ (right column) presented logarithmically. Varied over the rows is dust to gas ratio ϕ. $\Sigma_{\rm a} = 10\,{\rm g\,cm^{-2}}$ and $a_{\rm gr} = 0.1\,\mu{\rm m}$. From top to bottom $\phi = 10^{-4}, 10^{-3}, 10^{-2}, 10^{-1}$. The blue line in the right column represents where $x_e = 10^{-13}$.

across all tested values of $a_{\rm gr}$ and ϕ. At these low densities, $x_e \sim 10^{-6}$ (i.e. the ratio of $x_i/x_e \approx 1.0$, there is an electron for every ion). As with x_i, the electron fraction found at the maximum value of density varies depending on the dust-to-gas ratio. Again, increasing the ratio causes the minimum electron fraction to drop. It is usually assumed that in order for a gas to be susceptible to the magnetic field, it needs $x_e \gtrsim 10^{-13}$ (Gammie 1996). A line designating this boundary is drawn in on all the x_e panes in Figure 4.1. Due to the effects of the dust-to-gas ratio on the minimum electron fraction, the range of densities allowing the gas to be coupled to the magnetic field changes significantly. The gas will be magnetically susceptible at densities up to and exceeding $10^{-10}\,{\rm g\,cm^{-3}}$ when $a_{\rm gr} = 0.1\,\mu$m and $\phi = 10^{-4}$. On the other end of the spectrum, if the grain size is 0.1 μm and $\phi = 10^{-1}$, only when $\rho \lesssim 10^{-14}\,{\rm g\,cm^{-3}}$ will the gas be allowed to couple to the magnetic field lines.

Figure 4.2 shows that the ratio of x_i/x_e varies between 1.0 and 70.0 for all values of ϕ tested. The transition between the two extrema occurs over a relatively small range of mass density. The location of this transition varies with ϕ. As the dust to gas ratio grows from 10^{-4} to 10^{-1}, the density at which the ratio transitions drops from $\rho \sim 10^{-9}$ to $10^{-13}\,{\rm g\,cm^{-3}}$. Finally, in Figure 4.2 we present the average charge per grain, represented by the unitless charge coefficient $Z_{\rm avg}$, where $q = Z_{\rm avg}e$. For all cases where $a_{\rm gr} = 0.1\,\mu$m, the range of $Z_{\rm avg}$ is -38 to 0. The most negatively charged grains are found at high temperatures. For the minimum dust-to-gas ratio tested of 0.0001, density only has an effect on $Z_{\rm avg}$ when $\rho \gtrsim 10^{-11}\,{\rm g\,cm^{-3}}$, the higher densities, and collision rates related to them, precluding electrons from sticking to the grains as often. As ϕ increases, the density range where large negative $Z_{\rm avg}$ is prevented grows. When $\phi = 0.001$, $\rho \gtrsim 10^{-14}\,{\rm g\,cm^{-3}}$ effects the magnitude of $Z_{\rm avg}$. At $\phi = 0.01$, $\rho \gtrsim 10^{-16.5}\,{\rm g\,cm^{-3}}$ have an effect

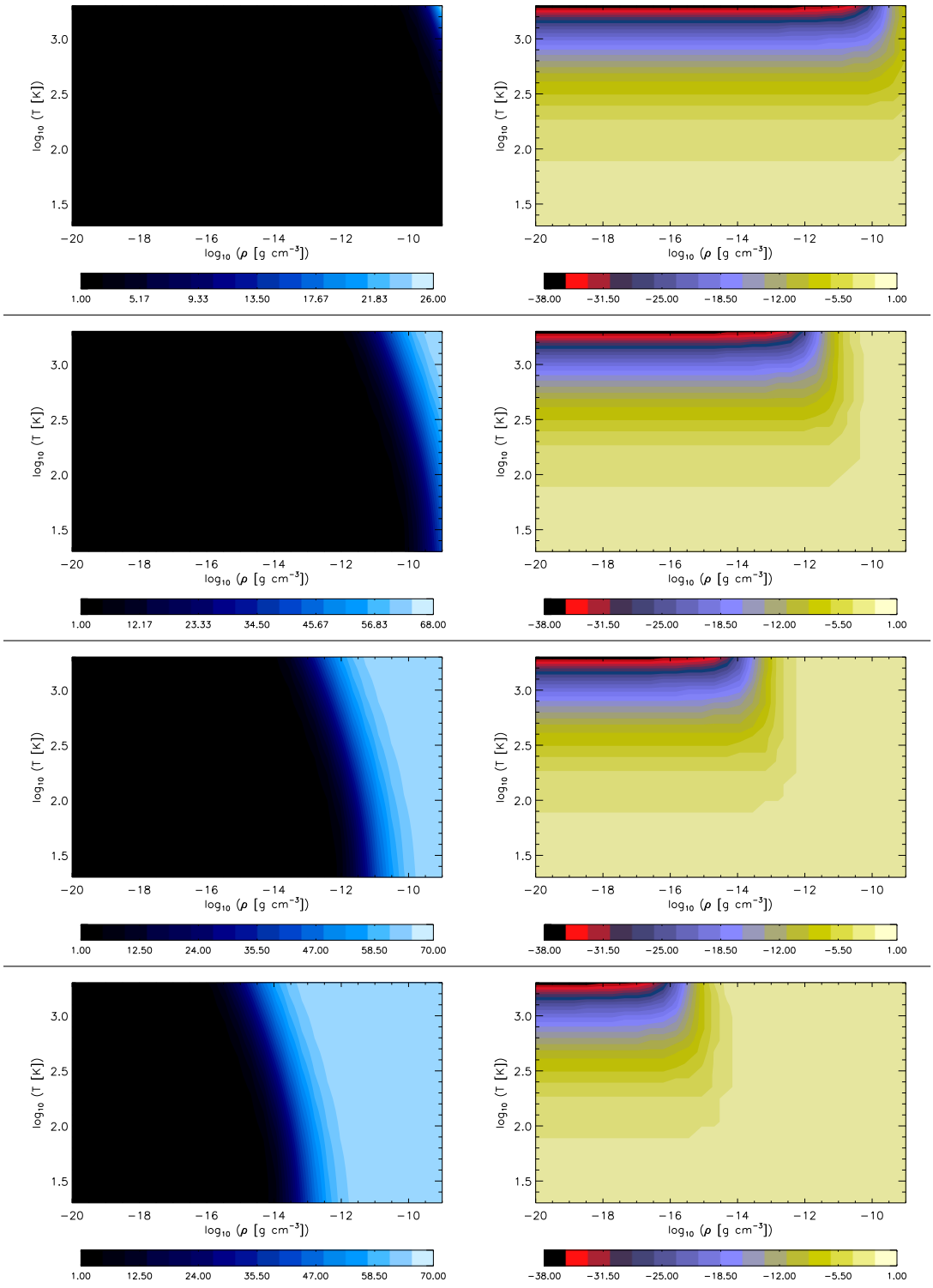

Figure 4.2: Ratio $x_i(\rho, T)/x_e(\rho, T)$ (left column) and $Z_{\rm avg}(\rho, T)$ (right column). Varied over the rows is the dust to gas ratio. $\Sigma_{\rm a} = 10\,{\rm g\,cm^{-2}}$ and $a_{\rm gr} = 0.1\,\mu{\rm m}$. From top to bottom $\phi = 10^{-4}, 10^{-3}, 10^{-2}, 10^{-1}$.

and at the largest ratio tested ($\phi = 0.1$) the critical density is $\rho = 10^{-19}\,\mathrm{g\,cm^{-3}}$.

This ratio x_e/x_i tells us where most of the charge in the disk is located. When $x_e \approx x_i$, the number of electrons and ions in the disk are near equal, and since we are assuming that each gas molecule can contribute one free electron to the gas, nearly all of the charge is in the form of free electrons and ions and the grains are mostly neutral. When $x_i/x_e \ll 1$, there are far more ions in the gas than electrons, implying that most electrons have been absorbed by the dust grains; this is where our grain calculations matter the most (i.e. $\rho > 10^{-12}\,\mathrm{g\,cm^{-3}}$). Similarly, situations where $Z_{\mathrm{avg}} \ll 0$ (i.e. $\rho < 10^{-15}\,\mathrm{g\,cm^{-3}}$) are where our chemistry method is most needed as our grain charge grid can be centered on any value, unlike previous models which center their grids on $Z_{\mathrm{avg}} = 0$. These two density criteria demonstrate that there is a large number of ρ and T combinations where our approach is potentially very important.

We also tested how changing the value of Σ_{a} (the active layer thickness) effected the ionization chemistry. Sano et al. (2000) suggests a maximum Σ_{a} of $\sim 10\,\mathrm{g\,cm^{-2}}$ and Gammie (1996) proposed values up to $\sim 100\,\mathrm{g\,cm^{-2}}$. We tested over the range of 0.1 to 100 $\mathrm{g\,cm^{-2}}$. For these tests we held $\phi = 0.01$ and $a_{\mathrm{gr}} = 0.1\,\mu\mathrm{m}$. Figure 4.3 illustrates the effects of Σ_{a} on x_i and x_e. Both fractional quantities decrease as Σ_{a} increases. This is due to the X-ray absorption volume being increased, lowering the effective ionization rate in the process. X-rays tend to dominate ionization in PPDs (Igea & Glassgold 1999), therefore a drop in the X-ray ionization rate will have a significant effect on the population of free electrons and ions in the gas. Unlike the effects of changing dust to gas ratio ϕ (the range in x_i and x_e growing with ϕ since only the minimum ionization and electron fractions

were effected), adjusting Σ_a effects both the minimum and maximum levels of ionization/electron fractions. As Σ_a increases from 0.1 to 100.0 g cm^{-2}, the maximum values of x_i and x_e decrease from $\sim 10^{-4}$ to $\sim 10^{-6}$. Over the same range in the active layer thickness, the minimum values of the ionization fraction change from $\sim 10^{-12}$ to $\sim 10^{-16}$ and the electron fraction varies from $\sim 10^{-14}$ to $\sim 10^{-18}$. The $x_e = 10^{-13}$ boundary shifts to lower mass densities as the active layer thickness increases (from $\sim 10^{-9}$ to $\sim 10^{-13}$).

In Figure 4.4 the effects of Σ_a on the x_i/x_e ratio and Z_{avg} are presented. The same two-tiered contour of x_i/x_e is shown. As the active layer thickness is increased, the density at which the transition from unity to $\approx$70 occurs at a density ranging from $\sim 10^{-9}$ (when $\Sigma_a = 0.1$ g cm^{-3}) to $\sim 10^{-12.5}$ (for $\Sigma_a = 100$ g cm^{-3}). Increasing the active layer thickness produces similar effects to increasing the dust-to-gas ratio. As for Z_{avg}, a similar range of average grain charge is found over the tested range in Σ_a (-38 to 0).

We present some grain charge state population results. Figure 4.5 presents the fractional population of each grain charge state considered in our model ($Z_{avg} - 10 \leq Z \leq Z_{avg} + 10$). In general, the population of a charge state outside of $(Z_{avg} - 1) < Z < (Z_{avg} + 1)$ grows as temperature increases. The previously used ionization models discussed above used a limited number of allowed grain charges (5 or 7 total). As shown here, such a model may be appropriate so long as temperatures are relatively low. As temperature increases, not only does the population of charge states further from the average grain charge increase, but as seen in Figures 4.2 and 4.4 the average grain charge deviates from neutrality.

To better illustrate this point, Figure 4.6 shows the resulting sum of various ranges of charge states. The disk environment modeled here has $\phi = 0.01$, $a_{gr} = 0.1\,\mu$m, $\Sigma_a = 10$ g cm^{-2}, and $\rho = 4.9 \times 10^{-15}$ g cm^{-3}. Whether

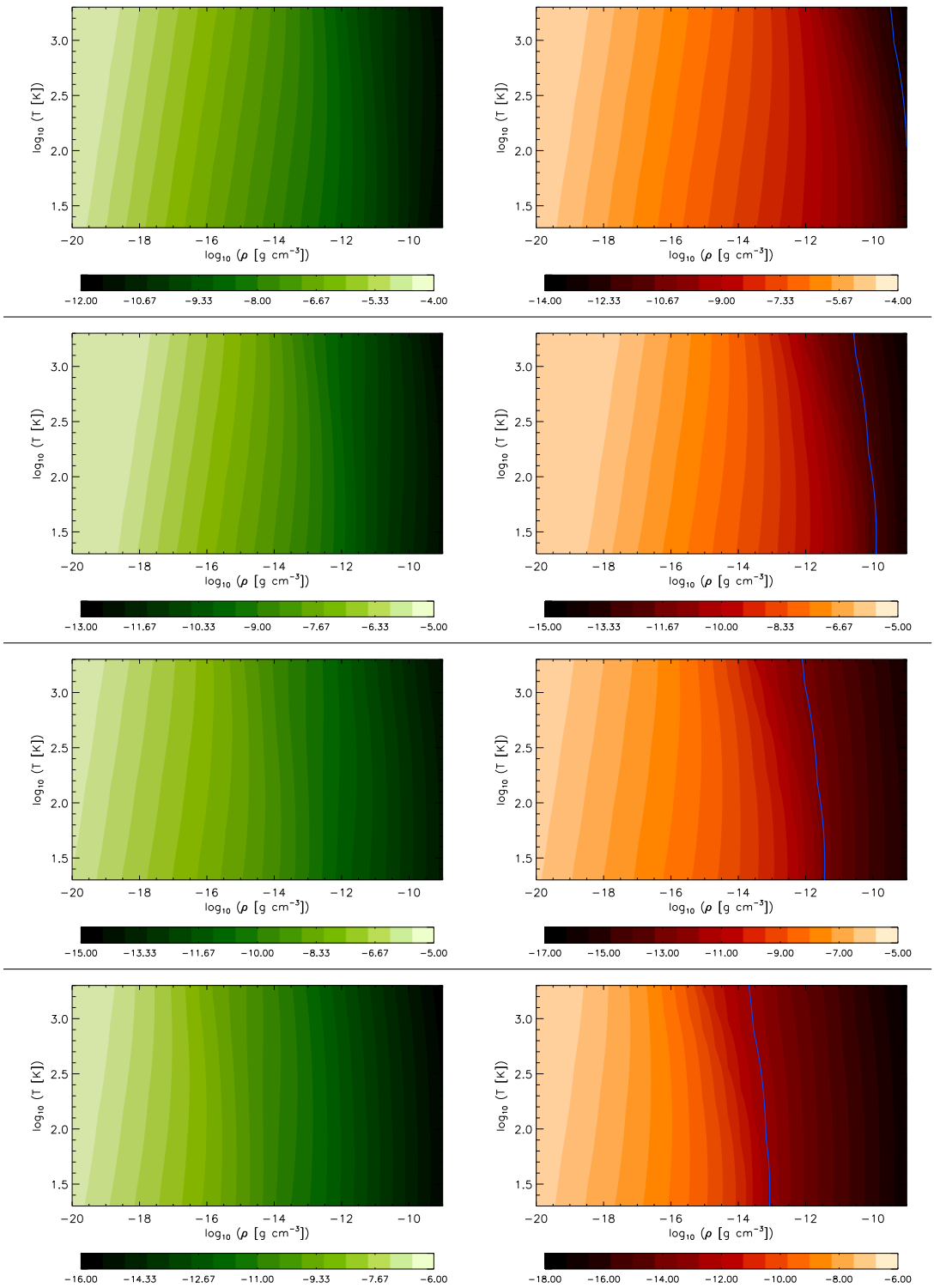

Figure 4.3: $x_i(\rho, T)$ (left column) and $x_e(\rho, T)$ (right column) presented logarithmically. Varied over the rows is Σ_a, ϕ is held at 0.01 and $a_\mathrm{gr} = 0.1\,\mu$m. From top to bottom $\Sigma_\mathrm{a} = 0.1$, 1.0, 10.0, 100.0 g cm^{-2}. The blue line in the right column represents where $x_e = 10^{-13}$.

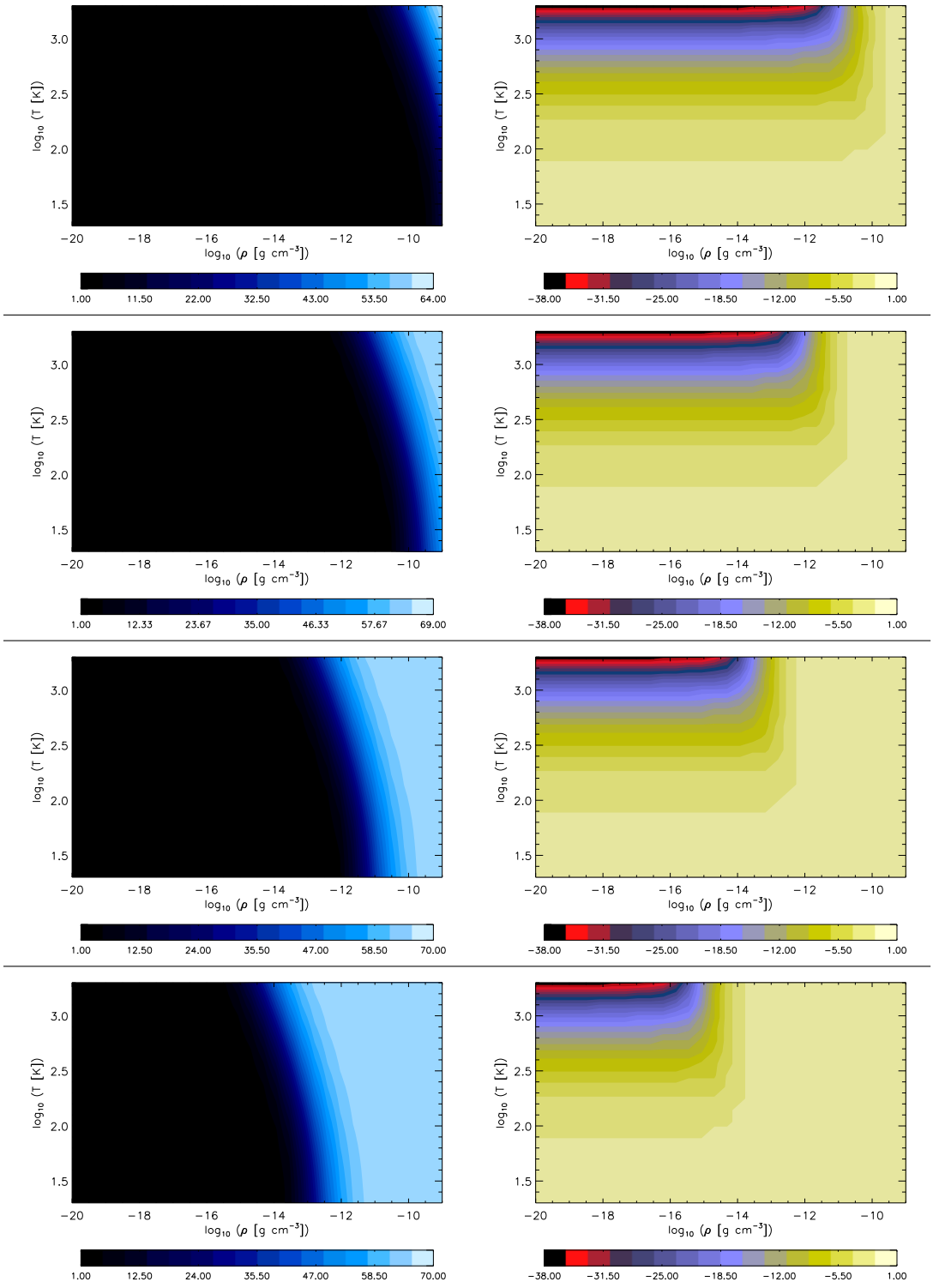

Figure 4.4: Ratio $x_i(\rho, T)/x_e(\rho, T)$ (left column) and $Z_{\rm avg}(\rho, T)$ (right column). Varied over the rows is $\Sigma_{\rm a}$, ϕ is held at 0.01 and $a_{\rm gr} = 0.1\,\mu$m. From top to bottom $\Sigma_{\rm a} = 0.1$, 1.0, 10.0, 100.0 g cm^{-2}.

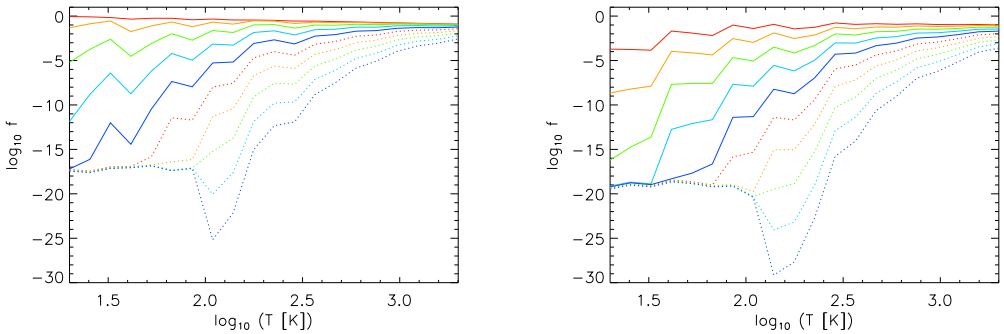

Figure 4.5: Fractional grain charge population, $f_q(T)$ for a mixed gas/dust system with $\rho = 4.9 \times 10^{-15}\,\mathrm{g\,cm^{-3}}$, $a_{\mathrm{gr}} = 0.1\,\mu\mathrm{m}$, $\phi = 0.01$, and $\Sigma_{\mathrm{a}} = 10\,\mathrm{g\,cm^{-2}}$. A total of 20 charge states (listed as departure from average charge) are presented between left and right frames. Left: -1 (solid red), -2 (solid orange), -3 (solid green), -4 (solid cyan), -5 (solid blue), -6 (dotted red), -7 (dotted orange), -8 (dotted green), -9 (dotted cyan), -10 (dotted blue). Right: +1 (solid red), +2 (solid orange), +3 (solid green), +4 (solid cyan), +5 (solid blue), +6 (dotted red), +7 (dotted orange), +8 (dotted green), +9 (dotted cyan), +10 (dotted blue).

or not a narrower range of charge states would neglect a appreciable amount of dust grains depends on the local temperature of the disk. For lower temperatures ($T < 80\,\mathrm{K}$), using a range of 5 charge states is appropriate. Temperatures up to 160 K can be represented by 7 charge states. However, as seen in Chapter 3, temperatures in the active regions of disks can be as high as $\approx$400 K for annuli inside of 1 AU in a disk with $\dot{M} = 10^{-8}\,\mathrm{M_\odot\,yr^{-1}}$ and $\Sigma_{\mathrm{a}} = 10\,\mathrm{g\,cm^{-2}}$. Therefore, in order to model the ionization of PPD active layers a higher number of charge states is necessary at higher temperatures. The consequence of not including enough charge states is that grain's net charges may not be allowed to go negative enough. Put another way, in the example illustrated in Figure 4.6, at $T = 100\,\mathrm{K}$ only 80% of the grains are within $Z = 2e$ of the median charge. Previous models with only 5 charge states would have the remaining 20% of the grains erroneously set to $Z = \pm 2e$ when they should be further from the median. Since the charge of the grains affects the collision rates, that means that the solution to all

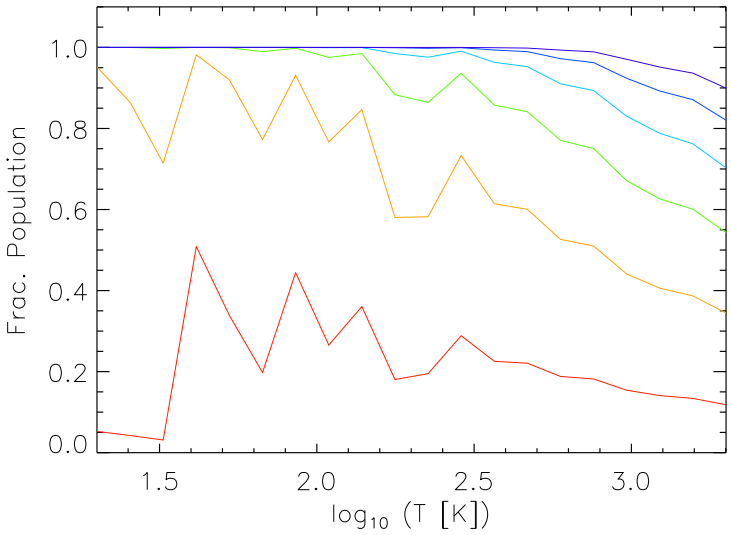

Figure 4.6: Fraction of dust grains included by summing $f_q(Z_{\rm avg})$ with $2n$ neighboring charge states (n on each side). Several sums are shown: $n = 0$ (red), $n = 1$ (orange), $n = 2$ (green), $n = 3$ (cyan), $n = 4$ (blue), and $n = 5$ (purple).

components of the ionization chemistry are incorrect.

Finally, we conducted a test to determine the quantitative effects of using a reduced range of allowed grain charge states, specifically the changes to electron density. Figure 4.7 presents the complete results of our test. We used the same values of ρ, Σ_a, $a_{\rm gr}$, and ϕ as the previous test. If we shrink the grid to a span of 7 charge states(but still allowing the grid to be centered on non-zero grain charge) x_e differs by as much as 5% at temperatures $\gtrsim 500\,{\rm K}$. Shrinking the allowed range of grain charges to 5 causes differences over 1% to appear at temperatures $\gtrsim 150\,{\rm K}$. However, if we shrink the range of charge states and anchor the range's center at $Z = 0$, then significant differences can appear at low temperatures. With 7 states between $Z = -3$ and $Z = +3$, x_e differs by 8% from our model at $T = 100\,{\rm K}$. With 5 states between $Z = -2$ and $Z = +2$ the difference in x_e at 100 K is 37%. The differences become more extreme as T is increased further. Whereas in the

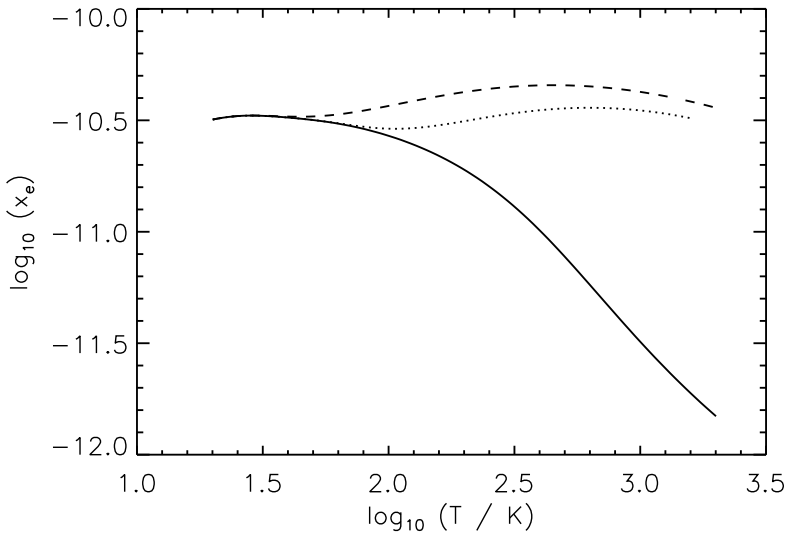

Figure 4.7: Electron density, $x_e(T)$ for three different treatments of grains within the chemistry model. The solid line is our grid of 21 allowed charge states. The dotted line is for a grid of 7 states centered on $Z = 0$, the dashed line is for a grid of 5 states centered on $Z = 0$.

narrower grids x_e remains at $\sim 10^{-10.5}$ over the range of temperatures tested, our model produces a $x_e(T)$ profile that falls off as $\sim r^{-1}$ at $T \gtrsim 300\,\mathrm{K}$. This demonstrates the necessity of a range of charge states that does not have the inflexibility of a grid centered on a net charge of 0.

Chapter 5

LAYERED ACCRETION INCLUDING TEMPERATURE FEEDBACKS

In Chapter 1 we discussed how the magnetorotational instability has been determined to be the most likely source of the turbulence responsible for transporting angular momentum within the disk. Other transport mechanisms, such as convection or gravitational instabilities, may play a role over short timescales compared to the lifetime of a PPD but are unlikely to be present consistently over a PPD's life. In Chapter 3 we presented the results of models which assumed a value for the turbulent viscosity parameter, α ($\nu = \alpha c_{\rm s} H$) as well as a thickness of the active layer, $\Sigma_{\rm a}$. In Chapter 4 we outlined how $\Sigma_{\rm a}$ can be calculated by computing the ionization chemistry of the disk. We will now combine that with the temperature code from Chapter 2 and an MRI algorithm (described below) to generate a suite of PPD models under the effects of the MRI. The goal is to calculate the disks' temperature structures with the constraint on $\Sigma_{\rm a}$ now lifted. Not only will $\Sigma_{\rm a}$ not be imposed, but a non-uniform value of layer thickness will be allowed. This in turn will permit the calculation of $\dot{M}_r(r)$ and $\dot{\Sigma}(r)$ at all radii in the disk. This will allow us to see in each annulus whether mass is accumulating or evacuating. Finally, we compute the timescales over which the annuli will evolve, the "short-term" end result being either a completely evacuated annulus or an annulus dense enough to trigger a gravitational instability.

5.1 Algorithm for determining MRI instability

Calculating the effects of the magnetic field on the disk involves a knowledge of the temperature, mass density, and magnetic field strength in the active layer. Using the algorithm described in Chapter 2 we ascertain the active

layer temperature, T_0, and the active layer density, ρ_0. We adopt a value for the magnetic field in the active layer, B_0.

Three sources of ionization are considered here. Cosmic rays, the rate given by $\zeta_{\rm cr}$, protostellar X-Rays, $\zeta_{\rm x}$, and radioactivity of unstable nucleotides within the disk, $\zeta_{\rm ra}$. For $\zeta_{\rm ra}$ we assume that the population of unstable radionucleotides within the disk is dominated by Al-26. We therefore set $\zeta_{\rm ra} = 10^{-19}\,{\rm s}^{-1}$. The rate of protostellar X-Rays has been investigated by Glassgold et al. (1997) and we set $\zeta_{\rm x} \sim 10^{-13}\,{\rm s}^{-1}$ with a protostellar X-Ray luminosity value of $L_{\rm x} = 10^{29}$. Finally, we adopt the cosmic ray ionization rates of Umebayashi & Nakano (1981) and use $\zeta_{\rm cr} = 10^{-17}\,{\rm s}^{-1}$. We combine these ionization rates to obtain an overall rate of ionization,

$$\zeta = \zeta_{\rm x} + \zeta_{\rm cr} + \zeta_{\rm ra}. \tag{5.1}$$

The question of MRI instability is answered in the following fashion. We run our temperature code to obtain temperature and density values at all locations within the disk. We then set the active layer column density, $\Sigma_{\rm a}$ to our minimum considered value of $0.1\,{\rm g\,cm}^{-2}$ (larger values will be considered as the code iterates). With known ρ_0, T_0, B_0, and $\Sigma_{\rm a}$ we compute the ionization state, or chemistry, of the disk (as described in the previous section). At this point the temperature is not yet self-consistent with $\Sigma_{\rm a}$, instead T_0 and $\Sigma_{\rm a}$ are fixed separately. They will be made self-consistent with each other soon.

We then obtain an average charge per grain value via

$$Z_{\rm avg} = \sum_{i=-NQ}^{NQ} f_i Z_i, \tag{5.2}$$

where f_i is the fraction of grains with charge $Z_i e$. Three timescales need to be calculated: interaction of electrons with neutrals, τ_{en}, interaction of ions

with neutrals, τ_{in}, and the interaction of grains with neutrals. They are calculated using the following equation (Mouschovias 1996):

$$\tau_{sn} = \frac{1}{a_{s\mathrm{He}}} \frac{m_s + m_{\mathrm{H_2}}}{m_{\mathrm{H_2}}} \frac{1}{n_{\mathrm{H_2}} \left\langle \sigma_{\mathrm{coll}} w \right\rangle_{s\mathrm{H_2}}}. \tag{5.3}$$

Here, $m_{\mathrm{H_2}}$ is the mass of the dominant neutral gas particle in the disk, molecular hydrogen and m_s is the mass of the species the timescale is being computed for (either electrons, hydrogen ions, or grains). The value $a_{s\mathrm{He}}$ is a scaling factor to take into account collisions with helium atoms, it has different values depending on what s is (1.14 for ions, 1.16 for electrons, and 1.28 for dust grains). Finally where c_s is the isothermal sound speed of the disk and $n_{\mathrm{H_2}}$ is the number density of H_2 molecules.

The next step is to compute the conductivities of the electrons (σ_e), ions (σ_i), and the grains (σ_{gr}). We do this via

$$\begin{aligned} \sigma_e &= \frac{n_e e^2 \tau_{en}}{m_e} \\ \sigma_i &= \frac{n_i e^2 \tau_{in}}{m_i} \\ \sigma_{gr,j} &= f_j Z_j^2 \frac{n_{gr} e^2 \tau_{gn}}{m_{gr}}. \end{aligned}$$

With these conductivities for the different species the conductivities relevant to computing the diffusion coefficients can be found using the following equations:

$$\sigma_{\parallel} = 10^{-30} + \sigma_e + \sigma_i + \sum_{j=-NQ}^{+NQ} \sigma_{gr,j} \tag{5.4}$$

$$\sigma_{\perp} = \frac{\sigma_e}{1 + (\omega_e \tau_{en})^2} + \frac{\sigma_i}{1 + (\omega_i \tau_{in})^2} + \sum_{j=-NQ}^{+NQ} \frac{\sigma_{gr,j}}{1 + (\omega_{g,j} \tau_{gn,j})^2} \tag{5.5}$$

$$\sigma_{\mathrm{H}} = \frac{\sigma_e \omega_e \tau_{en}}{1 + (\omega_e \tau_{en})^2} + \frac{\sigma_i \omega_i \tau_{in}}{1 + (\omega_i \tau_{in})^2} + \sum_{j=-NQ}^{+NQ} \frac{\sigma_{gr,j} \omega_{g,j} \tau_{gn,j}}{1 + (\omega_{g,j} \tau_{gn,j})^2}, \tag{5.6}$$

where $\omega_a = q_a B_0 / (m_a c)$ is the gyroscopic frequency of species a.

With the appropriate coefficients now defined, the diffusion coefficients can now be calculated using Equation 4.5. Using the computed diffusion coefficients we can finally use Eq. 4.1 to determine whether or not the disk is stable to the MRI. The only unknown remaining is s, which will have a value of ± 1 depending on whether the Alfven wave is aligned or anti-aligned with the magnetic field. We will test both values of s and if either value yields the unstable condition we deem the disk to be unstable to the MRI.

In Chapters 2 and 3 we explored the various feedbacks present in calculating the temperature structure of a PPD. Now instead of imposing an arbitrary value for the active layer column density, $\Sigma_{\rm a}$, we wish to solve for the value of $\Sigma_{\rm a}$ appropriate for a disk where the MRI is responsible for angular momentum exchange. This introduces an additional feedback as it was demonstrated in that paper that changing $\Sigma_{\rm a}$ can have drastic effects on the temperature structure, particularly at the midplane. Therefore, after the values of $\Sigma_{\rm a}$ are updated, the temperature structure of the disk needs to be recomputed.

Our algorithm is as follows. We first calculate the disk temperatures using a starter value of $\Sigma_{\rm a} = 0.1\,{\rm g\,cm^{-3}}$. After converging to a solution for $T(r,z)$ we perform the above calculations in each annulus to determine whether or not that area of the disk is stable to the MRI. If unstable, $\Sigma_{\rm a}$ is increased for that annulus. The disk temperature structure is then recomputed with the updated active layer. The process iterates until a value of $\Sigma_{\rm a}$ is found that is stable against the MRI, or until $\Sigma_{\rm a} = \Sigma/2$ (i.e. the whole disk is active).

Our computational grid has the same setup as in chapters 2 and 3. The disk is logarithmically divided into into $N_r = 50$ annuli. Each annulus has N_z evenly spaced vertical grid points; the value of N_z varies between

annuli but is always between 80 and 120.

5.2 Disk Evolution

The models which will be presented in this chapter are essentially snapshots in time of a protoplanetary disk. However, based on our results we will be able to compute some basic evolution timescales for the disk. In this section the terms and equations will be introduced and discussed. While these calculations will be basic and from first principles, they still offer insight toward our understanding of the disk's evolution because observations capable of measuring the mass flow through the disk (and not the mass flow from the disk onto the protostar) are still not possible (see Chapter 1).

The first quantity we wish to pursue is the mass flow through the disk, $\dot{M}$. In terms of known $\Sigma_{\rm a}$ and viscosity, ν, $\dot{M}_r(r)$ can be calculated using the following equation:

$$\dot{M}_r(r) = 6\pi r^{1/2} \frac{\partial}{\partial r} \left(r^{1/2} \nu \Sigma_{\rm a} \right). \tag{5.7}$$

Recall that in our models we are implementing an α-viscosity of the type introduced by Shakura & Sunyaev (1973), where $\nu = \alpha c_{\rm s}^2 \Omega^{-1}$ is the local viscosity as defined by the Keplerian frequency and the local sound speed. Using an isothermal soundspeed, $c_{\rm s} = kT_{\rm mid}/\bar{m}$, allows us to incorporate the midplane temperatures presented in the previous section into the calculation. $\Sigma_{\rm a}$ is of course the active layer thickness also found self-consistently found in our models. In Eq. 5.7, a positive value of $\dot{M}$ denotes mass moving toward the central protostar, a negative value equates to mass moving away from the star.

Another way of analyzing how mass flows through the disk is to compute the rate of mass gain or loss by an annulus rather than the mass flow per unit volume just discussed. The advantage of such a calculation is

that since the annuli are concentric rings, a better idea of how the disk would evolve from that snapshot in time can be ascertained. With $\dot{M}_r$ defined by Eq. 5.7, we can compute $\dot{\Sigma}$, the mass gained or lost per time by an annulus:

$$\dot{\Sigma}(r) = \frac{1}{2\pi r}\frac{\partial \dot{M}_r}{\partial r}. \tag{5.8}$$

For $\dot{\Sigma}$, the meaning of the sign is much more straightforward. A negative value of $\dot{\Sigma}$ indicates that the annulus is losing mass, a positive value means mass is accruing. In computing $\dot{\Sigma}(r)$ for the disks, one adjustment will be made to $\dot{M}$. To take into account smoothing in the mass flow over short timescales, if an annulus is surrounded on both sides by annuli with $\dot{M}$ in the same direction (i.e. three consecutive positive points or three consecutive negative points), its value will be replaced by the average of itself and its neighbors. No adjustments are made to $\dot{M}$ values where at least one of its neighbors is of the opposite sign. Due to the presence of the differentiation over radius, we cannot evaluate $\dot{\Sigma}$ at the disk boundaries.

With computed mass flow rates through the disk, we can now calculate the timescales over which annuli will either completely evacuate or become gravitationally unstable, whichever is appropriate for the individual annulus. For annuli that are accruing material, we will use the Toomre parameter, Q, that was introduced in Chapter 1 to define a critical mass density which will serve as an endpoint to the timescale calculated.

First we will consider the evacuation timescale, τ_{evac}. We define this quantity to be how long it will take an annulus to drain all of its mass given the $\dot{\Sigma}$ calculated from the previous section. Assuming this rate of mass loss is constant over time and with known $\dot{\Sigma}(r)$, we can easily calculate it via

$$\tau_{\text{evac}} = \frac{\Sigma}{|\dot{\Sigma}|}. \tag{5.9}$$

The other relevant timescale for our discussion, which represents how much time an annulus would take to become gravitationally unstable we will call the GI timescale, $\tau_{\rm GI}$. We define it such that it measures how much time is needed for an accreting portion of the disk to reach the surface density which makes the Toomre parameter less than unity (i.e. gravitationally unstable). As was introduced in Chapter 1, the Toomre parameter is defined as:

$$Q = \frac{c_{\rm s}\Omega}{\pi G\Sigma}, \tag{5.10}$$

where $c_{\rm s} = kT_{\rm mid}/\bar{m}$ is the isothermal sound speed and Ω is the Keplerian orbital frequency. If Q is evaluated to be < 1, then that portion of the disk is gravitationally unstable. Therefore, we define $\Sigma_{\rm crit}$ as the surface density of a disk's annulus where $Q = 1$ (based on the calculated midplane temperature value). This yields the following definition for our critical surface density:

$$\Sigma_{\rm crit} = \frac{c_{\rm s}\Omega}{\pi G}, \tag{5.11}$$

where $c_{\rm s}$ is the local isothermal sound speed, Ω the Keplerian frequency of the annulus, and G the gravitational constant. Since $c_{\rm s}$ is defined with the midplane temperature, $T_{\rm mid} \propto r^{q}$ (leading to $c_{\rm s} \propto r^{q/2}$) and $\Omega \propto r^{-3/2}$, the critical surface density varies as $\Sigma_{\rm crit} \propto r^{-1.8}$ (where we have adopted $q = 0.6$ as was done in the previous section).

We can now calculate the GI timescale in terms of the disk's properties:

$$\tau_{\rm GI} = \frac{(\Sigma_{\rm crit} - \Sigma)}{|\dot{\Sigma}|} = \frac{1}{|\dot{\Sigma}|}\left(\left[\frac{kT_{\rm mid}M_{\star}}{\pi^2\bar{m}Gr^3}\right]^{1/2} - \Sigma\right), \tag{5.12}$$

where $M_{\star}$ the mass of the central protostar, $\bar{m}$ is the average molecular mass of the disk material, and k is the Boltzmann constant.

5.3 Model Results

A number of disk models were generated to test the extent of the MRI. The protostar used was the same as that of the layered accretion models in Chapter 3 ($M = 0.5\,\mathrm{M}_\odot$, $R = 2.5\,\mathrm{R}_\odot$, $T = 4000\,\mathrm{K}$). Also as before, we will be generating snapshot models of how the disk is behaving at a specific time and will not be time evolving the disk. As such, we choose again a relatively simple disk surface density profile, $\Sigma(r) \propto r^{-n}$. In Chapter 3, we used $n = 1.5$ for testing the layered accretion models. For testing the MRI, we will again employ that profile and will introduce a second, piecewise surface density as well. We will describe our adopted surface density profiles more extensively below.

In all models tested we take the average particle mass to be $\bar{m} = 2.3 m_\mathrm{p}$. The gas to dust ratio (unless otherwise indicated) is 0.01 and we assume a well-mixed disk where the dust grains are silicates with opacities given by Draine & Lee (1984). We are again simulating a population of grains that are all one size, in this case $a_\mathrm{gr} = 0.1\,\mu\mathrm{m}$.

Our model imposes a simple magnetic field on the disk. We assume a spatially and temporally constant field strength and direction. The field is aligned with the the disk's rotation axis ($\mathbf{B} = B\hat{\mathbf{e}}_z$). We test a variety of field strengths, with B ranging between 10^{-6} and 10 Gauss. Employing a spatially uniform field may not be physically accurate, however, since we are testing a range of magnetic field strengths and are not at this point time evolving the field, it serves as a useful avenue to pursue a parameter study of B.

As stated above, we will test two surface density profiles. The first one we present is a relatively low mass disk and will be similar to that used

in our layered accretion models. We define $\Sigma(r)$ as:

$$\Sigma(r) = 1700 \left(\frac{r}{1\,\mathrm{AU}}\right)^{-3/2} \mathrm{g\,cm^{-2}}. \tag{5.13}$$

The second profile being tested is of a much higher total mass. It is a piecewise function:

$$\Sigma(r) = \begin{cases} 22470 \left(\frac{r}{1\,\mathrm{AU}}\right)^{-1} \mathrm{g\,cm^{-2}} & \text{if } r \leq 2\,\mathrm{AU} \\ 343 \left(\frac{r}{10\,\mathrm{AU}}\right)^{-2.168} \mathrm{g\,cm^{-2}} & \text{if } r > 2\,\mathrm{AU}. \end{cases} \tag{5.14}$$

Equation 5.13 is a density profile commonly used when modeling PPDs. This is in accordance with the so-called minimum mass solar nebula as computed in Hayashi (1981). Integrating the disk's mass out to $r_{\mathrm{max}} = 100\,\mathrm{AU}$ (the extent of our disk in the models), $M_{\mathrm{disk}} = 0.023\mathrm{M}_{\odot}$. It is more massive than the profile used in Chapter 3, in which we had set $\Sigma(1\,\mathrm{AU}) = 1000\,\mathrm{g\,cm^{-2}}$. The other profile we are testing, Eq. 5.14 is of much higher mass. This high mass disk features a slightly more complicated surface density structure. It is a piecewise combination of two power laws, with their joining at $r = 2.0\,\mathrm{AU}$. This density function was suggested in Desch (2007) where a revised mass value was calculated for the solar nebula, the precursor to our solar system. The integrated disk mass out to 100 AU is $0.121\,\mathrm{M}_{\odot}$, almost an order of magnitude higher than our low mass disk.

The strength of the turbulence is still measured by dimensionless parameter α such that the viscosity is defined as $\nu = \alpha c_{\mathrm{s}}^2 \Omega^{-1}$. Currently, there is no one appropriate value of α in the active layer; various values have been found via numerical simulations and observational fitting. For example, Winters et al. (2003) uses an average global value of $\alpha = 0.02$ in MHD simulations of a fully ionized ionized area of a disk undergoing planet formation. Nelson (2005) uses a volume-average value of $\alpha = 0.005$ in another protoplanetary model of protoplanets interacting with turbulent,

magnetized protostellar disks. However, there is observational evidence for global α values of 0.001-0.003 in PPDs based on observations of FU Ori systems (King et al. 2007). Therefore, it is important that we test a range of α. With our model constructed with layered accretion, we do not impose a global value for α but rather an active-layer value. If a dead zone $\alpha_{\rm dz} = 0$ is imposed the active layer value, $\alpha_{\rm a}$, can be related to its vertically averaged value, α, by $\alpha_{\rm a} = \alpha(\Sigma_{\rm a}/\Sigma)$ as discussed previously. We test 4 different values for $\alpha_{\rm a}$: 0.01, 0.03, 0.1, and 0.3 and impose a dead zone value of $\alpha_{\rm dz} = 0$.

We also test a range of magnetic field strengths. Currently there is not a well defined B-field value in the active regions of PPDs. However, there is a range of strengths that would be appropriate to consider. Measurements of paleofields in meteorites are thought to probe the magnetic field of the solar nebula. These measurements indicate magnetic field strengths $B \approx 0.1 - 1\,{\rm G}$ (Weiss et al. 2008). The source of this magnetic field is not known. It is not likely to be from the protostar, though, as the stellar dipole field will vary as $B \sim 10^3\,(r/R_\odot)^{-3}\,{\rm G}$ and will be $< 1\,\mu{\rm G}$ at 1 AU. More likely it is caused by the magnetic turbulence within the disk itself (akin to a magnetic dynamo). As discussed in Chapter 1, Goodman & Xu (1994) have explored the possibility of parasitic instabilities effecting the strength of the magnetic field in active regions of PPDs and found that it is possible for weak fields to strengthen to the level of equipartition, $B_{\rm eq} = 20(r/1\,{\rm AU})^{-3}\,{\rm G}$. However, it is also likely that magnetic field growth will be suppressed before equipartition field strength is attained (Goodman & Xu 1994). We will impose a variety of field strengths on the active layers of the disk, ranging between $B = 10^{-6}$ and $10\,{\rm G}$. In all cases the magnetic field is oriented parallel to the disk's rotation axis and is spatially uniform.

As with the models presented in Chapter 3, each simulation builds

upon a provided starter solution to save time. A passive disk was generated for each surface density profile tested. For each value of α used, a series of models were generated with progressively increasing B-field strengths, with each model using the solution with a weaker magnetic field as a starter solution. On our 2 GHz machine, the runtimes varied from 30 minutes for weaker B-fields to as long as 10 hours for stronger fields.

What follows is the results of our parameter study of α and B. First we will present the resulting active layer thicknesses, $\Sigma_{\rm a}$ which are no longer arbitrarily chosen but are self-consistently calculated using the ionization chemistry described in Chapter 4. We then show the resulting midplane temperature structures of the model disks. The calculated mass flow rates $\dot{M}$ and $\dot{\Sigma}$ are then shown, along with a timescale calculation for either an annulus' evacuation or gravitational instability trigger, whichever is appropriate.

5.4 Active Layer Thicknesses

The resulting $\Sigma_{\rm a}$ are presented in Figures 5.1 and 5.2 for the low mass disk described by Eq. 5.13. The data have not been smoothed in any way. The small fluctuations seen are mostly likely due to small numerical inaccuracies caused by the limited number of radial grid points. These feed back into the flaring angle and so can lead to difficulties in convergence of the temperature profile, along the lines of the unstable modes identified in the Appendix of Chiang et al. (2001).

First of all, we notice that for this range of magnetic fields, the value of $\alpha_{\rm a}$ has little effect on $\Sigma_{\rm a}$ when varied between 0.01 and 0.3. This is not overly surprising, as the resulting $\Sigma_{\rm a}$ are all $\lesssim 10\,{\rm g\,cm^{-2}}$ and as was demonstrated in Chapter 3, changing $\alpha_{\rm a}$ when the active layer thickness is

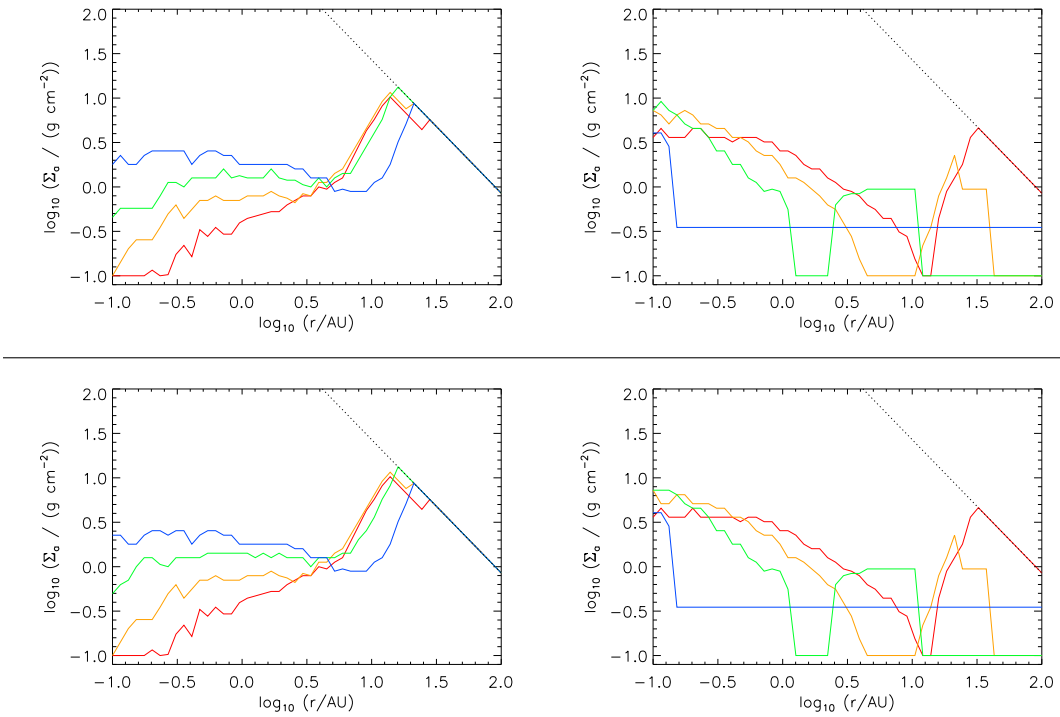

Figure 5.1: Top row: $\Sigma_{\rm a}(r)$ for a disk with the power law surface density described by Eq. 5.13 and $\alpha = 0.01$ in the active layers for a variety of magnetic field strengths. [Left: $B = 10^{-6}\,{\rm G}$ (red), $10^{-5}\,{\rm G}$ (orange), $10^{-4}\,{\rm G}$ (green), and $10^{-3}\,{\rm G}$ (blue); Right: $B = 10^{-2}\,{\rm G}$ (red), $10^{-1}\,{\rm G}$ (orange), $1\,{\rm G}$ (green), and $10\,{\rm G}$ (blue).] Bottom row: A disk with the same mass as the top row but with $\alpha = 0.03$ in the active layers; the division of magnetic field strengths and color assignments is the same as the top row.

that small does very little to the midplane temperature, which controls other aspects of the disk such as density and viscosity.

Comparing our results to those of Sano et al. (2000) we notice similar structure in $\Sigma_{\rm a}(r)$ for $r \gtrsim 10\,{\rm AU}$ for disks with the uniform B-field $\leq 100\,{\rm mG}$. In this region the $\Sigma_{\rm a}(r)$ distribution is peaked. The right side of the peak coincides with (or closely follows) the total mass surface density for the disk, meaning that for this range of r (roughly $> 20 - 30\,{\rm AU}$) the disk is fully active and $\Sigma_{\rm a} \propto r^{-1.5}$. Left of the peak $\Sigma_{\rm a}$ increases sharply with radius, sometimes as steep as $\Sigma_{\rm a} \propto r^3$. For this range in B the precise location of the peak appears to be somewhat insensitive to the field strength;

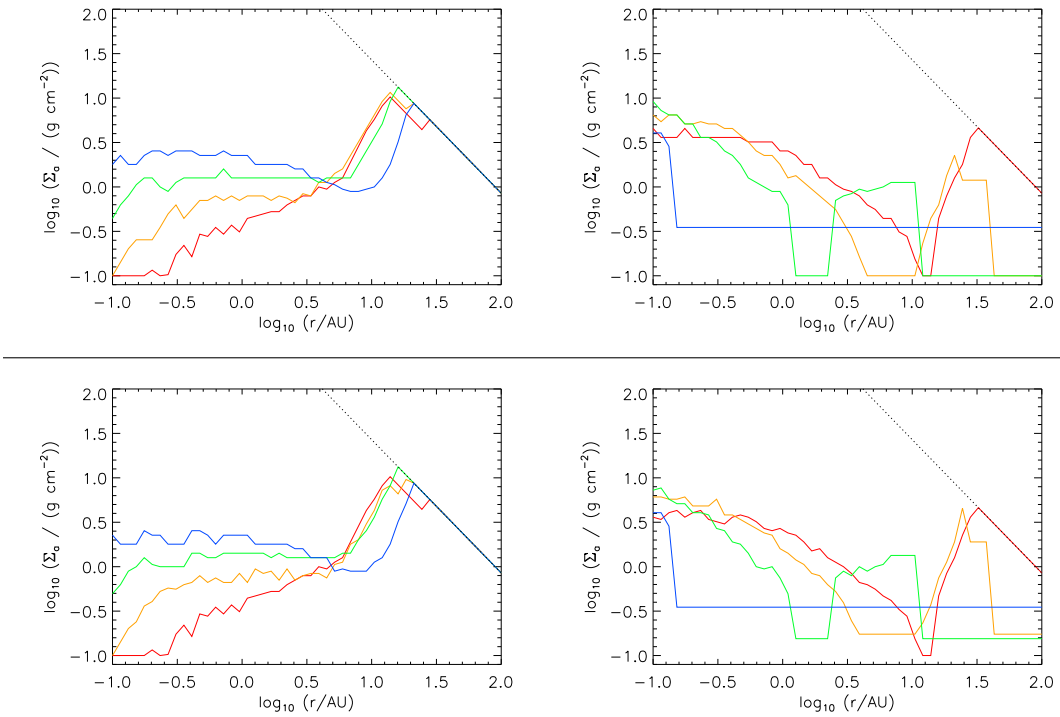

Figure 5.2: $\Sigma_{\rm a}(r)$ for a disk with the same mass as Fig. 5.3. Top frames: $\alpha = 0.1$ in the active layers. Bottom frames: $\alpha = 0.3$ in the active layers. The magnetic field strengths are divided between left and right in a fashion similar to Fig. 5.3. The color assignments are also similar.

increasing B by orders of magnitude from $1\,\mu$G has little effect on the radius of the peak until the field is 1-10 mG. For $B \geq 1.0\,$G the similarities to the models of Sano et al. (2000) are not present. This is not a problem since Sano's work involved B fields that decreased with r. In those models $B(30\,{\rm AU}) = 7.56$mG; our imposed field is far greater. The effects of ambipolar diffusion, which grows with B serves to fight instability at those radii given the field strengths imposed.

Interior to $r \approx 10\,$AU, however, the $\Sigma_{\rm a}(r)$ distribution for most of these models with $B \leq 0.1\,$G departs from that previously seen in other simulations. In Sano et al. (2000) $\Sigma_{\rm a}$ increases with r in the region of the disk where the disk is not fully active (i.e. a dead zone is present around the midplane). Our models indicate that in this region the active layer thickness

tends to be of a more complicated form. The weakest field model ($B = 1\,\mu$G) does follow the pattern exhibited in the models of Sano et al. (2000), with Σ_a increasing with r from its minimum of $\Sigma_a = 0.1\,\mathrm{g\,cm^{-2}}$ at $r = 0.1\,\mathrm{AU}$ until the disk becomes fully active at $r \approx 10\,\mathrm{AU}$. For **B**-fields in the range 10 μG to 0.1 G, two trends are seen. As the applied magnetic field in the active layer is strengthened, Σ_a increases for the innermost annuli ($r \lesssim 3\,\mathrm{AU}$). The active layer thickness at the inner boundary of the disk increases to 3.98 $\mathrm{g\,cm^{-2}}$ for $B = 0.1\,\mathrm{G}$. A consequence of these elevated Σ_a values for stronger magnetic fields is that active layer thickness no longer increases monotonically where the disk is not fully active. For B between 0.1 and 100 mG a second local maximum in Σ_a is found. This means that the physical volume that is involved with the transportation of material radially through the disk could decrease as r increases, an idea that will be explored later in this chapter. The second trend apparent involves the local minimum in Σ_a between the 2 maxima. As the **B**-field is strengthened, the location of this minimum moves outward and the depth of the minimum becomes more pronounced. For this set of models the $B = 0.1\,\mathrm{G}$ case has the deepest minimum of $\Sigma_a = 0.1\,\mathrm{g\,cm^{-2}}$ at $r = 12.6\,\mathrm{AU}$.

The two highest magnetic field strengths tested exhibit behaviors that deviate significantly from the rest and will be briefly discussed individually here. The $B = 1.0\,\mathrm{G}$ model resembles the previously addressed models for small radii ($r < 1\,\mathrm{AU}$) in that $\Sigma_a(r)$ begins at a local maximum at the disk's inner edge and decreases with bigger r. The active layer thickness drops off significantly in two regions. First, in a relatively narrow region between 1.25 and 2.25 AU Σ_a drops to $\leq 0.1\,\mathrm{g\,cm^{-2}}$. This dropoff appears to follow a trend seen in the $B = 0.01$ and $0.1\,\mathrm{G}$ simulations: a local maximum that shifts inward with increasing B-field strength. Outward of this region,

however, the Σ_a profile looks drastically different. The active layer thickness is essentially uniform between 3 and 10 AU, before dropping to $\Sigma_a \leq 0.1\,\mathrm{g\,cm^{-2}}$ for $r > 10\,\mathrm{AU}$. This second dropoff in Σ_a can probably be ascribed to the effects of a relatively strong magnetic field on an area of the disk with a low ionization state.

The last model presented here is for $B = 10\,\mathrm{G}$. The active layer thickness for this B-field strength is at a uniformly small value ($\Sigma_a \approx 0.3\,\mathrm{g\,cm^{-2}}$) for most of the disk. This reflects the effects of a strong magnetic field on the stability of the disk. As with the $B = 1\,\mathrm{G}$ model at $r > 10\,\mathrm{AU}$, a strong magnetic field suppresses the instability, drastically lowering the ability of the disk to move mass radially.

To summarize, the low mass disk exhibits behavior that is similar to what was seen in previous models. Regardless of the strength of B, a dead zone is present out to $r \approx 10 - 30\,\mathrm{AU}$. The thickness of the active layer reaches its maximum value at the outer edge of the dead zone. As B is increased, Σ_a in the inner annuli increases until $B = 1\,\mathrm{G}$, after which the active layer thickness decreases as B goes up to 10 G. At the outer edge of the dead zone, Σ_a ranges between 3 and 10 $\mathrm{g\,cm^{-2}}$. Over the range tested, α has little impact on the Σ_a profiles. The active layer thickness does not exceed $10\,\mathrm{g\,cm^{-2}}$ anywhere in the disk.

Figures 5.3 and 5.4 present Σ_a in the high mass disk. As in the low-mass disk, we find that the value of α in the active layers has a negligible effect on Σ_a. We also find that the magnetic field strength has a complicated effect on the active layer thickness.

As with the models presented for the low-mass disk, the active layer thicknesses resemble those produced by Sano et al. (2000) in the outer

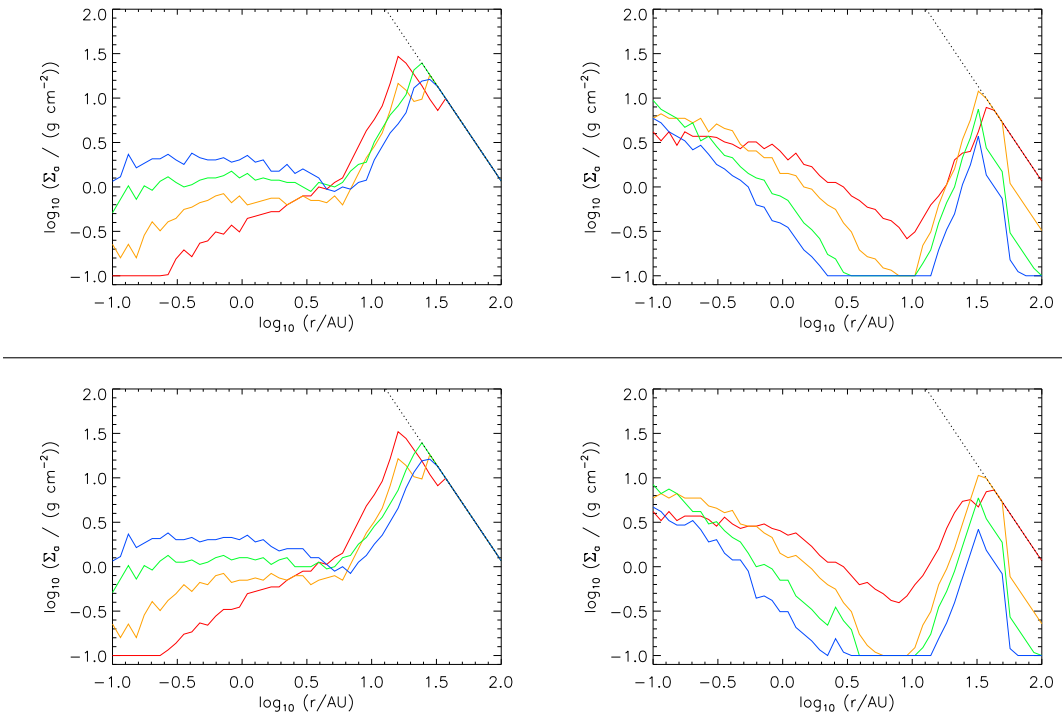

Figure 5.3: Top row: $\Sigma_{\rm a}(r)$ for a disk with the piecewise power law surface density described in Eq. 5.14 and $\alpha = 0.01$ in the active layers for a variety of magnetic field strengths. [Left: $B = 10^{-6}\,{\rm G}$ (red), $10^{-5}\,{\rm G}$ (orange), $10^{-4}\,{\rm G}$ (green), and $10^{-3}\,{\rm G}$ (blue); Right: $B = 10^{-2}\,{\rm G}$ (red), $10^{-1}\,{\rm G}$ (orange), $1\,{\rm G}$ (green), and $10\,{\rm G}$ (blue).] Bottom row: A disk with the same mass as the top row but with $\alpha = 0.03$ in the active layers; the division of magnetic field strengths and color assignments is the same as the top row.

regions ($r \gtrsim 10\,{\rm AU}$). However, unlike the low mass disk models, all field strengths yielded this profile (magnetic fields of 1 G or stronger yield significantly suppressed active layers for the lower disk mass).

A general insensitivity between field strength and location of peak active layer thickness is seen. While the tested **B**-field strengths varied over 7 orders of magnitude, the location of the peak moved between 16 and 30 AU. with no clear trend evident. Increasing the strength of the magnetic field in the active layer moves the location of the peak both inward and outward. A small movement of this peak is not without consequences, however. For models with $B \leq 0.1\,{\rm G}$ the peak in $\Sigma_{\rm a}$ occurs at a place where the disk is

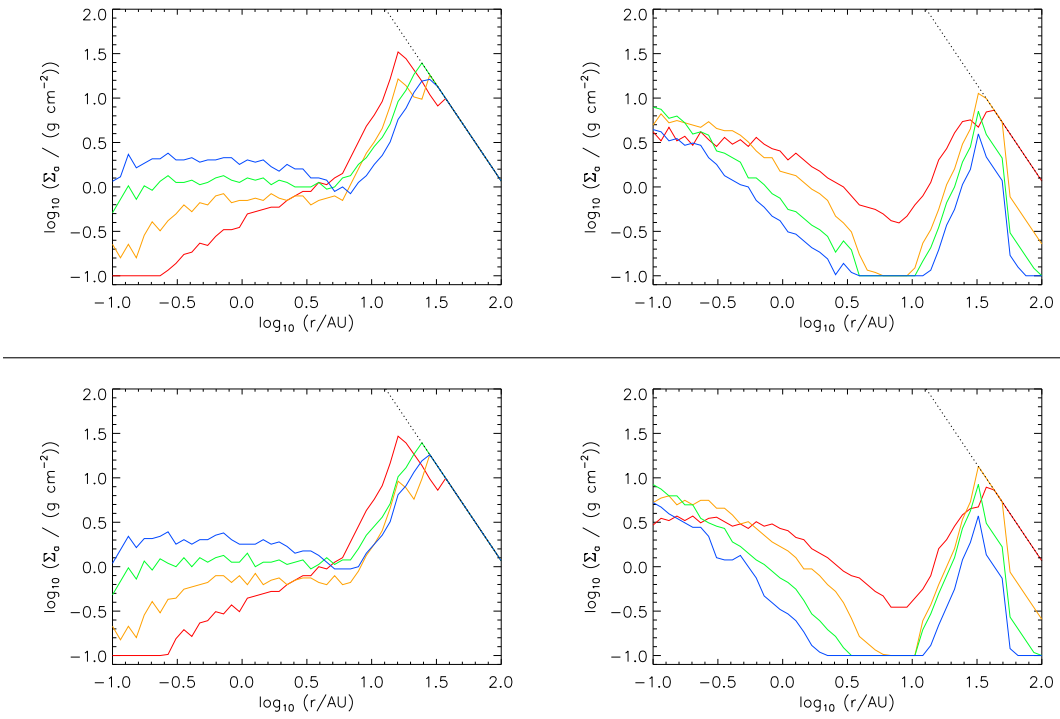

Figure 5.4: $\Sigma_{\rm a}(r)$ for a disk with the same mass as Fig. 5.3. Top frames: $\alpha = 0.1$ in the active layers. Bottom frames: $\alpha = 0.3$ in the active layers. The magnetic field strengths are divided between left and right in a fashion similar to Fig. 5.3. The color assignments are also similar.

fully active (i.e. no dead zone). With our adopted power law surface density profile, a shift from 16 to 30 AU translates to a decrease in $\Sigma_{\rm a}$ magnitude from 62 to 16 $\mathrm{g\,cm^{-2}}$. This has implications on the ability of the disk to evolve via radial mass flow, as will be explored later. Since the peak is not moving much as the field is changed, the inward side of the peak is relatively unchanged as well. One caveat to this discussion of the $\Sigma_{\rm a}$-peak shifting is that between 16 and 30 AU there are only 4 radial zones in our grid; therefore it is difficult to draw too many conclusions from this shift.

Inside of 10 AU, the same departure from the Sano et al. (2000) models is seen for all but the weakest field ($B = 1\,\mu$G). The model with the aforementioned field strength has a simple $\Sigma_{\rm a}$ profile (similar to that of the low mass disk with $B = 1\,\mu$G) where the active layer thickness is at a

minimum at the inner edge of the disk, growing with radius until the peak at $r = 16\,\mathrm{AU}$, after which the profile is coincident with the surface density of the disk (or follows it closely). More interesting are the other **B**-field cases. As B strengthens from 1 μG to 1 G, Σ_a at the inner edge of the disk rises. The strongest field tested, $B = 10\,\mathrm{G}$, has an inner edge active layer thickness roughly equivalent to the $B = 0.1\,\mathrm{G}$ case, suggesting that there is a maximum Σ_a for our disk's inner edge at $\approx 10\,\mathrm{g\,cm^{-2}}$.

As this increase of Σ_a at the inner edge is happening, a local minimum is growing in depth and width in the middle radii of the disk. This dip first appears as a kink in the Σ_a profile for $B = 10\,\mu\mathrm{G}$ between $r = 3$ and 5 AU where the monotonic increase of active layer thickness with radius is briefly broken. Once $B = 1\,\mathrm{mG}$ the magnitude of the dip, coupled with the higher values of Σ_a inside the dip yields the thinnest active layer in the dead zone area not at the inner edge, but at the bottom of the dip at $r = 6.3\,\mathrm{AU}$. This drop in magnitude becomes more and more pronounced with its sides getting progressively steeper.

As B strengthens from 1 μG to 10 mG the active layer thickness for all radii within $r \lesssim 3\,\mathrm{AU}$ increases. However, above 10 μG Σ_a diminishes with B in all but the innermost radii. The $B = 1.0$, 10.0, and to a lesser extent 0.1 G models all have dips that bring their Σ_a values below our imposed floor of $\Sigma_\mathrm{a} = 0.1$. The $B = 0.1\,\mathrm{G}$ model is $\leq 0.1\,\mathrm{g\,cm^{-2}}$ over a span of 3.7 AU. The increasing width of the span at or below the floor suggests that the bottom of the dip is quite low, perhaps on the order of 0.01 $\mathrm{g\,cm^{-2}}$ or less. This floor was set such that an annulus with an active layer thickness at that value would have negligible accretional heating. However, with such a significant drop in Σ_a it is evident that a bottleneck will exist in these disks where material moving inward from outer radii or outward from inner radii will get

trapped and be unable to flow unless the conditions of the disk change.

To summarize over our findings in the high mass disk, Σ_a profiles in the outer regions of the disk have similar shapes to those of the low mass disk. We see little movement of the location of outer edge of the dead zone, which is again where we find the thickness point of the active layer. Magnetic field strengths stronger than 1 mG exhibit a pronounced dip in Σ_a which grows as B is increased. One interesting comparison between the low and high mass disk models is the severity of the dips in Σ_a. It is possible that we are seeing the effects of an Ohmic dissipation process that is more readily able to suppress the MRI in the high mass disk at intermediate r due to the higher density of the disk at all radii; this idea will be explored in Chapter 6. As seen with the low mass disk, the active layer thicknesses of the inner annuli grow with B, turning over at $B = 1\,\mathrm{G}$. At r approaching 100 AU, $B \geq 0.1\,\mathrm{G}$ models suggest that the disk has a second dead zone that forms.

5.5 Midplane Temperatures

As with the layered accretion models presented in Chapter 3, we present here the midplane temperatures self-consistently found in our models. Figures 5.5 and 5.6 show the midplane temperatures for the low mass disks. For the disks with this surface density, the values of α and B play a small, nearly inconsequential role in determining T_{mid}. The lack of variation due to changes to α stems from the lack of α dependence on the Σ_a profiles. The apparent insensitivity to B is also as would be expected given the resulting Σ_a profiles from the range of **B**-fields tested. Figures 5.1 and 5.2 demonstrate that $\Sigma_a < 10\,\mathrm{g\,cm^{-2}}$ for all radii in all models tested. A glance at the results from Chapter 3 (Figure 3.11) indicate that in order for the magnitude of Σ_a to have a noticeable effect on T_{mid}, a combination of high α

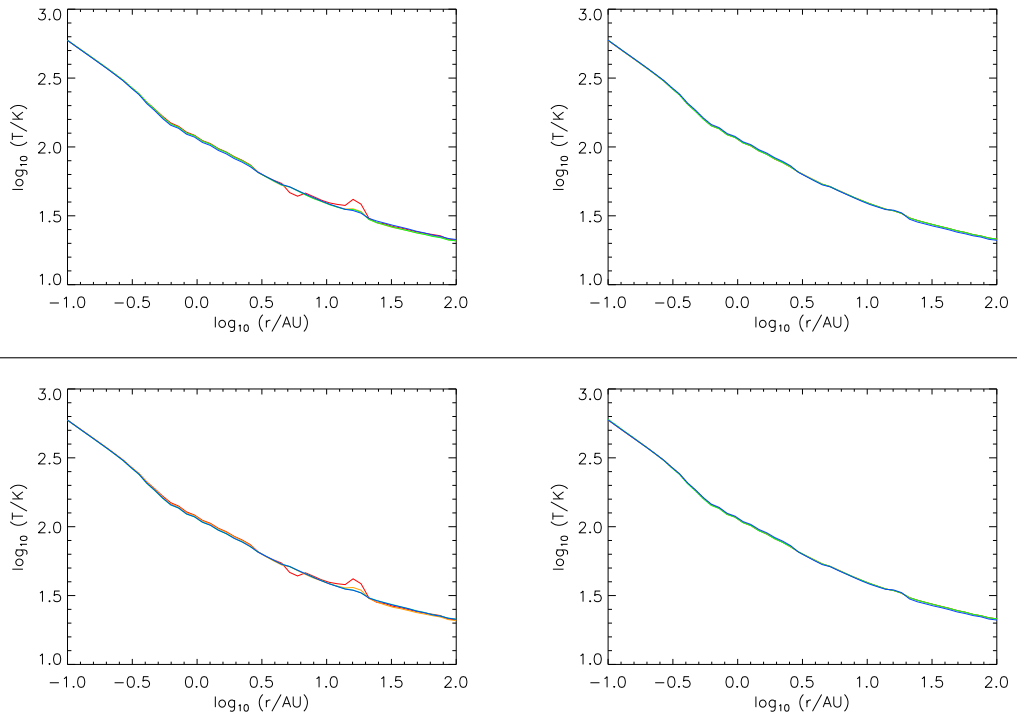

Figure 5.5: Top row: $T_{\rm mid}$ vs. r for a disk with the power law surface density described by Eq. 5.13 and $\alpha = 0.01$ in the active layers for a variety of magnetic field strengths. [Left: $B = 10^{-6}$ G (red), 10^{-5} G (orange), 10^{-4} G (green), and 10^{-3} G (blue); Right: $B = 10^{-2}$ G (red), 10^{-1} G (orange), 1 G (green), and 10 G (blue).] Bottom row: A disk with the same mass as the top row but with $\alpha = 0.03$ in the active layers; the division of magnetic field strengths and color assignments is the same as the top row.

and $\Sigma_{\rm a}$ is needed, especially $\Sigma_{\rm a}$. A large active layer thickness of 100 g cm^{-2} has an appreciably different temperature profile than those with thinner layers or no accretional heating at all (passive disks) for $\alpha \geq 10^{-3}$. However, the $\Sigma_{\rm a} = 10\,{\rm gcm}^{-2}$ curve only deviated significantly for $\alpha = 0.1$. While this condition is met, Figure 3.11 indicates that the large differences in $T_{\rm mid}$ are only evident for $r < 10$ AU. For most of the models tested here, most of the areas in the disk where $\Sigma_{\rm a}$ approaches 10 g cm^{-2} are outside of that radius.

These midplane temperature profiles are not without any features that deviate from a rough power law fit, however. An interesting feature present in many of the $T_{\rm mid}$ profiles is the bump at $r \approx 18$ AU. When

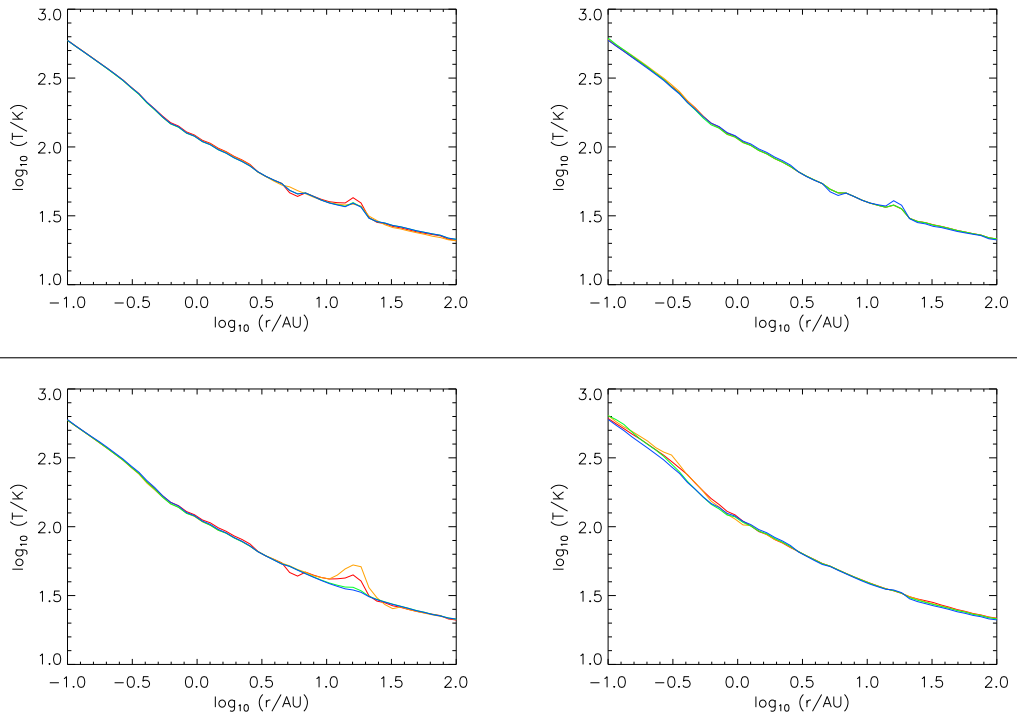

Figure 5.6: $T_{\rm mid}$ vs. r for a disk with the same mass as Fig. 5.5. Top frames: $\alpha = 0.1$ in the active layers. Bottom frames: $\alpha = 0.3$ in the active layers. The magnetic field strengths are divided between left and right in a fashion similar to Fig. 5.3. The color assignments are also similar.

$\alpha < 0.1$, the bump is the most pronounced for the $B = 1\,\mu$G, where the midplane temperature is 42 K, about 25% higher than the rest of the models at that radius. The remaining magnetic fields tested produce midplane temperature profiles that overlap with a small bump at $r \approx 18\,$AU.

When $\alpha = 0.1$, the bump is again most noticeable for $B = 1\,\mu$G. However, the difference between this model and the rest with $B \leq 1\,$mG is less, with $T_{\rm mid}$ of the bump only about 12% higher. The $\alpha = 0.3$ models show the largest disparity in $T_{\rm mid}$ at the bump. The $B = 1\,\mu$G model again has a large noticeable bump. However, the $B = 10\,\mu$G exhibits an even larger bump, with $T_{\rm mid}$ in the feature as much as 60% higher than the other disks. While probably a genuine feature of the disk, this bump is not of great interest due to its relatively small size and location in the disk. The

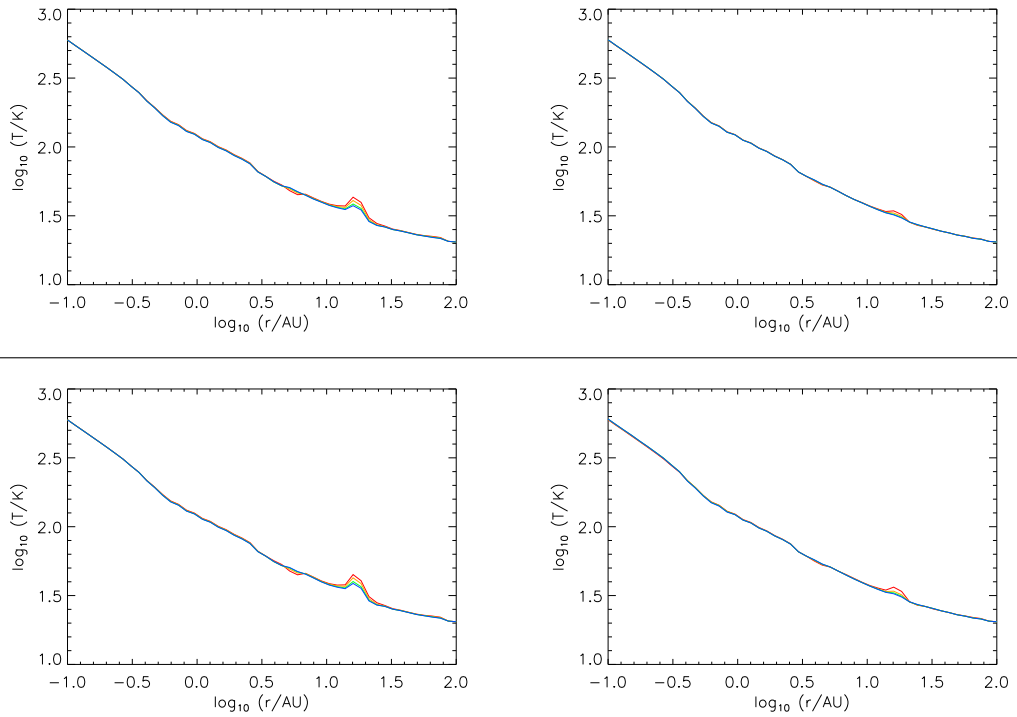

Figure 5.7: Top row: $T_{\rm mid}(r)$ for a disk with the piecewise power law surface density described by Eq. 5.14 and $\alpha = 0.01$ in the active layers for a variety of magnetic field strengths. [Left: $B = 10^{-6}\,{\rm G}$ (red), $10^{-5}\,{\rm G}$ (orange), $10^{-4}\,{\rm G}$ (green), and $10^{-3}\,{\rm G}$ (blue); Right: $B = 10^{-2}\,{\rm G}$ (red), $10^{-1}\,{\rm G}$ (orange), $1\,{\rm G}$ (green), and $10\,{\rm G}$ (blue).] Bottom row: A disk with the same mass as the top row but with $\alpha = 0.03$ in the active layers; the division of magnetic field strengths and color assignments is the same as the top row.

temperature structure is dominated by the almost power-law drop in T with r.

Figures 5.7 and 5.8 show the midplane temperatures for the high mass disks. Similar to the low mass disks discussed previously, for the high mass disks For the disks with this surface density, the values of α and B play a small, nearly inconsequential role in determining $T_{\rm mid}$. The exception again is the bump at $r \approx 16\,{\rm AU}$. For the high mass disks, the magnitude of the bump clearly decreases in size as B grows; with $\alpha = 0.01$, $T_{\rm mid}$ drops from 43 K when $B = 1\,\mu{\rm G}$ to 32 K when $B = 10\,{\rm G}$.

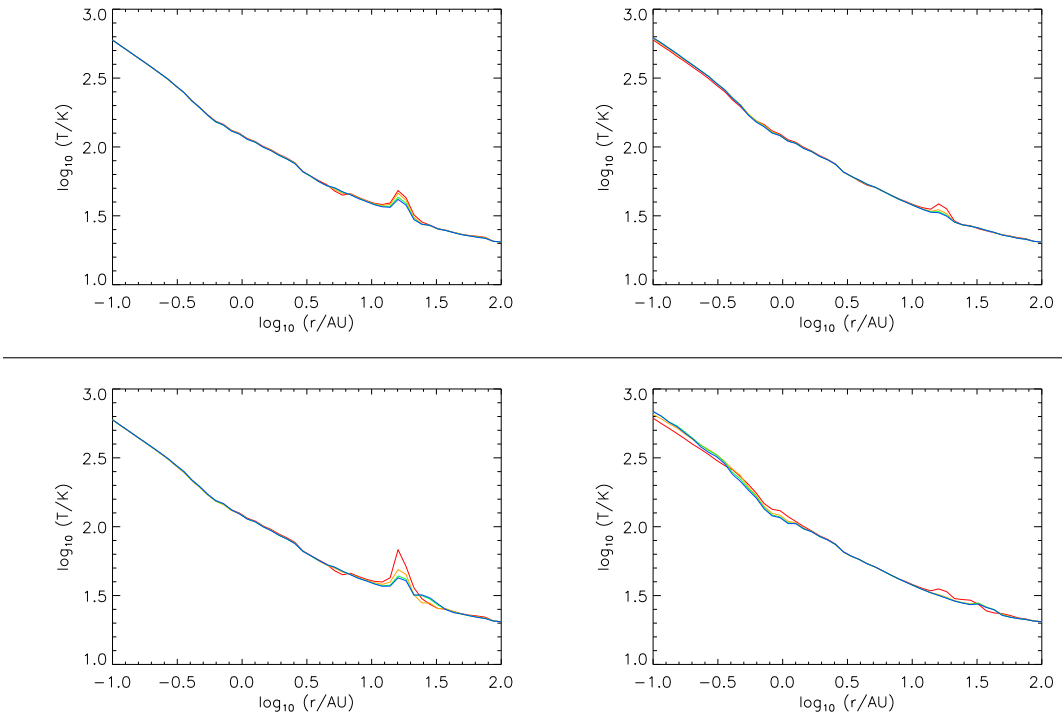

Figure 5.8: $T_{\rm mid}(r)$ for a disk with the same mass as Fig. 5.7. Top frames: $\alpha = 0.1$ in the active layers. Bottom frames: $\alpha = 0.3$ in the active layers. The magnetic field strengths are divided between left and right in a fashion similar to Fig. 5.7. The color assignments are also similar.

The bump also demonstrates a small amount of sensitivity to α as well. As the viscosity parameter grows from 0.01 to 0.3, the magnitude of the bump increases, with the width of the bump remaining unchanged. When $\alpha_{\rm a} = 0.03$, $T_{\rm mid}$ at the peak of the bump ranges from 45 to 32.5 K as B is increased. If $\alpha_{\rm a} = 0.1$, then $T_{\rm mid}$ goes from 48 to 33 K. Finally, when $\alpha_{\rm a} = 0.3$, the midplane temperature at the top of the bump ranges from 68 K down to 32 K.

The value of α has an effect on $T_{\rm mid}$ at other radii as well. For $\alpha < 0.1$, the profiles behave as the low mass profiles did, with no significant change in $T_{\rm mid}$ other than in the region around the bump. However, when $\alpha = 0.1$, midplane temperatures for $r < 0.5\,{\rm AU}$ grow as B increases. For example, at $r = 0.1\,{\rm AU}$, $T_{\rm mid}$ is largely unchanged for $B \leq 1\,{\rm mG}$, but as B grows stronger

than that, the midplane temperature rises to 621 K. The magnitude of the change decreases as r approaches 0.5 AU. In the range $0.72\,\mathrm{AU} \leq r \leq 3\,\mathrm{AU}$, T_{mid} drops as B is increased. The largest drop in this range is at $r = 0.83\,\mathrm{AU}$, where the midplane temperature drops from 132 K to 126 K.

These differences in T_{mid} for the inner annuli are more pronounced when $\alpha = 0.3$. Again, for $r < 0.5\,\mathrm{AU}$ the midplane temperature grows with B. The largest change in this zone is at $r = 0.11\,\mathrm{AU}$, where T_{mid} increases from 544 K to 636 K. There is also a range of radii ($0.72\,\mathrm{AU} \leq r \leq 3\,\mathrm{AU}$) where T_{mid} drops with increased B. At $r = 0.82\,\mathrm{AU}$, where the change is most dramatic, the midplane temperature drops from 132 K to 120 K.

To summarize, the temperature profiles found for both the high and low-mass disks largely resemble those of the passive disk as presented in Chapter 3. There are some deviations from the passive profile, most notably the bump discussed here, which is present for all values of α and for most magnetic field strengths. This is important, as it demonstrates that even when considering a complicated mass flow where there are no meaningful limits on $\dot{M}$ or Σ_{a} the temperature structure can be approximated by a power law resembling $T\ r^{-1/2}$.

5.6 Mass Flow

In the preceding sections the active layer thicknesses and temperatures of the models were presented. While interesting in their own right, having ascertained those quantities we can proceed to calculate other properties of the disk, such as the rate of mass flow through the disk for the snapshot in time simulated by the models. It is important to note that we are making calculations based on the data from the models, the models themselves do not calculate mass flow during their iterations (as opposed to disk chemistry,

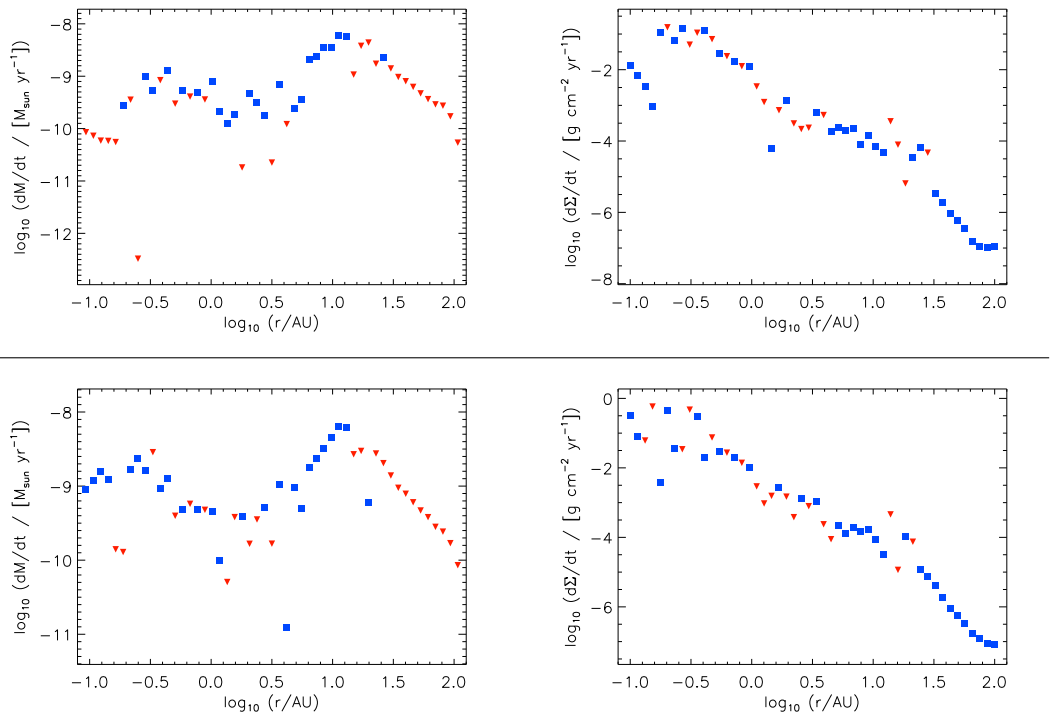

Figure 5.9: $|\dot{M}_r(r)|$ and $|\dot{\Sigma}(r)|$ for the low mass disk with $\Sigma(r)$ calculated from Eq. 5.13 and $\alpha = 0.1$. Absolute values are plotted for both $\dot{M}$ and Σ. Left column: $|\dot{M}(r)|$. Blue squares indicate material moving inward, red triangles indicate mass moving outward. Right column: $|\dot{\Sigma}(r)|$. Annuli gaining mass are represented by blue squares, those losing mass have red triangles. Top row: $B = 1\,\mu$G; bottom row: $B = 10\,\mu$G.

temperatures, and active layer thicknesses). Therefore, what we are engaging in now is a first-principles evaluation of the data. (See §5.1 for a thorough description of the terms and equations involved.)

dM/dt profiles

We will begin our analysis with a computation of the radial mass flow rate through the disk, $\dot{M}_r$. Remember that based on the formulation of Eq. 5.7, a positive value of $\dot{M}$ indicates mass moving toward the central protostar, a negative value denotes mass moving away from the star.

We shall restrict our discussion of $\dot{M}_r$ to the case of $\alpha = 0.1$ due to

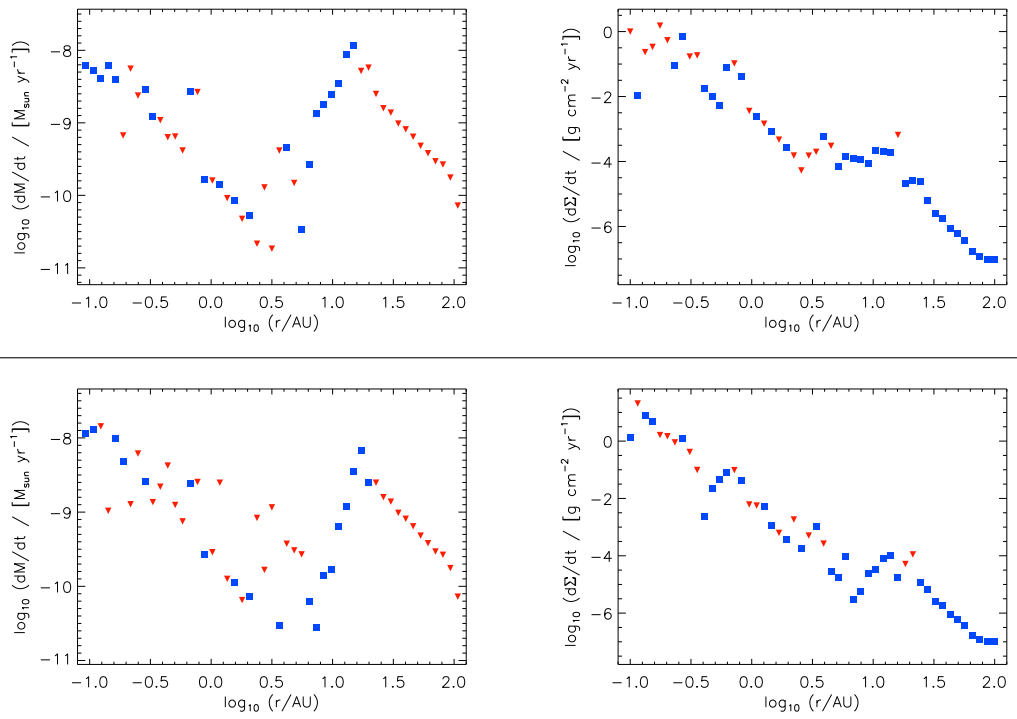

Figure 5.10: $|\dot{M}_r(r)|$ (left column) and $|\dot{\Sigma}(r)|$ (right column) for a low mass disk with $\alpha = 0.1$ and two values of magnetic field: $B = 0.1\,\mathrm{mG}$ (top row) and $B = 1\,\mathrm{mG}$ (bottom row). The symbol colors follow those of Figure 5.9.

the apparent insensitivity to α over the range of 0.01 to 0.3 as discussed previously. The left frames of Figures 5.9, 5.10, 5.11, and 5.12 present the radial mass flow for our suite of models with B varying from $1\,\mu$G to 10 G. Figures 5.13, 5.14, 5.15, and 5.16 present our mass flow results for the heavy disk.

A number of similar features are seen in these $\dot{M}_r$ plots. Nearly all of the mass flow profiles contain an almost power law decrease of $\dot{M}_r$ with r for the outer radii ($r \gtrsim 10\,\mathrm{AU}$). This feature is due to the disks becoming fully active at the outer radii, thus making $\Sigma_\mathrm{a} \propto r^{-1.5}$ for the low mass disks and $\propto r^{-2.158}$ for the high mass disks. This clean power law drop in $\dot{M}_r$ is of course absent from $B = 1$ and $10\,\mathrm{G}$ models of the low mass disk due to the irregular nature of the Σ_a profiles. The low mass disk's $B = 0.1\,\mathrm{G}$ is not fully

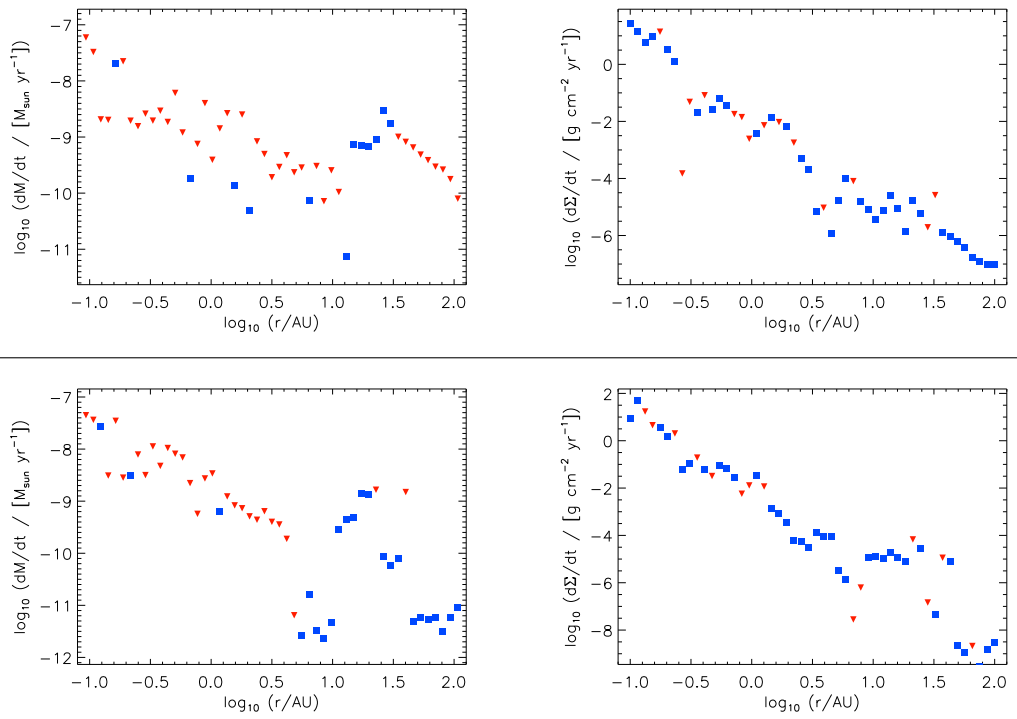

Figure 5.11: $|\dot{M}_r(r)|$ (left column) and $|\dot{\Sigma}(r)|$ (right column) for a low mass disk with $\alpha = 0.1$ and two values of magnetic field: $B = 10\,\mathrm{mG}$ (top row) and $B = 100\,\mathrm{mG}$ (bottom row). The symbol colors follow those of Figure 5.9.

active at the outer radii and therefore lacks the power law dropoff as well.

Annuli inward of $\sim 10\,\mathrm{AU}$ show varied behavior due primarily to the Σ_a profiles. The weakest two fields ($B = 1,\, 10\,\mu\mathrm{G}$) have a relatively small spread of $\dot{M}_r$ for $r \lesssim 10\,\mathrm{AU}$, ranging predominantly from 10^{-8} to $10^{-10}\,\mathrm{M}_\odot\,\mathrm{yr}^{-1}$ for the low mass disk and from $10^{-7.5}$ to $10^{-10}\,\mathrm{M}_\odot\,\mathrm{yr}^{-1}$. Mass flow rates such as these would be consistent with the lower end of mass accretion rates observed in T Tauri stars of $\sim 10^{-9}\,\mathrm{M}_\odot\,\mathrm{yr}^{-1}$ (Hartmann et al. 1998).

As the magnetic field strength in the active layer is increased, two interesting trends are seen. First of all, the range of $\dot{M}_r$ calculated increases. For the low mass disk, the increase in the range of mass flow rates is due partly to the rise in $\dot{M}_r$ at inner radii; at the disk's inner edge, $\dot{M}_r$ rises to

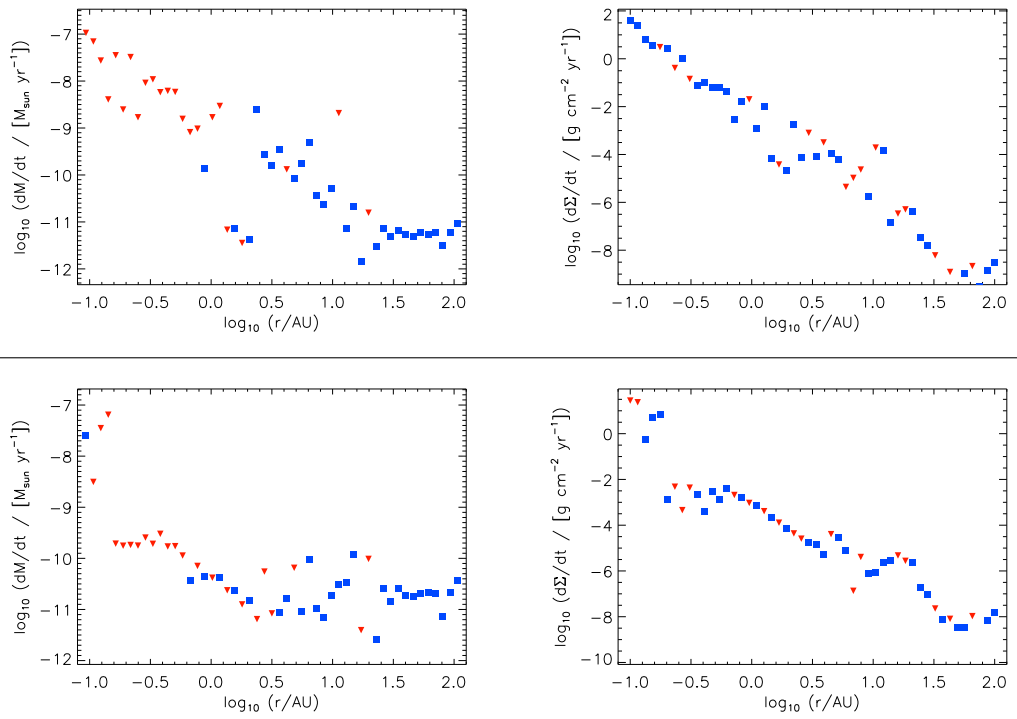

Figure 5.12: $|\dot{M}_r(r)|$ (left column) and $|\dot{\Sigma}(r)|$ (right column) for a low mass disk with $\alpha = 0.1$ and two values of magnetic field: $B = 1\,\mathrm{G}$ (top row) and $B = 10\,\mathrm{G}$ (bottom row). The symbol colors follow those of Figure 5.9.

$\sim 10^{-7}\,\mathrm{M}_\odot\,\mathrm{yr}^{-1}$. However, the minimum $\dot{M}_r$ drops with increased B as well, on account of the severe dip in Σ_a seen for the higher **B**-fields. This is an example of the bottleneck discussed earlier, mass wants to flow through the disk, however, due to the local conditions, much of the mass is stuck while only a trickle is allowed through.

The high mass disk starts with a mass flow range between $\dot{M}_r = 10^{-10}$ and $10^{-7}\,\mathrm{M}_\odot\,\mathrm{yr}^{-1}$ for $B = 1\,\mu\mathrm{G}$. The lowest values are present at the inner edge of the disk, where Σ_a is at a minimum. Similar to the low mass disk, an increase in **B**-field strength yields an increase in $\dot{M}_r$ for annuli near the disk's inner edge, in this case up to a maximum value of $\dot{M}_r = 10^{-7.5}$. Figures 5.13, 5.14, 5.15, and 5.16 also demonstrate that the slope of $\dot{M}_r$ steepens as B is increased, which has implications on whether annuli will tend to build up

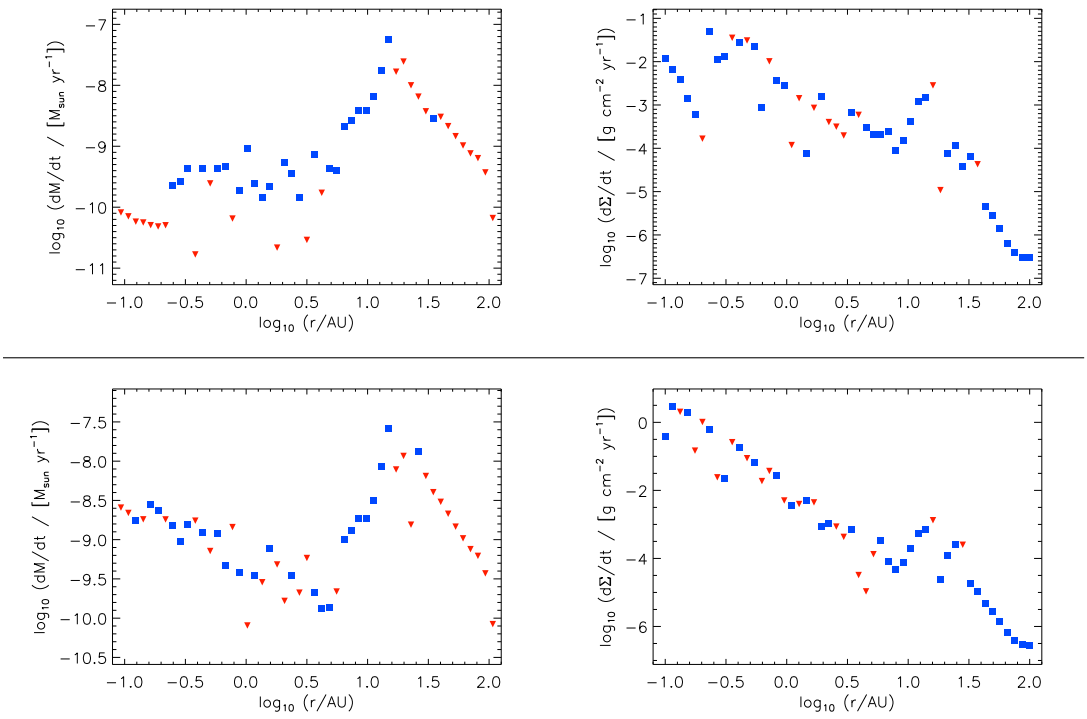

Figure 5.13: $|\dot{M}_r(r)|$ and $|\dot{\Sigma}(r)|$ for the heavy disk with $\Sigma(r)$ calculated from Eq. 5.14 and $\alpha = 0.1$. Absolute values are plotted for both $\dot{M}$ and $\dot{\Sigma}$. Left column: $|\dot{M}_r(r)|$. Blue squares indicate material moving inward, red triangles indicate mass moving outward. Right column: $|\dot{\Sigma}(r)|$. Annuli losing mass are represented by blue squares, those gaining mass have red triangles. Top row: $B = 1\,\mu$G, Bottom row: $B = 10\,\mu$G.

mass or evacuate, as will be discussed later in this chapter. These models with higher **B**-fields also exhibit a steep positive slope in radial mass flow around $r \sim 10\,$AU. This steepness will not be addressed here due to its existence being due partly to the imposed floor in $\Sigma_{\rm a}$. An unfortunate byproduct of this imposed minimum value is that for that stretch in r, $d\Sigma_{\rm a}/dr = 0$ and the $\dot{M}_r$ changes are being driven entirely by the slope of $T_{\rm mid}$. However, even though $d\Sigma_{\rm a}/dr = 0$ is an unphysical condition on the system, it is not unexpected for $\dot{M}$ to vary with $T_{\rm mid}$; some change in $\dot{M}$ over this range is expected.

The second trend involves the direction of mass flow through the disk.

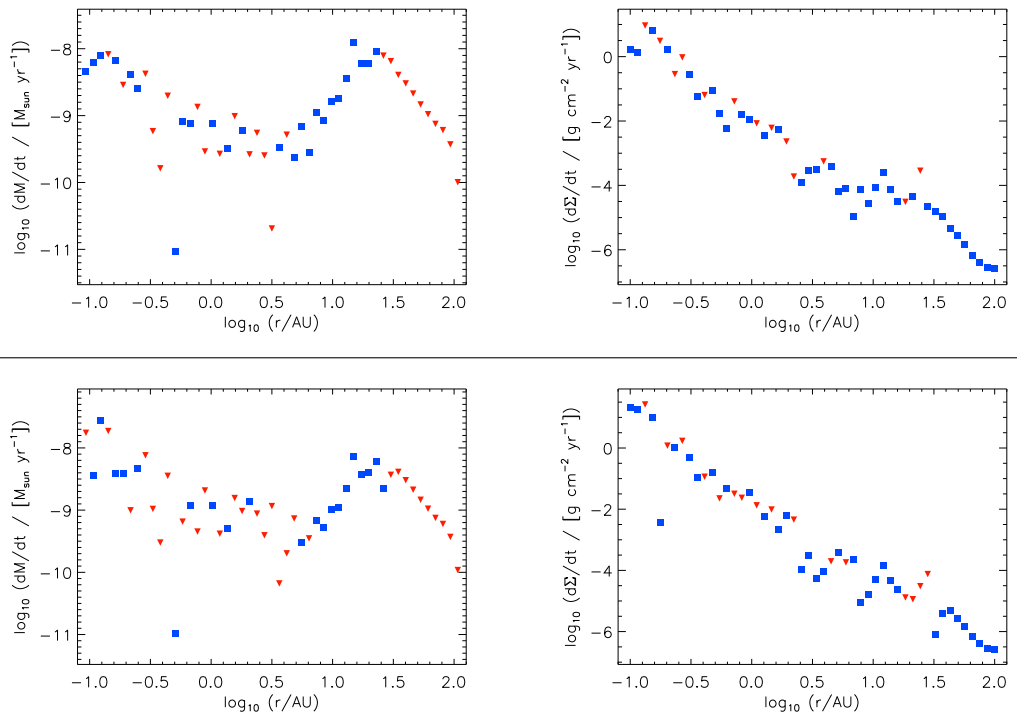

Figure 5.14: $|\dot{M}_r|$ (left column) and $|\dot{\Sigma}|$ (right column) vs. r for a high mass disk with $\alpha = 0.1$ and two values of magnetic field: $B = 0.1\,\mathrm{mG}$ (top row) and $B = 1.0\,\mathrm{mG}$ (bottom row). The symbol colors follow those of Figure 5.13.

Figure 5.9 demonstrates via color-coding that for a low strength **B**-field with our adopted surface density profile, mass tends to flow outward where the disk is fully active, and inward where the disk has a dead zone. There are individual points in the inner annuli where the calculation using Eq. 5.7 yields a negative (outward) value for $\dot{M}_r$. However, those are most likely due to small instabilities in the Σ_a profile (or in the case of $B = 1\,\mu\mathrm{G}$, Σ_a being at our floor value for the innermost r), the overall trend for those low-B models is to move mass inward at small r. As the **B**-field increases in strength, the trend seems to be for an increasing number of annuli with dead zones to contain a negative (outward) mass flow. This is due to the feature of Σ_a described earlier, an active layer thickness that decreases with increasing r for $r \lesssim 3\,\mathrm{AU}$. Figures 5.10 and 5.11 illustrate this trend; once B has been

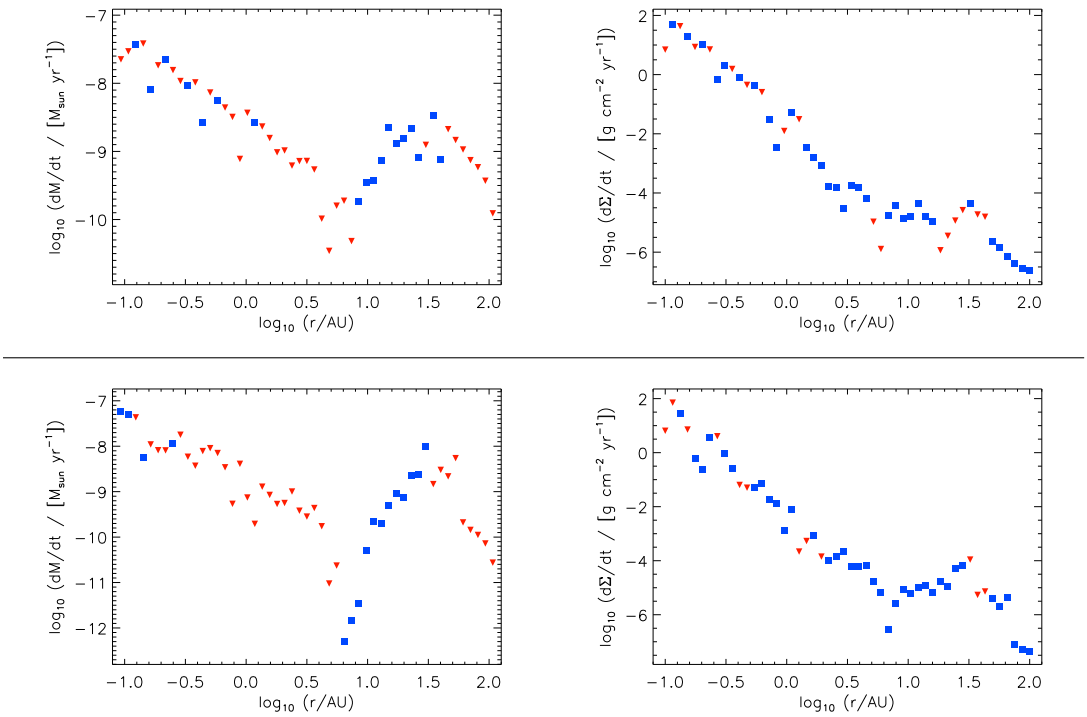

Figure 5.15: $|\dot{M}_r|$ (left column) and $|\dot{\Sigma}|$ (right column) vs. r for a high mass disk with $\alpha = 0.1$ and two values of magnetic field: $B = 10\,\mathrm{mG}$ (top row) and $B = 100\,\mathrm{mG}$ (bottom row). The symbol colors follow those of Figure 5.13.

strengthened to 100 mG, annuli within $r < 3\,\mathrm{AU}$ overwhelmingly tend to move mass outward. In fact, for that case, only 3 of 29 annuli within that radius range returned positive values of $\dot{M}_r$; as with the handful of negative exceptions found in the weak B-field models, these points are almost certainly outliers owing their adherent behavior to noise in the Σ_a profile.

The high-mass models exhibit this same trend. When the magnetic field strength is low, the inner portion of the disk tends to move mass inward (see Figure 5.13). Figures 5.14, 5.15, and 5.16 demonstrate the transition from mass moving predominantly inward to outward over the orders of magnitude changes to B.

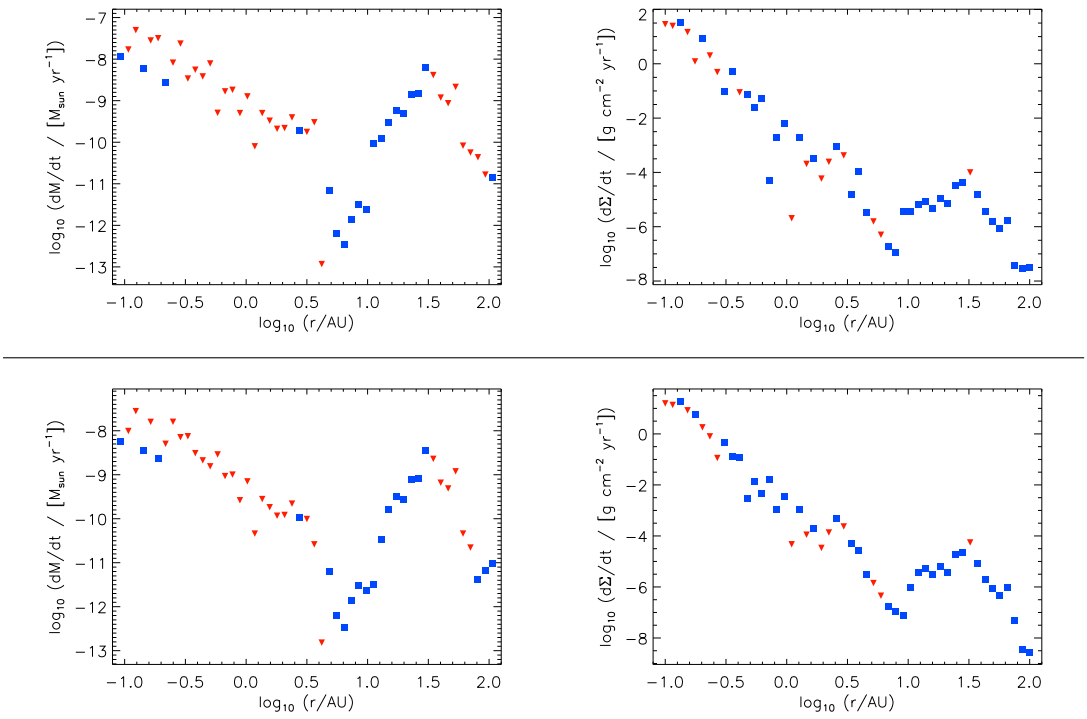

Figure 5.16: $|\dot{M}_r(r)|$ (left column) and $|\dot{\Sigma}(r)|$ (right column) for a high mass disk with $\alpha = 0.1$ and two values of magnetic field: $B = 1\,\mathrm{G}$ (top row) and $B = 10\,\mathrm{G}$ (bottom row). The symbol colors follow those of Figure 5.13.

dΣ/dt profiles

We now move on to the calculations of the rates of mass moving in and out of each annulus, $\dot{\Sigma}$ using Eq. 5.8. In this context, negative values equate to mass leaving the annuli over time and positive values mean mass is accruing.

The right frames of Figures 5.9, 5.10, 5.11, and 5.12 present our calculated annulus' mass gain/loss for the low mass disk with a surface density profile described by Eq. 5.13. Similarly, the right frames of Figures 5.13, 5.14, 5.15, and 5.16 plot $\dot{\Sigma}$ for the high mass disk. Essentially we are transforming the $\dot{M}_r(r)$ profiles into $\dot{\Sigma}(r)$ profiles. Therefore, $\dot{\Sigma}$ depends on the previously presented T_{mid} and Σ_{a} values as well. Due to the similarities in midplane temperature and active layer thickness over the range of α

tested, we will only show the derived annulus mass flow profiles for $\alpha = 0.1$.

Due to the fluctuations seen in $\Sigma_{\rm a}$ (and therefore in $\dot{M}_r$), it is not possible to draw major conclusions at the single-annulus level. As previously stated, the $\dot{M}_r$ profiles were smoothed using nearest-neighbor averaging before calculating $\dot{\Sigma}$ (if neighboring points were of same sign) in order to smooth over the sometimes rapid radial variations to reveal underlying trends. That being said, some trends can still be identified and discussed.

As has been seen in the preceding sections, the profiles for $T_{\rm mid}$ and $\Sigma_{\rm a}$ are not simple power laws. However, if we assume for the moment that locally they do obey a power law, then we can adopt $\Sigma_{\rm a} \propto r^{-p}$ and $T_{\rm mid} \propto r^{-q}$. This allows us to analytically study $\dot{\Sigma}(r)$. Using our local power law expressions for $\Sigma_{\rm a}$ and $T_{\rm mid}$, we obtain the result that locally, $\dot{\Sigma} \propto (2-p-q)(1-p-q)r^{-p-q-1}$. While of limited predictive value, such an analysis can be used to explore the results of these $\dot{\Sigma}$ profiles.

Ignoring the direction of mass motion for the moment (mass accruing vs. evacuating) it is clear that the rate of net mass entering and leaving an annulus is strongly related to r. This is of little surprise since Eq. 5.8 contains an explicit $1/r$ dependence and $\dot{M}_r$ is dependent on $T_{\rm mid}$, which decreases almost monotonically with r, and $\Sigma_{\rm a}$, which with the exception of annuli near the outer dead zone boundary at best increases weakly with r. Many of the models do exhibit one area where $\dot{\Sigma}$ increases with r which coincides with the location of the sharp peak in $\Sigma_{\rm a}$. Therefore, it is safe to conclude that active layer thickness can drive the rate of net mass entering or leaving an annulus, but only if the dependence on r of the $\Sigma_{\rm a}$ profile exceeds a critical value. With the low mass disks, the strength of the **B**-field applied affects the shape of the $\dot{\Sigma}$ profile. When $B \leq 10\,\mu$G, the resulting $\Sigma_{\rm a}$ do not contain a large enough gradient to noticeably effect the magnitudes of $\dot{\Sigma}$.

However, when the magnetic field in the active layer is $\geq 0.1\,\mathrm{mG}$, a bump coinciding with the left side of the peak in Σ_a described in the previous section is clearly evident. Therefore, B plays an important role in modeling the evolution of disks away from the snapshots that are illustrated in this paper. However, a review of the high mass disks' $\dot{\Sigma}$ (Figures 5.13-5.16 reveal that it is not a simple case of higher B leading to noticeable increases to the rate of mass leaving/entering annuli. With the higher surface density profile, the weakest fields ($B = 1,\ 10\,\mu\mathrm{G}$) show the elevated bump in mass flow, yet some stronger fields ($B = 0.1,\ 1.0\,\mu\mathrm{G}$) do not. The gradient of the resulting Σ_a profile is much more important than the value of B itself.

We see from such an analysis that mass will tend to pile up in an annulus so long as $p < +(1-q)$ or $p > +(2-q)$ and will evacuate an annulus if $(1-q) < p < (2-q)$. A quick study of the T_mid profiles reveals that over the range $0.1\,\mathrm{AU} < r < 10\,\mathrm{AU}$, the midplane temperature profiles roughly obey $T_\mathrm{mid} \propto r^{-0.6}$. If we set $q = 0.6$, our condition for accumulating mass becomes $p < +0.4$ or $p > +1.4$ and mass will tend to evacuate if $0.4 < p < 1.4$. An examination of Figures 5.2 and 5.4 shows that there are stretches where the general trend of the active layer thickness profile is within the range of p discussed to facilitate mass evacuating certain annuli, specifically in the range $0.3\,\mathrm{AU} \lesssim r \lesssim 3.0\,\mathrm{AU}$. This is important for the consideration of disk evolution. While our models only produce snapshots in time, it is still of use to see how disks under a set of conditions will tend to behave. This analysis also lends credibility to the models indicating that some annuli in the inner regions of disks will accrue material; given some of the noise in our Σ_a data, it would be reasonable to assume that some of the trends might not be real.

5.7 Accretion Timescales

As seen in the previous section, PPDs contain some annuli that are increasing in mass and others that are decreasing. Obviously, annuli that are losing mass cannot do so indefinitely as the annulus will eventually be evacuated of material. However, annuli that are gaining mass cannot do so either. Eventually, the annulus' local Σ will exceed what is stable to gravitational effects and become gravitationally unstable, as we discussed earlier in Chapter 1. We will now calculate the timescales. Recall from §5.1 that we defined two relevant timescales: $\tau_{\rm evac}$, the timescale for an annulus to lose all of its mass and $\tau_{\rm GI}$, the timescale for an annulus accruing mass to reach the critical density to trigger a gravitational instability, defined using the Toomre parameter, Q.

These timescales have been calculated for each annulus in each of the models presented in §5.3. It is important to note that these two timescales being computed, $\tau_{\rm evac}$ and $\tau_{\rm GI}$, do not take into consideration the lifetime of the disk. PPDs are though to last on the order of 10^7 yr, timescales that are found to be longer than that do not mean that those disks will last longer before dissipating; rather, that no appreciable change to that area of the disk will take place before the disk disappears.

The computed timescales for the low mass disk (total disk surface density, $\Sigma(r)$, defined by Eq. 5.13) are shown in Figures 5.17 & 5.18. Disks with $B \lesssim 100\,\mu$G have evacuation and GI timescales that do not track together in magnitude. Additionally, no clear trend is seen in either. The GI timescale decreases with r to a minimum between $r = 2$ and 3 AU, after which it increases with r to the outer edge. However, $\tau_{\rm evac}$ increases with r to a radius of 2-3 AU, then decreases to the outer edge. Interestingly, as the

applied **B**-field is increased, the two timescales begin to agree in magnitude in terms of varying with r and a trend develops where $\tau \propto r^n$. The $B = 1\,\mathrm{mG}$ case shows the two timescales beginning to agree in magnitude, with a rough value of $n = 1$. When B is increased to 10 mG, the agreement between τ_{evac} and τ_{GI} improves with n still ≈ 1.0 over the entire range of disk annuli being simulated. Once $B = 100\,\mathrm{mG}$ the power law slope has increased to $n \approx 5/3$. The $B = 1\,\mathrm{G}$ case has $n \approx 2$. and $B = 1\,\mathrm{G}$ have $n \approx 2$. The case of $B = 10\,\mathrm{G}$ seems to show τ has little dependence on r except at the edges of the disk. However, this may be suspect since Σ_{a} for this disk was at our imposed floor except at the inner edge. We do see some deviation from these power-law trends discussed here, however the bulk of the disagreement lies in the range where Σ_{a} was at our imposed floor value (as was discussed in §5.1). Therefore it is likely that with a different floor value for active layer thickness those trends would be cleaner.

A summary of the range of timescales seen in our low disk mass models is presented in Table 5.1. Each model has its minimum and maximum values of each timescale printed there (in Myr). Consistent with the findings of the individual models, we find that for τ_{GI} the minimum value decreases as B is turned up and that the maximum value of the timescale increases over this same period. This is what leads to the steepening of the rough power-law trend between τ_{GI} and r. The highest two **B**-fields tested $B = 1,\, 10\,\mathrm{G}$ are an exception to this trend, and given how those models differed radically in terms of Σ_{a} that is not too surprising. Significantly, for all but the $B = 1\,\mu\mathrm{G}$ case the minimum timescale is less than 1 Myr. This is important since all estimates of PPD lifetimes are well larger than that $\gtrsim 10\,\mathrm{Myr}$. Even if the rest of the disk is stable to the GI when the first annulus becomes unstable, it has been demonstrated that locally induced GI events can affect the

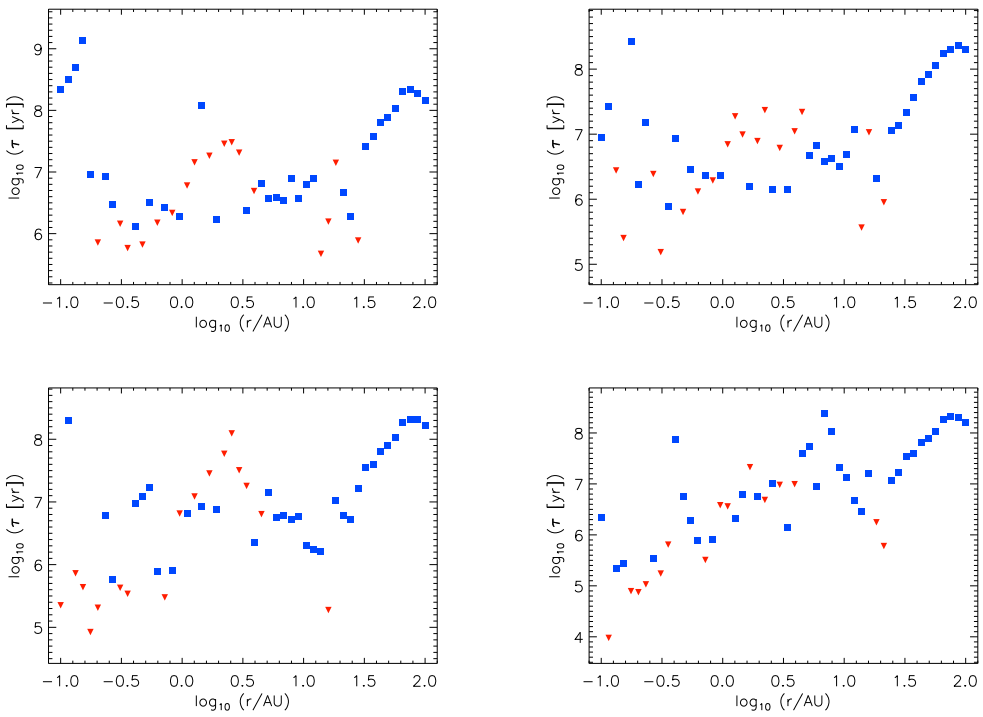

Figure 5.17: Timescales $\tau_{\rm evac}(r)$ and $\tau_{\rm GI}(r)$ for light disks with $\alpha_{\rm a} = 0.1$ and $B = 10^{-6}\,{\rm G}$ (top left), $10^{-5}\,{\rm G}$ (top right), $10^{-4}\,{\rm G}$ (bottom left), and $10^{-3}\,{\rm G}$ (bottom right),. Red triangles indicate $\tau_{\rm evac}$ (annulus losing mass), blue squares are $\tau_{\rm GI}$ (annulus gaining mass).

remaining portions of the disk (Laughlin & Rozyczka 1996).

Table 5.1 also lists the range of $\tau_{\rm evac}$. Unlike with $\tau_{\rm GI}$, the changes to the minimum and maximum values as B is increased are not uniform in direction. For example, as B is increased from $1\,\mu$G to 10 mG the minimum $\tau_{\rm evac}$ drops, as it does with the GI timescale. However, after that drop, $\tau_{\rm evac}$ increases and decreases with stronger applied **B**-fields. Similarly, the maximum values increase and decrease as B is strengthened. Annuli being evacuated of material lead to the formation of a gap in the PPD or in the case of the innermost annuli being drained of material, the central hole growing in size. The results of these models show that for a low mass disk, even a moderate strength field will lead to gaps forming on timescales of $\approx 10,000$ yr, well less than the lifetime of the disk.

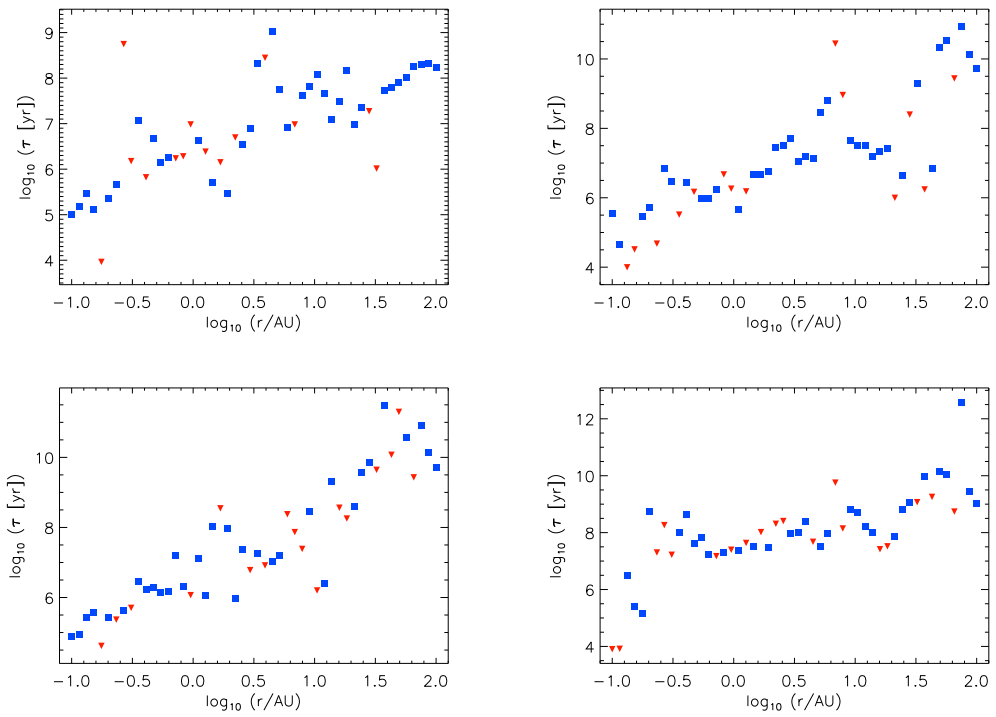

Figure 5.18: Timescales $\tau_{\rm evac}(r)$ and $\tau_{\rm GI}(r)$ for light disks with $\alpha_{\rm a} = 0.1$ and $B = 10^{-2}\,{\rm G}$ (top left), $10^{-1}\,{\rm G}$ (top right), $1\,{\rm G}$ (bottom left), and $10\,{\rm G}$ (bottom right),. Red triangles indicate $\tau_{\rm evac}$ (annulus losing mass), blue squares are $\tau_{\rm GI}$ (annulus gaining mass).

B (G)	$\tau_{\rm GI}$ (Myr) min	$\tau_{\rm GI}$ (Myr) max	$\tau_{\rm evac}$ (Myr) min	$\tau_{\rm evac}$ (Myr) max
10^{-6}	1.32	1384	0.470	30.4
10^{-5}	0.772	264	0.154	23.4
10^{-4}	0.576	208	0.0841	124
10^{-3}	0.222	242	9.51×10^{-3}	21.3
10^{-2}	0.103	1031	9.18×10^{-3}	559
0.1	0.0465	85707	9.90×10^{-3}	27672
1.0	0.0761	303581	0.0416	198691
10.0	0.140	3848710	8.01×10^{-3}	5706

Table 5.1: Range of $\tau_{\rm GI}(r)$ and $\tau_{\rm evac}(r)$ for low mass disks ($\Sigma(r)$ described by Eq. 5.13) with $\alpha = 0.1$. Timescales are in Myr.

The timescales for the heavy disk (see Eq. 5.14) and $\alpha = 0.1$ are presented in Figures 5.19 and 5.20. In general we find that $\tau_{\rm GI}$ and $\tau_{\rm evac}$ have more similar magnitudes for low **B**-field strengths than did the low mass disk models. For example, the $B = 1\,\mu$G disk has timescales that vary between

10^5 and 10^9 yr. Unlike the low mass disk, where two distinct trends were evident (one for $\tau_{\rm GI}$ and another for $\tau_{\rm evac}$), these timescales roughly follow a similar trend, which surprisingly decreases with r for annuli within $r \approx 30\,{\rm AU}$. The exception to this agreement is the $B = 10\,\mu{\rm G}$ model, where two different trends are again seen.

Similar to the low mass disk timescales presented earlier, turning up the **B**-field strength leads to better agreement between the two timescales and an overall steepening of the rough power-law dependence of τ on r. We see in the $B = 100\,\mu{\rm G}$ model that the timescales vary as roughly $\tau \propto r$ with one notable dip between 10 and 30 AU. The 1 mG model has the same r dependence, but lacks the dip seen as a result of the weaker **B**-field. The remaining models show that the r-dependence steepens to $\tau \propto r^3$ for the $B = 1$, 10 G models. One major feature that is seen in the high mass disk models and is absent from the low mass disk models is the dip in timescale centered around $\approx$30 AU. This coincides exactly with the strong peak in $\Sigma_{\rm a}$ seen for those same models, indicating that its a real feature of these high mass disk with strong **B**-fields in the active layers.

The ranges of $\tau_{\rm GI}$ and $\tau_{\rm evac}$ are listed in Table 5.2. As with the low mass models, the range in $\tau_{\rm GI}$ tends to increase as B is made stronger. However, there are more exceptions to this trend with the high mass disk models than there was with the low mass disk models. The $B = 1\,\mu{\rm G}$ and $B = 10\,{\rm mG}$ minimums are inconsistent with the overall trend of decreasing minimum values of $\tau_{\rm GI}$ as the applied magnetic field strength is increased. Likewise, the $B = 1\,\mu{\rm G}$ and $B = 1\,{\rm mG}$ are inconsistent with the overall trend of increasing maximum values of $\tau_{\rm GI}$ as B grows. As with the low mass disk models, all of the high mass disk models indicate that at least one annulus will become unstable to the gravitational instability on timescales of

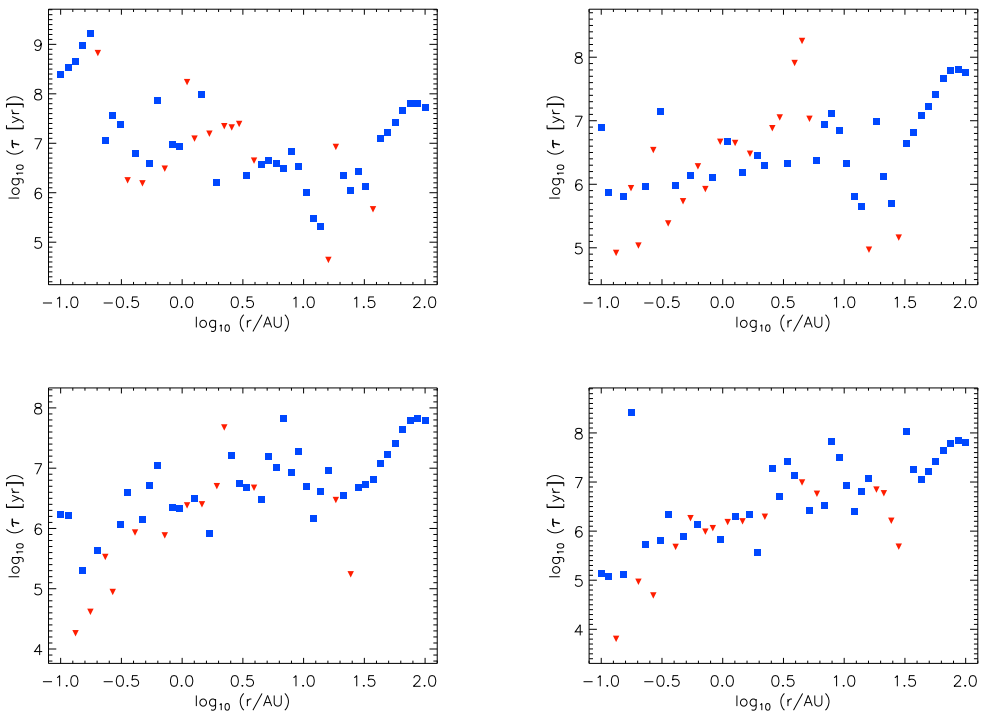

Figure 5.19: Timescales $\tau_{\rm evac}(r)$ and $\tau_{\rm GI}(r)$ for heavy disks with $\alpha_{\rm a} = 0.1$ and $B = 10^{-6}\,{\rm G}$ (top left), $10^{-5}\,{\rm G}$ (top right), $10^{-4}\,{\rm G}$ (bottom left), and $10^{-3}\,{\rm G}$ (bottom right),. Red triangles indicate $\tau_{\rm evac}$ (annulus losing mass), blue squares are $\tau_{\rm GI}$ (annulus gaining mass).

$< 1\,{\rm Myr}$. Since protoplanetary disks are likely to exist for more than 10 Myr, this means that a single disk could see several GI events over its lifetime, consistent with the idea that PPDs that fall prey to the GI are what is observationally seen with FU Orionis and EX Orionis objects.

All of our high mass disk models have $\tau_{\rm evac}$ values which suggest that gaps will form in disks more rapidly than will annuli become gravitationally unstable. It is unclear what effect this will have on overall disk evolution, as the global nature of GI events will likely cause these gaps in the disk to be refilled with disk material.

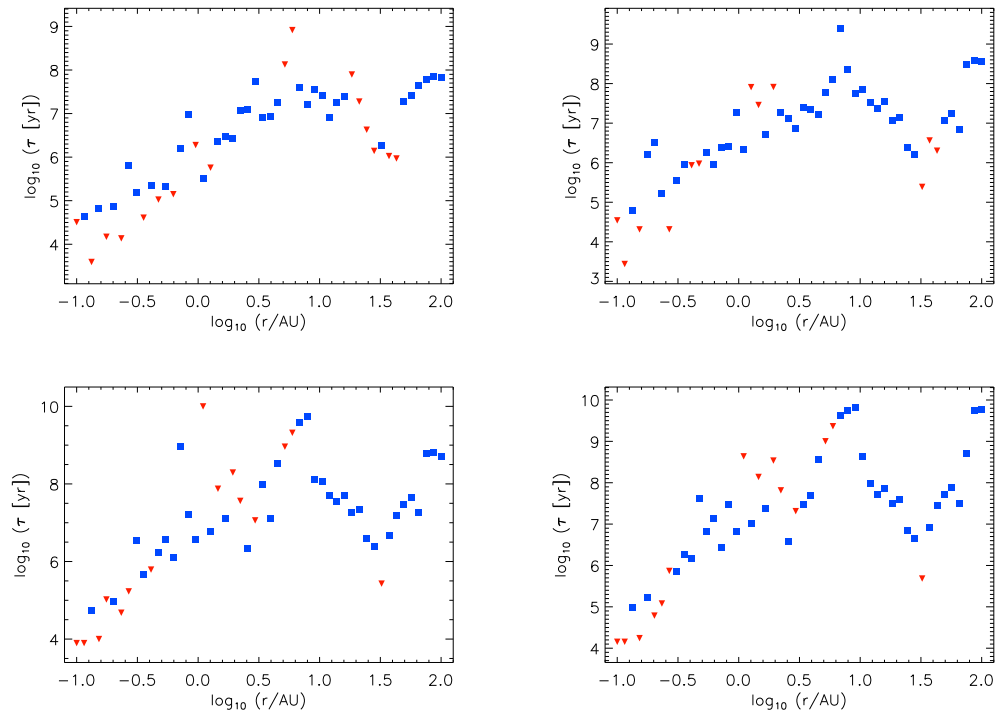

Figure 5.20: Timescales $\tau_{\rm evac}(r)$ and $\tau_{\rm GI}(r)$ for heavy disks with $\alpha_{\rm a} = 0.1$ and $B = 10^{-2}\,{\rm G}$ (top left), $10^{-1}\,{\rm G}$ (top right), $1\,{\rm G}$ (bottom left), and $10\,{\rm G}$ (bottom right),. Red triangles indicate $\tau_{\rm evac}$ (annulus losing mass), blue squares are $\tau_{\rm GI}$ (annulus gaining mass).

B (G)	$\tau_{\rm GI}$ (Myr) min	$\tau_{\rm GI}$ (Myr) max	$\tau_{\rm evac}$ (Myr) min	$\tau_{\rm evac}$ (Myr) max
10^{-6}	0.212	1624	0.0438	666
10^{-5}	0.447	65.2	0.0831	180
10^{-4}	0.201	67.8	0.0183	47.4
10^{-3}	0.120	261	6.39×10^{-3}	9.79
10^{-2}	0.0447	70.7	3.92×10^{-3}	824
0.1	0.0617	2533	2.75×10^{-3}	82.0
1.0	0.0546	5348	7.87×10^{-3}	9973
10.0	0.0963	6507	0.0143	2320

Table 5.2: Range of $\tau_{\rm GI}(r)$ and $\tau_{\rm evac}(r)$ for high mass disks ($\Sigma(r)$ described by Eq. 5.14) with $\alpha = 0.1$. Timescales are in Myr.

Chapter 6

DISCUSSION

6.1 Layered Accretion

In Chapter 1 we established the importance of protoplanetary disks in the evolution of planetary systems. Namely, they are the evolutionary step in between the collapsing cloud which precipitates star formation and the planets which may or may not eventually form before the stellar radiation sweeps away the disk. During the early stages of disk development the disk is accumulating mass from the collapsing cloud; material which is following trajectories described by Cassen & Moosman (1981). In addition to providing a place for material to accrete into planets, PPDs also feed mass onto the central protostar via interactions between the star's magnetosphere and the inner portions of the disk. These mass accretion rates onto the star have been observationally found to range from $\sim 10^{-9}$ to $\sim 10^{-6}\,\mathrm{M}_{\odot}\,\mathrm{yr}^{-1}$ (Hartmann et al. 1998). However, if material is falling onto the protostar, conservation of angular momentum demands that material in the outer portions of the disk move outward. This causes the disk to thin out over time. This effect has been noted in surveys such as those of Hartmann et al. (1998). Since the inner regions of PPDs are not seen to be immediately losing mass due to this protostellar accretion, there must be a persistent flow of mass (and therefore a constant exchange of angular momentum with the outer disk regions) through the disk itself. As discussed in Chapter 1, there is no way currently to observationally measure this mass flow within the disk. This has contributed to the difficulties over past decades to pinpoint the exact mechanism responsible for this exchange of angular momentum.

One of the major advances in PPD study in recent decades was the

discovery of the magnetorotational instability and its role in transporting mass and angular momentum within protoplanetary disks (Balbus & Hawley 1991). In conjunction with the work of Gammie (1996) a standard model of PPD mass flow was assembled. Mass flow will predominantly occur where ionization levels are sufficiently high (electron fraction $x_e \gtrsim 10^{-13}$) for disk material to couple to the magnetic fields, allowing for the instability to instigate and maintain the turbulence. Since any ionization sources of importance (e.g. protostellar X-rays, galactic cosmic rays) are external to the disk, only the top and bottom skin layers of the disk will become ionized (and therefore subject to the MRI). This introduces the concept of the "dead zone" that was first identified in the context of PPDs by Gammie (1996). The exact thickness of the ionized (or active) layer is an active area of research and in past discussions has depended largely on what type of ionization event is dominating. Gammie (1996) assumed that the primary ionization source for PPDs would be galactic cosmic rays, which due to their high energies can penetrate down to depths as high as $100\,\mathrm{g\,cm^{-2}}$. Subsequent modeling by Sano et al. (2000) suggests that active layers will be thinner, on the order of $10\,\mathrm{g\,cm^{-2}}$ due to X-rays emitted by the central protostar being the primary source. Our model results agree more with Sano's, in that active layer thicknesses will tend to be $\lesssim 10\,\mathrm{g\,cm^{-2}}$.

The role of mass accretion in setting the temperature structure and emergent spectrum of a disk has been investigated by a number of authors, as discussed in Chapter 1. These investigations generally do not consider the cause of mass accretion, assuming instead that it is driven by a turbulent viscosity, ν, that is vertically uniform within an annulus, but which can vary with r. Often a uniform α is assumed and the viscosity set to $\nu = \alpha c_s^2/\Omega$. In any case, the viscosity is parameterized. To introduce layered accretion to

our models, we control the value of α. In the majority of models we present here, we have set it to a non-zero value ranging between 10^{-4} and 1 for the active layer, and impose $\alpha = 0$ for the dead zone. This then gives us non-zero viscosities in the active layer and $\nu = 0$ in the dead zone.

In Chapter 3, we studied the effects of non-uniform accretion on the temperature structure and emergent spectrum of a PPD, by considering two types of layered accretion models. One was to vary $\Sigma_{\rm a}$ while defining viscosity (in the active layer) from an assumed $\dot{M}$ (α thus is unconstrained and varies freely). Alternatively, we used assumed values of α to define ν and tested various active layer thicknesses (leaving $\dot{M}$ unconstrained and free). Because $\dot{M} = 3\pi(2\Sigma_{\rm a})\nu$ in a disk undergoing layered accretion, there is a degeneracy in the resulting $\dot{M}$ values when viscosity is defined via α. In other words, a disk with small $\Sigma_{\rm a}$ and large ν (α) can produce the same $\dot{M}$ as a disk with large $\Sigma_{\rm a}$ and small ν (α). Regardless of how viscosity is defined (α or $\dot{M}$) we find that the magnitude of $\Sigma_{\rm a}$ has a major effect on the temperature structure, particularly $T_{\rm mid}$. This is readily understood physically as follows: Where accretional heating dominates stellar irradiation, the surface temperature will be defined by $\dot{M}$, emitting energy as $\sigma_{\rm SB}T_{\rm eff}^4 = (3/8\pi)\dot{M}\Omega^2$. However, the temperature will increase with increasing depth into the active layer. In a disk where $T_{\rm eff}$ is significantly increased due to an internal flux of radiation, the temperature an optical depth τ into the disk will be $T(\tau) \approx (3\tau/4)^{1/4}T_{\rm eff}$ (Hubeny 1990). Once in the dead zone (under the active layer), the disk temperature becomes effectively isothermal. This is due to the fact that, for all values of $\Sigma_{\rm a}$ tested, the bottom of the active layer is always under the superheated layer at height Z. Therefore $T_{\rm mid}$ will be roughly equal to the temperature at the base of the active layer. We can approximate the optical depth of the active layer's base

as $\tau_{\rm a} = \Sigma_{\rm a}\kappa$, where the Rosseland mean opacity has been used for κ. Thus, $T_{\rm mid} = T_{\rm eff}\,(3\tau_{\rm a}/4)^{1/4}$. As $\Sigma_{\rm a}$ grows, $\tau_{\rm a}$ does as well; $T_{\rm mid}$ follows suit.

Disks undergoing layered accretion are generally colder than uniformly accreting disks with the same $\dot{M}$, with consequences for the structure of the disk. We have shown that convection is less prevalent in disks undergoing layered accretion, even with $\dot{M} = 10^{-7}\,M_{\odot}\,{\rm yr}^{-1}$. This is in contrast to the uniformly accreting disks considered by Bell et al. (1997), which experienced some convection at nearly all radii. The flaring index differs as well. We found that the flaring index $\eta = d\ln(Z/r)/d\ln r$ was driven to negative values in a range of r when $\alpha = 10^{-2}$ everywhere in the disk. Physically, this represents the case where accretion in the innermost annuli heats and puffs up the gas in those regions, thereby shadowing annuli further out. Dullemond et al. (2003) proposed that UX Orionis objects could be explained by self-shadowed disks viewed nearly edge-on. To improve the stability of the code we imposed a floor on the flaring index ($\eta > 0.1$) in the uniformly accreting disk. We obtained similar temperatures with a floor of $\eta = 0.01$. Such small values of η correspond to negligible heating by starlight in those annuli. This imposed floor was unnecessary in disks undergoing layered accretion, as the flaring index never became negative in any of the examples we considered. Even when a disk undergoing layered accretion has the same mass accretion rate as a uniformly accreting disk, it will resemble a passive disk, in that convection is not usually relevant and self-shadowing is absent.

As is consistent with the midplane temperatures varying between the layered accretion models tested, the snow line's midplane location varies as well. As demonstrated in Table 3.7, $r_{\rm snow}$ depends on both the thickness of $\Sigma_{\rm a}$ and $\dot{M}$. It has been shown from multiple observations of T Tauri stars that mass accretion varies with the age of the system (Hartmann et al.

1998). This means that a single PPD will see its midplane snow line move as the disk evolves and its accretion lessens. A disk with $\Sigma_{\rm a} = 10\,{\rm g\,cm^{-2}}$ and $\dot{M} = 10^{-6}\,{\rm M_\odot\,yr^{-1}}$ has $r_{\rm snow} = 3.6\,{\rm AU}$. From Hartmann et al. (1998) that corresponds to an age between 1.0×10^5 and $2 \times 10^5\,{\rm yr}$. If the X-ray luminosity of the protostar does not change significantly, then $\Sigma_{\rm a}$ will not change appreciably. Based on Hartmann et al. (1998) a PPD of age $\approx 10^6\,{\rm yr}$ will have $\dot{M} \approx 10^{-8}\,{\rm M_\odot yr^{-1}}$. This would correspond to a snow line at $r_{\rm snow} = 0.8\,{\rm AU}$. The location of the snow line may be pivotal to the formation of planets and planetesimals from disk material. Kretke & Lin (2007) have suggested that sublimation fronts (such as the snow line) may be areas in the disk where grains migrating through the disk may accumulate, allowing larger bodies to form through grain cohesive collisions. Building on that, Brauer et al. (2008) find that so long as gas accretion is not too high, boulder-size particles ($\sim 10^2\,{\rm m}$) can form along snow lines after $\sim 10^3$ yr. Coupled with the movement of the snow line due to the disk's evolution, constraints may be placed on both when and where planets and planetesimals may form out of the PPD. The location of a protostar's innermost gas giant core may also be dependent upon the snow line's location (Kennedy & Kenyon 2008).

Despite the difference in convection and the disk structure, it is difficult to use emergent spectra to distinguish a disk undergoing layered accretion from a uniformly accreting disk. For a given $\dot{M}$, even disks with very different $\Sigma_{\rm a}$ have very similar SEDs, with variations of the same magnitude as those arising from other factors. The variations are comparable in magnitude to the size of the $10\,\mu{\rm m}$ feature, suggesting that grain size and composition will have as much of an effect on the SED as $\Sigma_{\rm a}$. The SED provides information about $T_{\rm eff}$ and therefore $\dot{M}$, but little information about

Σ_a, which is what determines the midplane temperature. It is therefore a challenge to infer midplane temperatures from SEDs, as was attempted by Woolum & Cassen (1999).

Woolum & Cassen (1999) were particularly motivated to determine where midplane temperatures were high enough to yield a globally hot inner solar nebula, in which CAI material could condense from the gas phase. This requires temperatures at least high enough to evaporate silicate material ($T \gtrsim 1350\,\mathrm{K}$), and probably near the condensation temperature of CAI minerals like hibonite and corundum (1660 K and 1680 K, respectively; Lodders 2003). However, Fig. 3.7 demonstrates that even the 1350 K temperature threshold is often not achieved in disks undergoing layered accretion. For $\dot{M} \leq 10^{-8}\,M_\odot\,\mathrm{yr}^{-1}$, these temperatures are never achieved in steady-state anywhere in the disk if $\Sigma_a \leq 100\,\mathrm{g\,cm}^{-2}$. For $\dot{M} = 10^{-7}\,M_\odot\,\mathrm{yr}^{-1}$, the temperature does not exceed 1350 K for $\Sigma_a \leq 30\,\mathrm{g\,cm}^{-2}$, but silicates do evaporate inside 0.2 AU for $\Sigma_a = 100\,\mathrm{g\,cm}^{-2}$. These can be contrasted with the predictions of Bell et al. (1997), who found $T_{\mathrm{mid}} > 1350\,\mathrm{K}$ for $r < 0.2\,\mathrm{AU}$ (if $\alpha = 10^{-2}$), or for $r < 0.7\,\mathrm{AU}$ (if $\alpha = 10^{-4}$), in uniformly accreting disks with $\dot{M} = 10^{-7}\,M_\odot\,\mathrm{yr}^{-1}$. Likewise, in our layered accretion disk models, CAI-forming temperatures of 1750 K are *not* reached in disks with $\dot{M} = 10^{-7}\,M_\odot\,\mathrm{yr}^{-1}$, whereas in the Bell et al. (1997) models, they are achieved inside 0.08 AU (for $\alpha = 10^{-2}$) or 0.3 AU (for $\alpha = 10^{-4}$). We conclude that CAI-forming temperatures require higher mass fluxes ($\dot{M} \gtrsim 10^{-6}\,\mathrm{M}_\odot\,\mathrm{yr}^{-1}$) in disks undergoing layered accretion than in uniformly accreting disks.

This result has consequences for the duration of CAI formation. Because a PPD contains a finite amount of mass, a given mass accretion rate can only be maintained for a finite length of time. We estimate an initial

disk mass of $0.10\,M_\odot$, half of which accretes onto the star during its viscous evolution (Desch 2007), thus providing a reservoir of mass of $0.05\,M_\odot$ for inward accretion. A mass accretion rate $\dot{M} = 10^{-7}\,M_\odot\,\mathrm{yr}^{-1}$ can therefore be maintained for no more than 0.5 Myr. As the temperatures required for CAI formation are higher than can be achieved with this mass accretion rate in a layered accretion disk, we conclude that the duration of CAI formation in a hot inner solar nebula is $\ll 0.5\,\mathrm{Myr}$. We can extrapolate our results to higher $\dot{M}$ by recognizing that in regions where the midplane temperature is significantly affected by accretion, $T_\mathrm{mid} \propto T_\mathrm{eff} \propto \dot{M}^{1/4}$. Thus, $T_\mathrm{mid} > 1750\,\mathrm{K}$ would require $\dot{M} > 2 \times 10^{-5}\,M_\odot\,\mathrm{yr}^{-1}$ at 1 AU, or $\dot{M} > 1 \times 10^{-6}\,M_\odot\,\mathrm{yr}^{-1}$ at 0.3 AU (assuming $\Sigma_\mathrm{a} = 100\,\mathrm{g\,cm}^{-2}$). We estimate that formation of CAIs even at 0.3 AU can persist in a steady-state layered accretion disk (with $\Sigma_\mathrm{a} = 100\,\mathrm{g\,cm}^{-2}$) no more than 50,000 years. This is consistent with the Al-Mg systematics of CAIs, which indicate a similarly short formation interval (Bizzarro et al. 2005).

6.2 Protoplanetary Disk Ionization Chemistry

A proper simulation of PPDs requires the implementation of disk chemistry to ascertain the ionization state of the disk material self-consistently with the rest of the model. In the layered accretion models created to obtain midplane temperatures we performed a parameter study of active layer thickness, Σ_a, with values from 1 to 100 $\mathrm{g\,cm}^{-2}$ tested. This arbitrary selection of Σ_a was dropped in our modeling of the MRI in Chapter 5. As discussed in Chapter 4, implementing disk chemistry is not a trivial task and there is no one algorithm which is necessarily correct for PPDs. In the past, chemistry calculations have been performed using various reaction networks. Some methodologies placed a premium on completeness of species inclusion, which in the case of Ilgner & Nelson (2006) means accounting for 173 neutral and

ion species. Other methods recognized the importance of gas-grain reactions with charged grains and created networks that included a larger range of possible grain charges for the dust grains, such as Sano et al. (2000) which allowed for 7 grain charge states.

For our chemistry network, we chose to focus on correctly capturing the various charge states of the dust grains. We introduced a grid of allowed grain charges with 21 states, which is far larger than previously simulated models. Additionally, we removed the constraint of centering the grid of charge states around a net neutral grain ($q_{\rm net} = 0$) and instead estimated what the mean charge state should be given the strength of ionization sources and used that as our center point of our grid ($q_{\rm net} = Z_{\rm mean} e$). Combined with the large total amount of states available, this allows us to capture the grain physics with greater confidence in our results. As outlined in Table 4.1, our reaction scheme is relatively simple. Our chemistry model revolves around the fact that not all reactions take place at the same rate. In particular, the "bottleneck" reaction, which will largely govern the overall rate of the ionization/recombination reaction chain, is the recombination reaction between HCO^+ and e^-, which produces atomic hydrogen and carbon monoxide (CO). Our chemistry model self-consistently produces electron and ion fractions in the gas, as well as the fractional population of each of the 21 allowed grain charge states.

We tested our reaction network over a range of conditions appropriate for PPDs. Consistent with the assumptions made in Chapters 3 and 5, we imposed a uniform grain size, $a_{\rm gr} = 0.1\,\mu$m. While it is unlikely that a PPD will have dust grains of one uniform size, this approach provides a good starting point for analysis; allowing for varying dust grain sizes is a point of emphasis for future work. The active layer thicknesses were assumed to

range between 0.1 and 100.0 $\mathrm{g\,cm^{-2}}$. Dust-to-gas ratios tested were between 10^{-4} and 10^{-1}. For the purposes of testing our network we assumed an ionization source in the form of a protostar was located 1 AU away. Using $x_e = n_e/n_{\mathrm{H2}} > 10^{-13}$ as a condition for whether the gas will become coupled to the magnetic field and therefore allow for the MRI to occur, we find that in all scenarios tested, the gas can be susceptible to the MRI. In particular, temperature had little role in determining whether or not the gas will couple to the field in the wide range of temperatures tested ($20\,\mathrm{K} < T < 2000\,\mathrm{K}$). Over the range of mass densities, dust-to-gas ratios, and active layer thicknesses tested, all temperature values tested permitted coupling. However, the overall mass densities that permit coupling to the field varied with dust-to-gas ratio and Σ_{a}. We find that as the dust-to-gas ratio increases, the maximum density that supports the MRI affecting the gas decreases. The larger dust-to-gas ratio means that more of the disk's mass is locked up dust grains, leaving less gas in the disk which more importantly means there are fewer free electrons in the disk material.

Holding our dust-to-gas ratio at 0.01 and varying the active layer thickness, Σ_{a}, led to similar findings. As the active layer was made thicker, the maximum mass density that will support gas coupling decreases. Thicker active layers (with the same strength of X-ray ionization source) imply that the ionization events are being spread out over a larger volume, which in turn means that progressively lower densities can negate the ionization enough to keep x_e from reaching the threshold value for MRI susceptibility.

Using the same litmus test for susceptibility to the MRI ($x_e > 10^{-13}$), we can make other findings. Our tests indicated that situations where sufficient ionization is present to permit coupling to the magnetic field correlate to ion to electron ratios (x_i/x_e) that are greater than unity, as seen

in Figure 4.2. The average net grain charge where the disk material is not well-coupled to the magnetic field tends to be near neutral and relatively uniform ($Z_{\rm avg}$ values between -1 and -4). However, in scenarios where the gas is strongly coupled to to the field, $Z_{\rm avg}$ varied over a wide range and correlated strongly with temperature. Higher temperatures yielded average grain charge states that were much more negative. This is consistent with the collision rate of gas particles and grains growing as a function of T, due to the increased kinetic energy of the gas particles, in particular the free electrons.

Finally, we investigated the importance of a wide range in allowed grain charge states. Recall that in previous models including charged grains, the total number of allowed charge states is relatively small (between 5 and 7) and that the grid was centered on net neutral grains. Based on our results in Figures 4.2 and 4.4, this assumption could be introducing error into the calculations. These figures indicate that when allowing the center of the grain charge range to be self-consistently calculated based on the dynamics of the disk, the most populated grain charge becomes more negative with increased T. For the range of T, ρ, $\Sigma_{\rm a}$, and dust-to-gas ratio, ϕ, the range of charge states occupied is mostly filled with negative values of $Z_{\rm avg}$; a total net charge of neutrality (or close to it) is not the center of the occupied states, it is an endpoint.

Given the differences in grain charge grids used by previous ionization chemistry models, it is useful to evaluate how large the grid needs to be to capture an appropriate level of grain physics. A range that is too narrow will not adequately describe the charge states that exist in a real disk, a range that is too wide runs inefficiently. In Figure 4.5 this issue was addressed. Adopting typical disk parameters ($\rho = 4.9 \times 10^{-15}\,{\rm g\,cm^{-3}}$, $a_{\rm gr} = 0.1\,\mu{\rm m}$, $\phi = 0.01$, and $\Sigma_{\rm a} = 10\,{\rm g\,cm^{-2}}$) the fractional occupation of each charge state

was evaluated as a function of temperature. As expected, larger T values increased the populations of grains in the charge states further from the central charge state. Larger temperatures also led to a slightly depressed population in the central charge state. At temperatures approaching 1000 K, the fractional occupation of charge states $5e$ away from the central value surpass 1%, suggesting that in order to accurately simulate the disk chemistry over a range of temperatures, the grids used previously (e.g. Sano et al. (2000) and Ilgner & Nelson (2006)) are insufficient. Testing conducted suggests that if the grid is anchored around $Z = 0$, then significant differences in x_e will manifest themselves. At $T = 100\,\mathrm{K}$ the difference is 8% for a grid of 7 states and 37% for a grid of 7 charge states. These differences grow with increased T. It is important to remember that while a large portion of the disk will be at temperatures low enough to be approximated by 5 to 7 charge states, the central regions near the protostar, as well as the actively accreting layers along the disk surface, will need many more charge states to accurately describe the ionization chemistry.

6.3 The Magnetorotational Instability

As discussed in Chapter 4, to correctly ascertain and model the effects of the MRI it is paramount that the effects of ambipolar diffusion, Ohmic dissipation, and the Hall effect are correctly evaluated and included. When combined with our ionization chemistry network as presented here we obtain models of PPDs subject to the MRI which shed new light on the physical properties of protoplanetary disks, namely the mass flow rates between the disk's annuli.

The $\Sigma_{\mathrm{a}}(r)$ profiles presented in Chapter 5.4 are an improvement over previous models (e.g. Sano et al. (2000)). Similar to those previous models,

our models include the ionization effects of protostellar x rays, cosmic rays, and radioactive elements in the disk. The effects of x rays would be dependent on r, and as would be expected our results for Σ_a are similar to those of Sano et al. (2000) at $r \gtrsim 3\,\mathrm{AU}$, where active layer thickness grows with r to a maximum when the disk is fully active, then following the half surface density profile out to 100 AU. Our models indicate that if our spatially uniform magnetic field is stronger than 0.01 G the outer parts of the low mass disk (which resembles that tested by Sano et al. (2000)) no longer become fully active. This is not necessarily inconsistent with the existing models in the literature, as a $B \propto r^{-11/8}$ field was used by the previous models discussed, yielding $B = 0.08\,\mathrm{G}$ at 10 AU and $0.02\,\mathrm{G}$ at 20 AU. Given the irregular behavior of Σ_a for $B \geq 1.0\,\mathrm{G}$ in Figures 5.1 and 5.2, studying the MRI with these relatively strong magnetic fields is not as enlightening due to the ease at which such disks suppress the effects of the MRI.

The high mass disks exhibit structure in Σ_a at all B-fields tested. For $B \leq 10\,\mathrm{mG}$ the disk transitions from a layered model to a fully accreting model at $r \sim 30\,\mathrm{AU}$. However, the $B = 0.1\,\mathrm{G}$ model has a 2nd dead zone which begins at $r \approx 50\,\mathrm{AU}$ and extends out past the edge of our grid. The models with $B \geq 1\,\mathrm{G}$ have no fully active area of the disk in our grid range, the entire disk is layered. In fact, the magnitude of the local maximum in Σ_a decreases as B is increased once $B > 0.1\,\mathrm{G}$. This probably due to the effects of ambipolar diffusion, as the magnitude of this stabilizing factor's coefficient varies as $\sim B^2/n_i$. The strengthening field is causing ambipolar diffusion to strengthen as well, providing stability to the disk against the MRI. The drop in Σ_a past $r = 30\,\mathrm{AU}$ is due to the decreased ionization. The x ray flux, which is what is primarily responsible for ionizing the gas in the disk, diminishes as r increases. This provides a natural stabilizing effect to the

disk at large r.

An interesting result of our models for both the high and low mass disks tested is the active layer thickness dependence on r for $r < 3\,\mathrm{AU}$. Models that had previously been created of protoplanetary disks in any detail (e.g. Sano et al. 2000) demonstrated that Σ_a monotonically increased with r until the outer edge of the dead zone. For the weakest fields tested ($B \leq 10\mu\mathrm{G}$), this simple relation appears to hold. However, our models with stronger B-fields indicate that this relation between Σ_a and r is not nearly as simple. The inner regions are far more susceptible to X-ray ionization (the X-ray flux at the inner boundary of our modeled disk is 10^6 times stronger than it is at the outer edge. Therefore the ionized fraction of the gas is expected to grow as the proximity to the protostar decreases, meaning that as you approach the protostar, n_i increases faster than n_{H2}. Increasing n_i causes the diffusion coefficient for ambipolar diffusion to decrease, since $D_\mathrm{AD} \sim B^2/n_\mathrm{i}$. The interactions between the higher ionized fraction produces non-linear results for Σ_a. However, the magnetic field's effect on these inner portions of the disk is complicated further. We notice that increasing the strength of $\mathbf{B}$ does not always increase Σ_a. Of the fields tested, Σ_a at the disk's inner edge appears to peak at $B = 0.1\,\mathrm{G}$, then stay roughly constant in the $B = 1\,\mathrm{G}$ model before decreasing. This non-linear behavior is probably also due to the effects of ambipolar diffusion, since as discussed it depends strongly ($\sim B^2$) on magnetic field.

A remarkable and somewhat surprising feature is the strong dip in Σ_a centered around $r \sim 8\,\mathrm{AU}$. The dip appears for both the low and high mass disks and appears to grow in strength as B is increased. The severity of the dip also appears to be dependent on disk mass, as the low mass disks appear to exhibit a deeper dropoff in Σ_a than do the high mass disks. The two more

likely causes of this stability are the Hall effect and ambipolar diffusion. As discussed in Chapter 4, the ambipolar diffusion coefficient scales as $D_{\rm AD} \sim \sigma_\perp/(\sigma_\perp^2 + \sigma_{\rm H}^2)$. Since $\sigma_\perp \sim (n_{\rm H_2}/B^2)(n_i + n_e)$ and $\sigma_{\rm H} \sim (n_i + n_e)/B$, $D_{\rm AD}$ will vary as $\sim B^2/n_{\rm H_2}$ for large densities and/or small magnetic field strengths, which will be true in the areas of the disk being discussed here. As B is strengthened, $D_{\rm AD}$ grows, which makes the left-hand side of Eq. 4.1 increase (providing stability). $D_{\rm H}$ varies as $\sim \sigma_{\rm H}/(\sigma_\perp^2 + \sigma_{\rm H}^2)$. Based on the above discussion, this can be reduced to $D_{\rm H} \sim B^3/n_{\rm H_2}^2$ for large densities and/or small magnetic field strengths. Unlike ambipolar diffusion, the Hall effect can be either stabilizing or destabilizing (it has a presence on both sides of the stability equation); its effects on the disk are difficult to measure analytically. However, given the strong dependence on B and the fact that it is with increased B we see this rapid stabilization, its effects are probably to provide a net stability to the disk. Higher magnetic fields will therefore stabilize the disk against the MRI due to the Hall effect. As the MRI is suppressed, the active layer gets thinner, which is what is seen in our models. As for the apparent difference in dip depth between the disk masses, it is possible that the roughly order of magnitude increase in Σ (which serves to increase the volume density by approximately the same factor) is sufficient to increase stability in these intermediate annuli via Ohmic dissipation. The diffusion coefficient for Ohmic dissipation scales as $D_{\rm OD} \sim 1/\sigma_\parallel$, where $\sigma_\parallel \sim (n_i + n_e)/n_{\rm H_2}$; therefore $D_{\rm OD}$ varies as $\sim n_{\rm H_2}/(n_i + n_e)$. Increasing $n_{\rm H_2}$ causes $D_{\rm OD}$ to strengthen, which when applied to Eq. 4.1 causes the left-hand side of the equation to again rise, marginally increasing stability

The midplane temperature profiles presented are unusual with the existence of the "bump" located roughly at outer edge of the dead zone. This feature consistently appears where $\Sigma_{\rm a}$ reaches its local maximum at the outer

edge of the dead zone (if present). This bump has not appeared in other models of PPDs subject to the MRI, primarily due to the fact that most other models of PPDs impose a temperature structure at the midplane of $T_{\rm mid} \propto r^{-n}$, where n is usually 1/2, rather than self-consistently solve for it as we do. The models that do not impose a temperature profile typically do not include the effects of layered accretion, instead using either no accretional heating at all or a uniform viscosity parameter α. The bump's existence is most likely due to the complicated feedbacks in the disk between $T_{\rm mid}$, $\Sigma_{\rm a}$, and the flaring index, η that are demonstrated in Chapter 3. The steep upward slope of $\Sigma_{\rm a}$ as it approaches the edge of the dead zone equates to the superheated layer being fewer optical depths away from the midplane, allowing it to heat up to a hotter temperature than had $\Sigma_{\rm a}$ been the same as the previous annulus. This increased $T_{\rm mid}$ causes that annulus of the disk to puff up more, exposing a larger effective area to absorb protostellar radiation, which then heats up the annulus more. The bump magnitude is inversely proportional to B, consistent with this explanation since the slope of $\Sigma_{\rm a}(r)$ is steeper for smaller B. Once the local maximum in $\Sigma_{\rm a}$ is reached, this heating effect disappears and the temperature structure returns to normal.

Both disk masses tested produce a similar trend in the rate of mass flowing inward at small r. The weakest B field that didn't result in $\Sigma_{\rm a}$ hitting our minimum value of $\Sigma_{\rm a}$ (which artificially introduces $d\Sigma_{\rm a}/dr = 0$ over annuli with $\Sigma_{\rm a} = \Sigma_{\rm a,min} = 0.1\,{\rm g\,cm^{-2}}$) near the inner edge for the low mass disk is $10\,\mu$G. This field produced a disk with most annulus' mass flowing inward (23 of 34 grid points inside of 10 AU). As the strength of the magnetic field increases toward 10 mG, the amount of disk mass flowing inward decreases (at that field strength only 5 of 34 gridpoints inside of 10 AU are moving mass inward). At $B = 10\,\mu$G in the high mass disk 20 of 34

zones inside of 10 AU have mass moving inward. When B is increased to 0.1 G only 8 zones have mass moving toward the protostar with half of that number lying outside of $r = 3\,\mathrm{AU}$. Therefore under the proper circumstances the MRI can be responsible for moving mass outward at small r. The innermost annulus of the $B = 1\,\mathrm{G}$ disk has $\tau_{\mathrm{evac}} \sim 10^4$yr. However, in order for mass to be evacuating a zone, $\dot{M}$ must be falling faster than r^{-1} to counteract the effects of annuli growing with r. An examination of the corresponding $\dot{\Sigma}$ profiles shows that while mass does want to move outward in disks subject to $B \geq 0.1\,\mathrm{G}$, the gradient of $\dot{M}$ is not steep enough to initially facilitate evacuation of annuli not on the inner edge of the disk (i.e. form a disk gap). However, given that for some of the disks tested the innermost annulus is losing mass as material flows outward, it can be expected for the inner edge of the disk to expand; this would lead to a hole slowly growing.

We see from our summary of evolution timescales presented in Tables 5.1 and 5.2 that there are clear trends between the applied magnetic field strength and τ_{GI} for both the high and low mass disks. We estimate that the low mass disk will be subject to a gravitational instability on timescales of 1.32 Myr for $B = 1\,\mu\mathrm{G}$. This timescale decreases down to 46,000 yr when $B = 0.1\,\mathrm{G}$, which is a likely magnetic field strength in the disk according to studies of paleomagnetic fields in meteorites (Weiss et al. 2008). A similar trend is seen for the high mass disk, although the trend is less clear. The minimum timescale for triggering a gravitational instability ranges from 0.447 Myr when $B = 10\,\mu\mathrm{G}$ to 44,700 years when $B = 10\,\mathrm{mG}$. Regardless of mass, it appears that PPDs subject to fields of $B = 0.1\,\mathrm{G}$ will go through several cycles of mass accruing in bottleneck radii and GIs triggering once $\Sigma(r)$ has reached a critical value as determined with the Toomre parameter. This is consistent with observations of FU Orionis and EX Orionis objects.

Interestingly, low mass disks with weak magnetic fields permeating them may not experience any GI events since the timescale calculated (1.32 Myr) is of the order of expected disk lifetimes. Strong magnetic fields appear to lead to large $\dot{M}$ through portions of the disks modeled, yet they also nearly stabilize the disk at intermediate r.

6.4 Future Work

The breath of the work presented here allows for a number of avenues to be taken to continue the modeling. First and foremost is the evolution of these disks. Given that we self-consistently calculate the temperature, density, flaring index, scale height, and active layer thickness of the disk, our model would be ideal to improve upon the calculations of Suzuki et al. (2010) and test the viability of creating holes in PPDs solely with MRI-induced turbulence. Evolving the disk would also test whether MRI turbulence can concentrate mass enough to trigger a gravitational instability, as suggested by Zhu et al. (2010).

The magnetic field imposed on the disk is most likely not uniform, as was used in this paper. Any B contribution from the rapidly spinning protostar will be radially dependent, likely decreasing as r^{-1}. As shown in Chapter 5, for low mass disks ($\Sigma(r = 1\,\mathrm{AU}) = 1700\,\mathrm{g\,cm^{-2}}$) $B > 0.1$ produce questionable results in outer radii. Attempts at introducing B-fields that vary with r have already been undertaken Sano et al. (2000). However, it is probably the case that the appropriate magnetic field to impose upon the disk's active layers does not mirror whatever ambient field is present due to the molecular cloud the PPD is in or the central protostar's dynamo-created magnetic field due to its rapid rotation. It is important to remember that the MRI which is being simulated in these sorts of models is augmenting the

local B-field. The field is being changed both in magnitude and direction. Simulations of how the magnetic field locally evolves via the MRI are needed to judge mean B and disordered B. The mean B is important because of its use in the stability criterion used to establish the thickness of the active layer. The disordered B will affect the local conductivities of the gas, which also feeds back into the stability criterion. Such appropriately computed B field strengths would greatly improve the models.

Dust settling may also play an important role in understanding the effects of the MRI on the disk's accretion. The dust-to-gas ratio employed in this paper is 0.01, which is typical for PPDs. However, it has been argued that over time dust will tend to settle toward the midplanes of disks, significantly lowering the population of grains in the upper layers where most of the protostellar radiation is directly absorbed and where the viscosity is non-zero. Thus, experimenting with a vertically non-uniform dust-to-gas ratio would have consequences both on the opacity of the disk as well as the ionization chemistry.

If dust settling is present in PPDs, it will not affect all grain sizes evenly. Larger grains will be more likely to settle to the midplane; smaller grains will be more likely to stay suspended in the upper, active layers of the disk. If we assume that a protoplanetary disk has dust grains that range in size between $a_{\rm min}$ and $a_{\rm max}$ and that the dust grain size populations obey a typical MRN distribution (Mathis et al. 1977) we can calculate the reduction in grain mass in the upper layers that would occur if grains larger than a_1 were to settle to the midplane. We begin with an MRN distribution, where a -3.5 dependence on grain size, a, has been assumed and calculate the total

dust density, ρ:

$$\begin{aligned} \frac{dn}{da} &= \gamma a^{-3.5} \\ \frac{d\rho}{da} &= \gamma \left(\frac{4}{3}\pi\rho_{\rm gr}a^3\right) a^{-3.5} \\ \rho &= \frac{8}{3}\pi\rho_{\rm gr}\gamma \left[a_{\rm max}^{1/2} - a_{\rm min}^{1/2}\right] \end{aligned} \tag{6.1}$$

where $\rho_{\rm gr}$ is the density of silicates found in PPDs and we have introduced scaling constant γ. Now we assume that grains larger than a_1 have fallen out and recompute the density of the grains remaining, ρ_1.

$$\rho = \frac{8}{3}\pi\rho_{\rm gr}\gamma \left[a_1^{1/2} - a_{\rm min}^{1/2}\right]$$

The effect of dust settling will be to reduce the density of grains by a factor

$$X = \frac{\rho_1}{\rho} = \frac{a_1^{1/2} - a_{\rm min}^{1/2}}{a_{\rm max}^{1/2} - a_{\rm min}^{1/2}} \tag{6.2}$$

However, electron density will be affected by the surface area of the grains since is it on grain surfaces where most of the ionization/recombination of the gas occurs. Assuming the same MRN distribution, we can calculate the total surface area, σ:

$$\begin{aligned} \frac{d\sigma}{da} &= 4\pi\gamma a^{-3/2} da \\ \sigma &= -8\pi\gamma \left[a_{\rm max}^{-1/2} - a_{\rm min}^{-1/2}\right] \end{aligned}$$

Now compute the resulting surface area if the large grains have settled out of the upper layers.

$$\sigma = -8\pi\gamma \left[a_1^{-1/2} - a_{\rm min}^{-1/2}\right]$$

As with mass density, we take the ratio of these two quantities to obtain the reduction factor in surface area, Y:

$$Y = \frac{\sigma_1}{\sigma} = \frac{a_1^{-1/2} - a_{\rm min}^{-1/2}}{a_{\rm max}^{-1/2} - a_{\rm min}^{-1/2}} \tag{6.3}$$

The relative change in dust mass will be greater than the change total surface area in all cases. To illustrate with an example: Mathis et al. (1977) found that an acceptable range of grain sizes has $a_{\min} = 0.005\,\mu$m and $a_{\max} = 1.0\,\mu$m. If we adopt a grain-settling threshold of $a_1 = 0.1\,\mu$m, then $X = 0.26$ and $Y = 0.84$; this means that after taking into account the effects of dust settling, the mass density of grains will be reduced by 74%, but the surface area would only be reduced by 16%. If instead we chose $a_1 = 0.01\,\mu$m, $X = 0.032$ and $Y = 0.32$, implying mass density and surface area changes of 99% and 68%, respectively. The disparity in changes between these two values means we can safely simulate dust settling by decreasing the dust-to-gas mass ratio. Reducing the surface density by 0.84 (the $a_1 = 0.01\,\mu$m case) is analogous to simply reducing the dust's mass density by 0.84. This will not be exact, as the equations of Draine & Sutin (1987) that are used to compute the disk's ionization chemistry account for dust size in a different way. However, this method will not be far off. We will run models with feedback mechanisms in place to allow the mass ratio to change.

6.5 Summary

We have developed models for protoplanetary disks which calculate the temperature, density, and flaring index self-consistently at all locations. These models include the effects of layered accretion, which heretofore has not been rigorously included in PPD models. Our application of Rybicki's method for computing the temperatures has not been used in this way before, and offers several advantages over often times used Monte Carlo methods which suffer from inaccuracies at high optical depth, τ, without requiring overwhelming amounts of computing time. We found that the midplane temperatures of the disk, which are important for CAI formation and planet formation, depend on the thickness of the active layer for large

values of α and $\Sigma_{\rm a}$. We demonstrated that the emergent SEDs of PPDs are not sensitive to $T_{\rm mid}$, and rather will have characteristics of the surface layers, making difficult the prospects of using observed SEDs as diagnostics of the inner portions of the disks. We found that although inverted vertical temperature profiles are present in accreting disks (i.e. warmer layers under cooler layers), convection will in many cases not occur as it requires $\Sigma_{\rm a} \geq 30\,{\rm g\,cm^{-2}}$ which while technically possible, is not likely to be the case.

We also implemented a new method for solving the ionization chemistry of a PPD's active layers, which while simplistic in its treatment of gas phase reactions, allows for a larger range of dust grain charges than has been done previously. With this ionization chemistry, we developed models of disks subject to the MRI that self-consistently calculate the active layer thickness at all radii which accounting for the MRI suppression processes present in disks: ambipolar diffusion, Ohmic dissipation, and the Hall effect. A range of B-field strengths and two disk surface density profiles were tested. In all cases dead zones were found extending out to $r \gtrsim 16\,{\rm AU}$. We found that the $\Sigma_{\rm a}$ profiles are complicated. For $B > 100\,\mu{\rm G}$ the $\Sigma_{\rm a}(r)$ profiles have two peaks: one at the outer edge of the dead zone and a second at or near the inner edge of the disk. We also found that as B is increased, intermediate radii became more stable to the MRI, and the values of $\Sigma_{\rm a}$ drastically diminish, the added stability likely the result of ambipolar diffusion and the Hall effect. The active layer thicknesses found were in all cases $\leq 10\,{\rm g\,cm^{-2}}$. This resulted in temperature profiles that largely resembled those of a passive disk (i.e. no accretional heating). We used our model results to calculate mass flow rates and evolution timescales for the PPDs. We found a strong dependence on B for GI timescales in low mass disks: if $B = 1\,\mu{\rm G}$ a gravitational instability would be expected roughly every 10 Myr, which may

be longer than the disk's lifetime; as B is increased, the timescales for a GI event become progressively shorter. If $B = 0.1\,\mathrm{G}$, the disk can be expected to become gravitationally unstable every $\sim 50,000\,\mathrm{yr}$.

Adams, F. C., & Shu, F. H. 1986, ApJ, 308, 836

Adams, F. C., Lada, C. J., & Shu, F. H. 1987, ApJ, 312, 788

Alexander, R. D., & Armitage, P. J. 2006, ApJ, 639, L83

Alexander, R. D., Clarke, C. J., & Pringle, J. E. 2006, MNRAS, 369, 216

Alexander, R. D., Clarke, C. J., & Pringle, J. E. 2006, MNRAS, 369, 229

Andrews, Sean M., Wilner, D. J., Hughes, A. M., Qi, Chunhua, and Dullemond, C. P. 2009, ApJ, 700, 1502

Armitage, P. J. 2007, arXiv:astro-ph/0701485

Bachiller, R. 1996, ARA&A, 34, 111

Balbus, Steven A. & Hawley, John F. 1991, ApJ, 376, 214

Balbus, S. A., & Hawley, J. F. 1998, American Institute of Physics Conference Series, 431, 79

Bell, K. R., Cassen, P. M., Klahr, H. H., & Henning, Th. 1997, ApJ, 486, 372

Bell, K. R., Cassen, P. M., Wasson, J. T., & Wollum, D. S. 2000, in Protostars and Planets IV, ed. V. Maggings, A. P. Boss, & S. S. Russell (Tucson: University of Arizona Press)

Bell, K. R., & Lin, D. N. C. 1994, ApJ, 427, 987

Bizzarro, M., Baker, J. A., Haack, H., & Lundgaard, K. L. 2005, ApJ, 632, L41

Bjorkman, J. E. & Wood, K. 2001, ApJ, 554, 615

Blaes, O. M., & Balbus, S. A. 1994, ApJ, 421, 163

Boss, A. P. 1989, PASP, 101, 767

Brauer, F., Henning, T., & Dullemond, C. P. 2008, A&A, 487, L1

Brown, J. M., Blake, G. A., Dullemond, C. P., et al. 2007, ApJ, 664, L107

Cabot, W., Canuto, V. M., Hubickyj, O., & Pollack, J. B. 1987, Icarus, 69, 423

Cabot, W., Canuto, V. M., Hubickyj, O., & Pollack, J. B. 1987, Icarus, 69, 387

Calvet, Nuria, Patino, Alberto, Magris, Gladis C., & D'Alessio, Paola. 1991, ApJ, 380, 617

Calvet, N., & Gullbring, E. 1998, ApJ, 509, 802

Calvet, N., D'Alessio, P., Hartmann, L., et al. 2002, ApJ, 568, 1008

Calvet, N., D'Alessio, P., Watson, D. M., et al. 2005, ApJ, 630, L185

Cameron, A. G. W. 1978, Moon and Planets, 18, 5

Canuto, V. M., Goldman, I., & Hubickyj, O. 1984, ApJL, 280, L55

Cassen, P., & Moosman, A. 1981, Icarus, 48, 353

Chambers, J. E. 2009, ApJ, 705, 1206

Chiang, E. I. & Goldreich, P. 1997, ApJ, 490, 368

Chiang, E. I., Joung, M. K., Creech-Eakman, M. J., Qi, C., Kessler, J. E., Blake, G. A., van Dishoeck, E. F. 2001 ApJ, 547, 1077

Chiang, E., & Murray-Clay, R. 2007, Nature Physics, 3, 60

Cieza, L., Padgett, D. L., Stapelfeldt, K. R., et al. 2007, ApJ, 667, 308

Cieza, L. A., Schreiber, M. R., Romero, G. A., et al. 2010, ApJ, 712, 925

Clarke, C. J., Gendrin, A., & Sotomayor, M. 2001, MNRAS, 328, 485

Cohen, M., & Witteborn, F. C. 1985, ApJ, 294, 345

Connolly, H. C., Jr., Desch, S. J., Ash, R. D, & Jones, R. H. 2006, in Meteorites and the Early Solar System II, ed. D. S. Lauretta & H. Y. McSween Jr. (Tucson: University of Arizona Press)

Currie, T., Lada, C. J., Plavchan, P., et al. 2009, ApJ, 698, 1

D'Alessio, Paola, Cantó, Jorge, Calvet, Nuria, & Lizano, Susana 1998, ApJ, 500, 411

D'Alessio, P., Hartmann, L., Calvet, N., et al. 2005, ApJ, 621, 461

Dahm, S. E., & Carpenter, J. M. 2009, AJ, 137, 4024

Davis, Sanford S. 2003, ApJ, 592, 1193

Descartes, Rene 1644, Principia Philosophiae

Desch, S. J., & Mouschovias, T. C. 2001, ApJ, 550, 314

Desch, S. J. 2004, ApJ, 608, 509

Desch, S. J. 2007, ApJ, 671, 878

Draine & Lee. 1984, ApJ, 285, 89

Draine, B. T., & Sutin, B. 1987, ApJ, 320, 803

Draine, B. T. 2003, ARA&A, 41, 241

Dullemond, C. P. & Dominik, C. 2004, A&A, 417, 159

Dullemond, C. P., van Zadelhoff, G. J., & Natta, A. 2002, A&A, 389, 464

Dullemond, C. P., Hollenbach, D., Kamp, I., & D'Alessio, P. 2007, Protostars and Planets V, 555

Dullemond, C. P., van den Ancker, M. E., Acke, B., & van Boekel, R. 2003, ApJ, 594, L47

Fang, M., van Boekel, R., Wang, W., et al. 2009, A&A, 504, 461

Fleming, T. P., Stone, J. M., & Hawley, J. F. 2000, ApJ, 530, 464

Fleming, T., & Stone, J. M. 2003, ApJ, 585, 908

Gammie, C. F. 1996, ApJ, 457, 355

Garaud, P., & Lin, D. N. C. 2007, ApJ, 654, 606

Glassgold, A. E., Najita, J., & Igea, J. 1997, ApJ, 480, 344

Glassgold, A. E., Najita, J., & Igea, J. 1997, ApJ, 485, 920

Goodman, J., & Xu, G. 1994, ApJ, 432, 213

Grigorieva, A., Thébault, P., Artymowicz, P., & Brandeker, A. 2007, A&A, 475, 755

Gullbring, Erik, Hartmann, Lee, Briceno, Cesar, & Calvet, Nuria 1998, ApJ, 492, 323

Gullbring, E., Calvet, N., Muzerolle, J., & Hartmann, L. 2000, ApJ, 544, 927

Hartmann, L., & Kenyon, S. J. 1996, ARA&A, 34, 207

Hartmann, Lee, Calvet, Nuria, Gullbring, Erik, & D'Alessio, Paola. 1998, ApJ, 495, 385

Hawley, J. F., & Stone, J. M. 1998, ApJ, 501, 758

Hayashi, C. 1981, Progress of Theoretical Physics Supplement, 70, 35

Henning, T. 2010, ARA&A, 48, 21

Herbig, G. H. 2007, AJ, 133, 2679

Hernández, J., Hartmann, L., Megeath, T., et al. 2007, ApJ, 662, 1067

Hubeny, I. 1990, ApJ, 351, 632

Hueso, R., & Guillot, T. 2005, A&A, 442, 703

Hughes, A. M., Wilner, D. J., Calvet, N., et al. 2007, ApJ, 664, 536

Igea, J., & Glassgold, A. E. 1999, ApJ, 518, 848

Ilgner, M., & Nelson, R. P. 2006, A&A, 445, 205

Ilgner, M., & Nelson, R. P. 2008, A&A, 483, 815

Jin, Liping 1996, ApJ, 457, 798

Jonsson, Patrik 2006, MNRAS, 372, 2

Kamp, I. & Dullemond, C. P. 2004, ApJ, 615, 991

Kant, I. 1755, *Universal Natural History and Theory of Heaven*

Kennedy, G. M., Kenyon, S. J., & Bromley, B. C. 2006, ApJ, 650, L139

Kennedy, G. M., & Kenyon, S. J. 2008, ApJ, 673, 502

Kenyon, S. J., & Hartmann, L. 1987, ApJ, 323, 714

Kim, K. H., Watson, D. M., Manoj, P., et al. 2009, ApJ, 700, 1017

King, A. R., Pringle, J. E., & Livio, M. 2007, MNRAS, 376, 1740

Klahr, H. H., & Bodenheimer, P. 2003, ApJ, 582, 869

Klahr, H. H., Henning, T., & Kley, W. 1999, ApJ, 514, 325

Klahr, H. 2007, IAU Symposium, 239, 405

Kretke, K. A., & Lin, D. N. C. 2007, ApJ, 664, L55

Lada, C. J., Muench, A. A., Luhman, K. L., et al. 2006, AJ, 131, 1574

Laplace, P.-S. 1796, *Exposition du Système du Monde*

Larson, R. B. 1969, MNRAS, 145, 271

Laughlin, G., & Rozyczka, M. 1996, ApJ, 456, 279

Lecar, M., Podolak, M., Sasselov, D., & Chiang, E. 2006, ApJ, 640, 1115

Lenzuni, Paolo, Gail, Hans-Peter, & Henning, Thomas 1995, ApJ, 447, 848

Lodders, Katharina 2003, ApJ, 591, 1220

Lynden-Bell, D. & Pringle, J. E. 1974, MNRAS, 168, 603

Mac Low, M.-M., Norman, M. L., Konigl, A., & Wardle, M. 1995, ApJ, 442, 726

Machida, M. N., Inutsuka, S.-i., & Matsumoto, T. 2011, ApJ, 729, 42

Machida, M. N., & Matsumoto, T. 2011, MNRAS, 413, 2767

Malbet, Fabien & Bertout, Claude 1991, ApJ, 383, 814

Merín, B., Brown, J. M., Oliveira, I., et al. 2010, ApJ, 718, 1200

Markwick, A. J., Ilgner, M., Millar, T. J., & Henning, T. 2002, A&A, 385, 632

Mathis, J. S., Rumpl W., Nordsieck K. H. 1977, ApJ, 217, 425

Matsuyama, I., Johnstone, D., & Hartmann, L. 2003, ApJ, 582, 893

Mihalas, D. 1978, Stellar Atmospheres, 2nd Ed. (W. H. Freeman and Company)

Min, M., Dullemond, C. P., Dominik, C., de Koter, A., & Hovenier, J. W. 2009, A&A, 497, 155

Mitchell, J. B. A., & McGowan, J. W. 1983, NATO ASIB Proc. 83: Physics of Ion-Ion and Electron-Ion Collisions, 279

Muzerolle, J., Hartmann, L., & Calvet, N. 1998, AJ, 116, 455

Muzerolle, J., Calvet, N., & Hartmann, L. 2001, ApJ, 550, 944

Muzerolle, J., Luhman, K. L., Briceño, C., Hartmann, L., & Calvet, N. 2005, ApJ, 625, 906

Muzerolle, J., Adame, L., D'Alessio, P., et al. 2006, ApJ, 643, 1003

Muzerolle, J., Allen, L. E., Megeath, S. T., Hernández, J., & Gutermuth, R. A. 2010, ApJ, 708, 1107

Najita, J. R., Strom, S. E., & Muzerolle, J. 2007, MNRAS, 378, 369

Najita, J. R., Carr, J. S., Glassgold, A. E., & Valenti, J. A. 2007, in Protostars and Planets V, ed. B. Reipurth, D. Jewitt, & K. Keil (Tuscon: University of Arizona Press)

Natta, A., Testi, L., & Randich, S. 2006, A&A, 452, 245

Nelson, R. P. 2005, A&A, 443, 1067

Niccolini, G. & Alcolea, J. 2006, A&A, 456, 1

Nishi, R., Nakano, T., & Umebayashi, T. 1990, Galactic and Intergalactic Magnetic Fields, 140, 280

Oishi, J. S., & Mac Low, M.-M. 2009, ApJ, 704, 1239

Pascucci, I., Apai, D., Henning, Th., Stecklum, B., & Brandl, B. 2004, A&A, 426, 523

Penston, M. V. 1969, MNRAS, 145, 457

Penston, M. V. 1969, MNRAS, 144, 425

Pessah, M. E., Chan, C.-k., & Psaltis, D. 2007, ApJ, 668, L51

Pinte, C., Harries, T. J., Min, M., Watson, A. M., Dullemond, C. P., Woitke, P., Ménard, F., & Durán-Rojas, M. C. 2009, A&A, 498, 967

Podolak, M., & Zucker, S. 2004, Meteoritics and Planetary Science, 39, 1859

Pudritz, R. E. 1986, PASP, 98, 709

Quillen, A. C., Blackman, E. G., Frank, A., & Varnière, P. 2004, ApJ, 612, L137

Rafikov, Roman R. 2007, ApJ, 662, 642

Regos, E. 1997, MNRAS, 286, 97

Robitaille, T. P. 2010, A&A, 520A, 70

Robitaille, Thomas P., Whitney, Barbara A., Indebetouw, Remy, Wood, Kenneth, & Denzmore, Pia 2006, ApJS, 167, 256

Sano, T., Miyama, S. M., Umebayshi, T., & Nakano, T. 2000, ApJ, 543, 486

Sano, T., & Stone, J. M. 2002, ApJ, 570, 314

Sasselov, D. D., & Lecar, M. 2000, ApJ, 528, 995

Shakura, N. I. & Sunyaev, R. A. 1973, A&A, 24, 337

Shu, F. H., Johnstone, D., & Hollenbach, D. 1993, Icarus, 106, 92

Sicilia-Aguilar, A., Hartmann, L. W., Fürész, G., et al. 2006, AJ, 132, 2135

Sicilia-Aguilar, A., Henning, T., & Hartmann, L. W. 2010, ApJ, 710, 597

Snell, R. L., Loren, R. B., & Plambeck, R. L. 1980, ApJ, 239, L17

Stamatellos, D. & Whitworth, A. P. 2003, A&A, 407, 941

Stone, J. M., Gammie, C. F., Balbus, S. A., & Hawley, J. F. 2000, Protostars and Planets IV, 589

Stone, J. M., & Balbus, S. A. 1996, ApJ, 464, 364

Strom, K. M., Strom, S. E., Kenyon, S. J., & Hartmann, L. 1988, AJ, 95, 534

Strom, K. M., Strom, S. E., Edwards, S., Cabrit, S., & Skrutskie, M. F. 1989, AJ, 97, 1451

Suzuki, T. K., Muto, T., & Inutsuka, S.-i. 2010, ApJ, 718, 1289

Swedenborg, E. 1734, *Philosophical and Mineralogical Works*

Takeuchi, T., Clarke, C. J., & Lin, D. N. C. 2005, ApJ, 627, 286

Terquem, C. E. J. M. L. J. 2008, ApJ, 689, 532

Tielens, A. G. G. M. 2008, ARA&A, 46, 289

Turner, N. J., & Drake, J. F. 2009, ApJ, 703, 2152

Turner, N. J., & Sano, T. 2008, ApJ, 679, L131

Umebayashi, T., & Nakano, T. 1980, PASJ, 32, 405

Umebayashi, T., & Nakano, T. 1981, PASJ, 33, 617

Umebayashi, T., & Nakano, T. 1988, Progress of Theoretical Physics Supplement, 96, 151

Umebayashi, T., & Nakano, T. 1990, MNRAS, 243, 103

Vorobyov, E. I., & Basu, S. 2005, ApJ, 633, L137

Vorobyov, E. I., & Basu, S. 2006, ApJ, 650, 956

Vorobyov, E. I., & Basu, S. 2008, ApJ, 676, L139

Wardle, M. 1999, MNRAS, 307, 849

Wardle, M., & Ng, C. 1999, MNRAS, 303, 239

Weiss, B. P., Berdahl, J. S., Elkins-Tanton, L., et al. 2008, Science, 322, 713

Whitney, B. A., Wood, K., Bjorkman, J. E., & Cohen, M. 2003, ApJ, 598, 1079

Whitney, B. A., Wood, K., Bjorkman, J. E., & Wolff, M. J. 2003, ApJ, 591, 1049

Whitney, B. A., Indebetouw, R., Bjorkman, J. E., & Wood, K. 2004, ApJ, 617, 1177

Willacy, K., Klahr, H. H., Millar, T. J., & Henning, T. 1998, A&A, 338, 995

Willacy, K., & Langer, W. D. 2000, ApJ, 544, 903

Williams, J. P., & Cieza, L. A. 2011, ARA&A, 49, 67

Winters, W. F., Balbus, S. A., & Hawley, J. F. 2003, MNRAS, 340, 519

Wolk, S. J., & Walter, F. M. 1996, AJ, 111, 2066

Wollum, Dorothy S. & Cassen, Patrick. 1999, Meteoritics & Planetary Science, 34, 897

Wünsch, R., Gawryszczak, A., Klahr, H., & Różyczka, M. 2006, MNRAS, 367, 773

Zhu, Z., Hartmann, L., & Gammie, C. 2010, ApJ, 713, 1143